UNIVERSITÀ DEGLI STUDI DI TRIESTE

GRADUATE SCHOOL OF NANOTECNOLOGY

XXIV CYCLE – 2009 - 2011

Doctoral thesis on:

ADVANCED MEMS RESONATOR FOR MASS DETECTION AND MICROMECHANICAL TRANSISTOR

By:

SEID-HOSSEIN PAKDAST

Under the supervision of:

Dr. MARCO LAZZARINO

UNIVERSITÀ DEGLI STUDI DI TRIESTE

Sede Amministrativa del Dottorato di Ricerca

Consiglio Nazionale delle Ricerche - Istituto Officina dei Materiali - Laboratorio TASC

Posto di dottorato attivato grazie al contributo del Dip.to di Fisica su fondi Consorzio per la Fisica provenienti da Consorzio Area di Ricerca Trieste (finalizzata al Progetto "*Nanotecnologie per l'Energia: sviluppo di celle fotovoltaiche basate su nanostrutture.*")

XXIV CICLO DEL DOTTORATO DI RICERCA IN NANOTECNOLOGIE

GRADUATE SCHOOL OF NANOTECNOLOGY

XXIV CICLO DEL DOTTORATO DI RICERCA IN *NANOTECNOLOGIE*

"ADVANCED MEMS RESONATOR FOR MASS DETECTION AND MICROMECHANICAL TRANSISTOR"

Settore scientifico-disciplinare: FIS01 FISICA SPERIMENTALE

DOTTORANDO:
Seid-Hossein Pakdast
MAT. S911524001

COORDINATORE:
Prof. Maurizio Fermeglia

SUPERVISORE:
Dr. Marco Lazzarino

ANNO ACCADEMICO 2010/2011

Institutions

Università degli Studi di Trieste
Piazzale Europa, 1
34127 Trieste, Italy
www.units.it

Graduate School of Nanotechnology
c/o Dipartimento di Fisica - Università di Trieste
Via A.Valerio, 2
34127 Trieste, Italy
www.nanotech.units.it

The experimental work of this dissertation has been carried on starting from January 2009 at Laboratorio TASC, one of the consociated of the new Istituto Officina dei Materiali (IOM) which is in turn one of the institutes of the italian National Research Council (Consiglio Nazionale delle Ricerche, CNR).

CNR - Istituto Officina dei Materiali
Laboratorio TASC
Area Science Park - Basovizza
Edificio MM
S.S. 14, km 163.5
34149 Trieste, Italy
www.tasc.infm.it

Printed on 02/03/2012 19:03

Table of Contents

Institutions IV
Table of Contents V
Preface and Acknowledgements VII
List of abbreviations X
Abstract XI
1 Introduction to Micro-electro-mechanical- systems 1
1.1 Motivation 1
1.2 Cantilever-based MEMS sensors 4
1.3 Mechanical Coupled Cantilevers 6
1.4 Transduction methods 9
1.5 Cantilevers as mass sensors 16
1.6 Thesis overview 20
2 Theory of Microcantilevers 23
2.1 Introduction 23
2.2 Static Mode 23
2.3 Dynamic mode 24
2.4 Q-factor 26
2.5 Mechanics of Cantilever Systems 30
2.6 Triple Coupled Cantilevers (TCC) 31
3 Simulation of Triple Coupled Cantilever (TCC) Systems 37
3.1 Introduction 37
3.2 Eigenfrequency Modes of TCC by using FEM Simulation 39
3.3 Optimization of the overhang (width and length) 41
3.4 Added mass vs. Amplitude ratio 47
4 Design and Fabrication Process of TCC 53
4.1 Introduction 53
4.2 Design of TCC with Silicon nitride (SiN) 56
4.3 Fabrication process flow of SiN 57
4.4 Fabrication Process of TCC device: 60
4.5 Second design with silicon nitride (SiN) 61
4.6 Fabrication Process Flow of TCC device 63
4.7 Fabrication with Silicon on Insulator (SOI): 66
4.8 Fabrication process of SOI 66
5 Experimental Results 71
5.1 Introduction 71
5.2 Experimental setup 72
5.3 Optimization of Experimental Setup 75
5.4 Actuation methods (Piezoelectric and Optical actuation) 75
5.5 Measurement of SOI TCC 77
5.6 SiN TCC as Mass Sensor 79
5.7 Focused Ion Beam with SiN TCC 84
5.8 A proposal for a Micromechanical Transistor (µMT) 88
5.9 Field Effect Transistor (FET) 92
5.10 Cell Growth on Cantilever 97
6 Conclusions 99
Appendix A – Details of simulation of TCC XV
Appendix B – Width of overhang vs. Resonance frequency XXVI
Appendix C – Process sequences of TCC in SOI, SiN XXVII
Appendix D –Detailed drawings of the vacuum chamber XXX
Appendix E –Growth of Cells XXXII
List of References XXXIII

This page intentionally left blank

Preface and Acknowledgements

This thesis has been written as a part of fulfillment of the requirements for obtaining the Ph.D. degree at the University of Trieste (UniTS), in Nanotechnology during the period from the 1st of January 2009 to the 1st of March 2012. The Ph.D. project has been carried out at CNR-IOM Laboratorio TASC in BioMEMS group in Laboratory for Interdisciplinary Lithography Technology (LILIT) under supervision of Dr. **Marco Lazzarino**.

The path to a PhD degree has been exciting and winding one. The route was not always well illuminated and at times it became very bumpy. Nonetheless, there have been many people who provided guidance and support along the way. I am grateful for their time, friendship, and words of wisdom.

First of all I would like to express my sincerest gratitude, love to my parents and family members for their continuous motivation and support.

I wish to record my deep sense of gratitude to my research supervisor Dr. **Marco Lazzarino** for his benevolent guidance, support and encouragement to carry out this project and his valuable suggestions in preparing this thesis without which I could not have completed my work.

My sincere thanks to all the staff members, lab assistants, secretary (**Roberta** Ferranti, **Paola** Mistron and **Rossella** Fanucchi, etc.) of TASC for their assistance in all respects.

I would like to thank **Stefano** Bigaran and **Vanja** Cvelbar etc for their help with the internet and software programs and **Federico** Salvador, **Andrea** Martin, **Massimiliano** De Marco and **Alessandro** Pertot of electronic and metal workshops for their help to fix the experimental set-up.

I would like to thank to the present and former members of the LILIT and BioMEMS groups which have provided an open, friendly, helpful and inspiring atmosphere which made these past three years a great experience. I would also like to acknowledge **Mauro** Prasciolu to perform Focused Ion Beam (FIB) on one of the TCC devices.

For the part of friendships, I would like to acknowledge **Valeria** Toffoli, **Damino** Casses, **Mauro** Melli, **Elisa** MigliorinіI, **Daniele** Borin, **Luca** Piantanida and **Laura** Andolfi.

Secondly, I thank **Mattia**, Valeria, Daniele for being fantastic office mates during the Ph.D. time and for very interesting discussions we have had in the office.

Thanks for all the useful discussions about science, politics and etc. during the coffee and tea breaks with **Muhammad** Arshad, **Manvendra** Kumar, **Vikas** Baranwal, **Mattia** Fanetti, **Sunil** Bhardwaj, **Sajid** Hussain, P.S.**Srinivas** Babu, **Raffaqat** Hussain and **Lucero** Alvarez Mino etc.

I would like to thank the Iranian friends (**Majid** M. Khorasani, **Sara** Mohammadi, **Saeed** Hariri, **Ahmad** Fakhari, **Mohammad** Bahrami, **Masoud** Nahali and Haghani, **Fatemeh** Kashani, **Sina** Tafazoli and etc.) and Italian friends (Nanotech@trieste) for their fun, help and support throughout the three years of my stay in Trieste.

I also had enjoyable time with all the Centro Universita Sportivo (CUS) members of the table tennis team, especially thanks to our coach **Bruno** Bianchi, for his encouragement, tolerance and always positive mind set.

I thank to Prof. **Maurizio** Fermeglia for being a fantastic program coordinator and leader for Ph.D. School in Nanotechnology of University of Trieste.

This page intentionally left blank

List of abbreviations

AC -- Alternating Current
AFM-- Atomic Force Microscope
Au-- Gold
CTE -- Coefficient of Thermal Expansion
CW --- Continuous Wave
DC --- Direct Current
FEA --- Finite Element Analyse
FEM --- Finite Element Method
FIB ---Focused Ion Beam
HARM -- High Aspect Ratio Micromachining
HNA-- HF/Nitric/Acetic Acid
IC -- Integrated Circuit
KOH--- Potassium Hydroxide
LPCVD -- Low Pressure Chemical Vapor Deposition
MEMS -- Micro-Electro-Mechanical Systems
MOEMS --- Micro-Opto-Electro-Mechanical Systems
MOSFET ------------------------------ Metal-Oxide-Semiconductor Field-Effect-Transistor
NEMS--- Nano-Electro-Mechanical Systems
OD -- Optical Density
pg -- Picogram (1x10^{-12}g)
PR-- Photoresist
PSA-- Prostate Specific Antigen
PZT--- Lead Zirconate Titanatet
QCM -- Quartz Crystal Mass Balance
4QP-- 4-Quadrant Photodiode
RF-- Radio Frequency
RIE ---Reactive Ion Etching
Si--Silicon
SEM --Scanning Electron Microscope
SiN -- Silicon nitride
SOI --- Silicon-on-Insulator
µMT-- MicroMehanical Transitor
UHV -- Ultra High Vacuum
UV-- Ultraviolet

Abstract

Cantilever sensors have been the subject of growing attention in the last decades and their use as mass detectors proved with attogram sensitivity. The rush towards the detection of mass of few molecules pushed the development of more sensitive devices, which have been pursued mainly through downscaling of the cantilever-based devices. In the field of mass sensing, the performance of microcantilever sensors could be increased by using an array of mechanically coupled micro cantilevers of identical size.

In this thesis, we propose three mechanically coupled identical cantilevers, having three localized frequency modes with well-defined symmetry. We measure the oscillation amplitudes of all three cantilevers. We use finite element analysis to investigate the coupling effect on the performance of the system, in particular its mass response. We fabricated prototype micron-sized devices, showing that the mass sensitivity of a triple coupled cantilever (TCC) system is comparable to that of a single resonator. Coupled cantilevers offer several advantages over single cantilevers, including less stringent vacuum requirements for operation, mass localization, insensitivity to surface stress and to distributed a-specific adsorption. We measure the known masses of silica beads of 1μm and 4μm in diameter using TCC. As it is difficult to obtain one single bead at the free end of the cantilevers, we choose to use the Focused Ion Beam. By sequential removing mass from one cantilever in precise sequence, we proved that TCC is also unaffected from a-specific adsorption as is, on the contrary, the case of single resonator.

Finally, we proposed shown the use of TCC can be as micromechanical transistor device. We implemented an actuation strategy based on dielectric gradient force which enabled a separate actuation and control of oscillation amplitude, thus realizing a gating effect suitable to be applied for logic operation.

This page intentionally left blank

1 INTRODUCTION TO MICRO-ELECTRO-MECHANICAL- SYSTEMS

1.1 Motivation

This chapter gives an overview of the MEMS cantilever sensors. First, a brief description of MEMS topics including main applications is presented. Next section introduces the mass sensors based on resonant beams including the state-of-the-art of ultra-sensitive sensors. Finally the outline of chapters is described.

The transistor was invented in 1947 gave rise to the beginning of Integrated Circuit (IC) technology which is the machining of complex electronic circuits on a small piece of a semiconductor [1]. This technology would be a revolution so big efforts have been made in almost 20 years in order to shrink the dimensions of transistor and thereby increase the quality of the microstructures on a chip.

Since the fifties, physicists, chemists and engineers joined up, because of the necessity of broad interdisciplinary competences, and many materials, processes and tools have been invented and deeply studied. Nowadays, it is possible to manufacture 1 million of transistors per mm^2, because of the development of manufacturing processes. This allowed to shrink computers which had dimensions of a room in devices which can be kept in one hand. Indeed, “shrink” is the keyword of IC industry because smaller means cheaper and faster because less material, power consumption and space are required.

In thirty years, the minimum printed line widths (i.e., transistor gate lengths) has reduced from 10 microns (1971) to 32 nanometers (2010) and the International Technology Roadmap for Semiconductors (ITRS) estimates that the 11 nanometer will be reached in 2022 [2]. It will be the ultimate step of the miniaturization of silicon devices: smaller than this will be forbidden by quantum mechanics laws.

However, all the know-how, accumulated in decades, was not confined only in the electronic industry but several and different applications have been proposed. In the 1970s, the concept of micro-electro-mechanical systems (MEMS) was introduced and now this technology is widespread in many devices: from ink-jet and bubble-jet printer heads [3], digital projectors [4,5,6], accelerometers [7,8], and has been successfully commercialized in the market [9].
MEMS is the integration of mechanical and electronic elements on a common substrate through the utilization of microfabrication technology. The mechanical part, which can generally move, has two main functions: sensing and actuating. For example, MEMS are used as sensors in accelerometers, gyroscopes, pressure or flow sensors and, as actuator, they are employed as micromotors, mirror mounts, micro pumps and AFM cantilevers [10] All the examples reported above are MEMS devices that have succeeded in being competitive in the market. There are some emerging MEMS based products that might be better than the existing technology in the future, such as the Millipede ™ project [11] that aims to offer better cost/data storage ratio than existing options such as flash memory.
The reasons of their success are basically three:

1. They are cheap. Due to the “batch processing” many devices are made in same time reducing the price of a single component.
2. They are extremely sensitive. In fact, as rule of thumbs, in many applications, the smaller the sensor, the less is affected by external perturbation. Moreover as actuator, precision down to nanometer scale is achievable.
3. They are small. It is possible to integrate many sensors and many function on the same device, which in turn can be embedded practically in every environment.

Besides these commercial available applications which we use every day, MEMS has attracted the interest of some researchers in field of fundamental research.
Due to a constant efforts to shrink the device and to improve the measurement techniques, it has been demonstrated force and mass sensitivity of the order of zeptonewtons and zeptogram (zepto = 10^{-21}). In general, these devices are called nano-electro-mechanical-systems (NEMS) to stress the difference with the micro device, but, usually just one of three dimensions (i.e. thickness) is less than 100 nanometers, in figure 1.1 some of the most important results are shown.

However, this kind of measurements, requires extremely demanding condition, like milliKelvin temperature and ultra high vacuum, so with the present technology, they are

confined in few high level laboratories and can hardly be applied for any commercial applications. But if we accept the compromise of reducing the sensitivity in favor of increasing the feasibility we can still use the MEMS approach for developing tools and application for different fields of science, including Biology and Medicine.

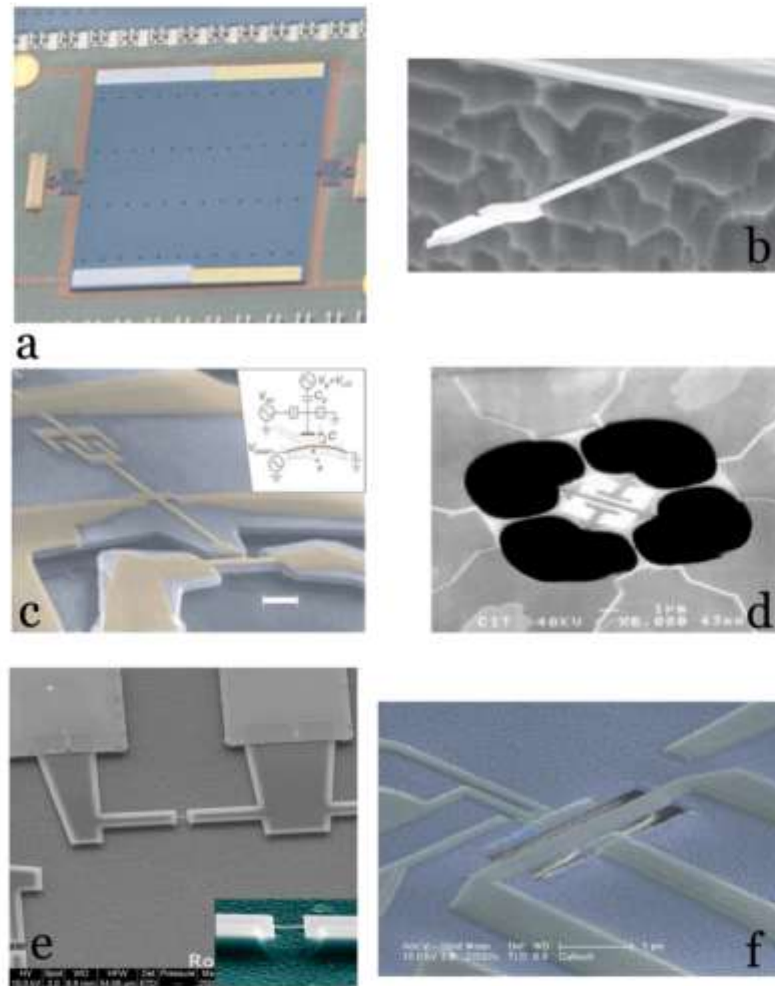

Figure 1.1: NEMS devices

(a) A torsional resonator used to study Casimir forces [12]

(b) An ultrasensitive magnetic force detector that has been used to detect a single electron spin [13]

(c) A 116-MHz resonator coupled to a single-electron transistor [14].

(d) Suspended mesoscopic device used for measuring the quantum of thermal conductance [15].

(e) Zeptogram-Scale Nanomechanical Mass sensor [16].

(f) Nanomechanical resonator coupled to qubits [17].

1.2 Cantilever-based MEMS sensors

The use of cantilevers in microtechnology became popular with the invention of the Atomic Force Microscope (AFM) in 1986 [10,18] and nowadays they are very important tools within the research area of micro- and nanofabrication. A cantilever is a beam that is clamped at one end and free-standing at the other figure 1.2. The length L and the width W define the cantilever plane and typically the thickness t is at least an order magnitude lower than the other dimensions. In the AFM, a sharp tip is added at the free-standing extremity and the surface of the sample is scanned while measuring the deflection of the cantilever, which is caused by the interaction of the tip with the sample. In controlled conditions, with extremely sharp tips and proper samples, the tip-sample interaction is dominated by the attractive and repulsive forces at atomic level, hence the name of atomic force microscopy figure 1.3. The low spring constant of the cantilever allows a high out-of-plane deflection of the cantilever upon small changes of the topography.

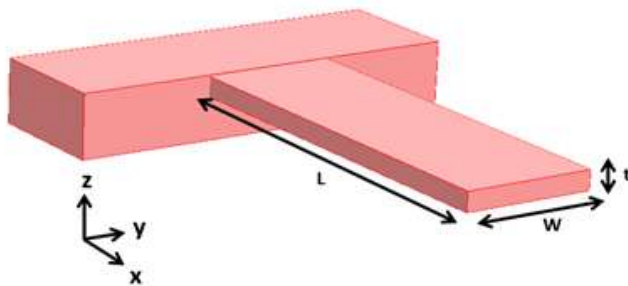

Figure 1.2: Schematic of a cantilever

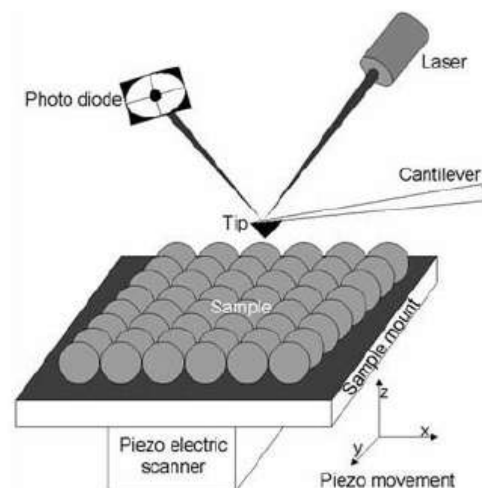

Figure 1.3: Principle of the AFM [19]

In the 1990s, a large variety of sensor technologies based on microcantilevers were applied as mass sensors [20,21,22,23,24], such as biological, physical, chemical, medical diagnostics and environmental monitoring. One of the advantages of micromechanical biosensors is that microcantilevers are produced using a microfabrication process, which allows parallel production of microcantilevers at low cost, and with a very low structure error. This has motivated the development of biosensors based on arrays of microcantilevers [25,26,27]. It has been demonstrated that microcantilevers can be used for the identification and detection of bio/chemical molecules [28], evaluation of hydrogen storage capacity [29] and monitoring of air pollution [30]. One particular kind of application of biosensor-based cantilever is the

highly sensitive and label-free mass detection by measuring resonant frequency shifts before and after the load of biological mass [31,32,33]. Resonating cantilevers can be used for mass detection because added mass results in a change of the resonance frequency of the beam [34,35].

The basic principle is the measurement of the resonance frequency shift is due to the mass adsorption to the cantilever, effecting a change in cantilever mass, assuming that the spring constant is remained constant, and then a change in cantilever mass and a shift in the resonance frequency occur. This mass sensing has been widely used as a detection scheme for small masses, e.g. DNA, virus and cells [36,37,38,39]. Another sensor principle is based on changes of surface stress resulting in static bending of the cantilever [40,41,42]. These measurement methods will be discussed in detail in the following section. For all cantilever-based sensors, optical read-out is most commonly used for the measurement of the cantilever deflection figure 1.3 [43,44,34,40,41,42,45]. A laser beam is focused onto the apex (free end) of the cantilever and the reflection is monitored using a position sensitive photodiode (PSD). Alternatively, the use of piezoresistive [46,47], piezoelectric [48,49], capacitive [50,51,52] or MOSFET-based [53] read-out methods has been demonstrated. The selection of the read-out method depends on the specific application. For example, compared to optical read-out, the integration of piezoresistors has the advantage that the signal is not influenced by the optical properties of the surrounding medium. On the other hand, fabrication of the cantilever devices for piezoresistive read-out is more time-consuming.

In the last decay the microcantilevers have been used to sense DNA, proteins, antigen-antibody reactions, gases etc. [54,55,56,57,58]

Cantilever sensors can be applied in three different areas: *surface stress*, *change in temperature* and *change in mass*, where the different areas will be explained below:

- Surface stress: The surface of the cantilever is coated with a detection layer. When the target molecules bind to the detection layer they will induce a surface stress, typically originated from the increase in volume of the bound molecules, thus causing the cantilever to bend, see figure 1.4A.

- Change in temperature: When there is an exothermic or endothermic reaction, it will change the temperature of the cantilever. In the case where the cantilever is made of several materials with different Coefficient of Thermal Expansion (CTE), it will bend due to the bimorph effect, see figure 1.4B.

- Change in mass: The resonance frequency of the cantilever is depending on the mass of the cantilever. When a mass is added, the resonance frequency will be changed, see figure 1.4C.

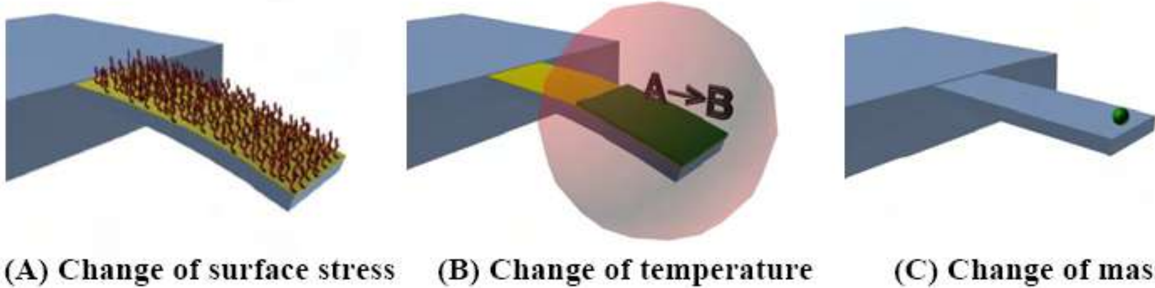

Figure 1.4: Three different detection principles using a cantilever. (A) Illustrates change in surface stress due to chemical adsorption. (B) Change in temperature due to different chemical solvent on the free end of the cantilever. (C) Mass change can be measured due to change in resonance frequency. [59]

Cantilever-based sensors are applied in many various fields. The collective behavior of coupled MEMS arrays can also efficiently enhance the performance of resonator-based devices, such as RF-filters [60], mass sensor [61,62], magnetometers [63], etc.

In this Ph.D. thesis, we will show a novel and alternative design of a mass sensor. With this design we are independent of the surface stress as it is the case in the resonance shift method for a single cantilever system. The detection mechanism is called mode localization of vibration amplitudes of array of cantilevers [64,65]. The main challenge in this Ph.D. project lies on the fabrication processes.

1.3 Mechanical Coupled Cantilevers

The coupled cantilever systems approach exhibits sensitivity comparable with the well established frequency shift method, when used in high vacuum and with high quality factor cantilevers, and offers several additional advantages. Our device is less affected by the surface stress induced by mass adsorption along the cantilever; the quadratic dependence on the adsorbing site position allows a more precise determination of the mass location; using the oscillator phase response it is possible to identify the cantilever onto which adsorption takes place.

Resonating microstructures and resonant cantilevers in particular have been proposed as very

sensitive tools for mass detection with sensitivity down to single molecule level [66]. In spite of the impressive effort which have been devoted so far to the investigation of resonant microstructures in many different fields, very little has been proposed in the direction of a higher degree of complexity; A. Qazi *et al*. demonstrated a driver-follower geometry for molecular detection [67]; M. Spletzer *et al*. proposed the use of coupled cantilevers for mode localization derived mass detection [68]; E. Gil-Santos *et al.* focused on the influence of actuation strategy on the mode localization observing that inertial actuation excite preferentially one cantilever and distorts the system response, while using thermal excitation it is possible to obtain a more realistic behavior at the price of a lower signal to noise ratio [69]. Finally H. Okamoto and coworkers proposed a GaAs based coupled clamped beams [70] in which the asymmetries of the device are compensated by inducing locally a thermal stress with a laser, thus obtaining a perfectly symmetric device.

The detectors based on two weakly coupled cantilevers, shown in figure 1.5, have two major limitations. Upon mass adsorption on one cantilever the initial symmetry is broken and the modes are localized: in particular the cantilever where the mass is adsorbed will oscillate mainly at the higher frequency while the reference cantilever will have higher oscillation amplitude on the low frequency mode. However, both cantilevers have finite amplitude in both modes; moreover unless the frequency is tuned by stressing one cantilever as already done for clamped beams [70], the relative amplitude in the two modes is not controllable. Upon mass adsorption the amplitude variation is relatively small and depends on the initial amplitude.

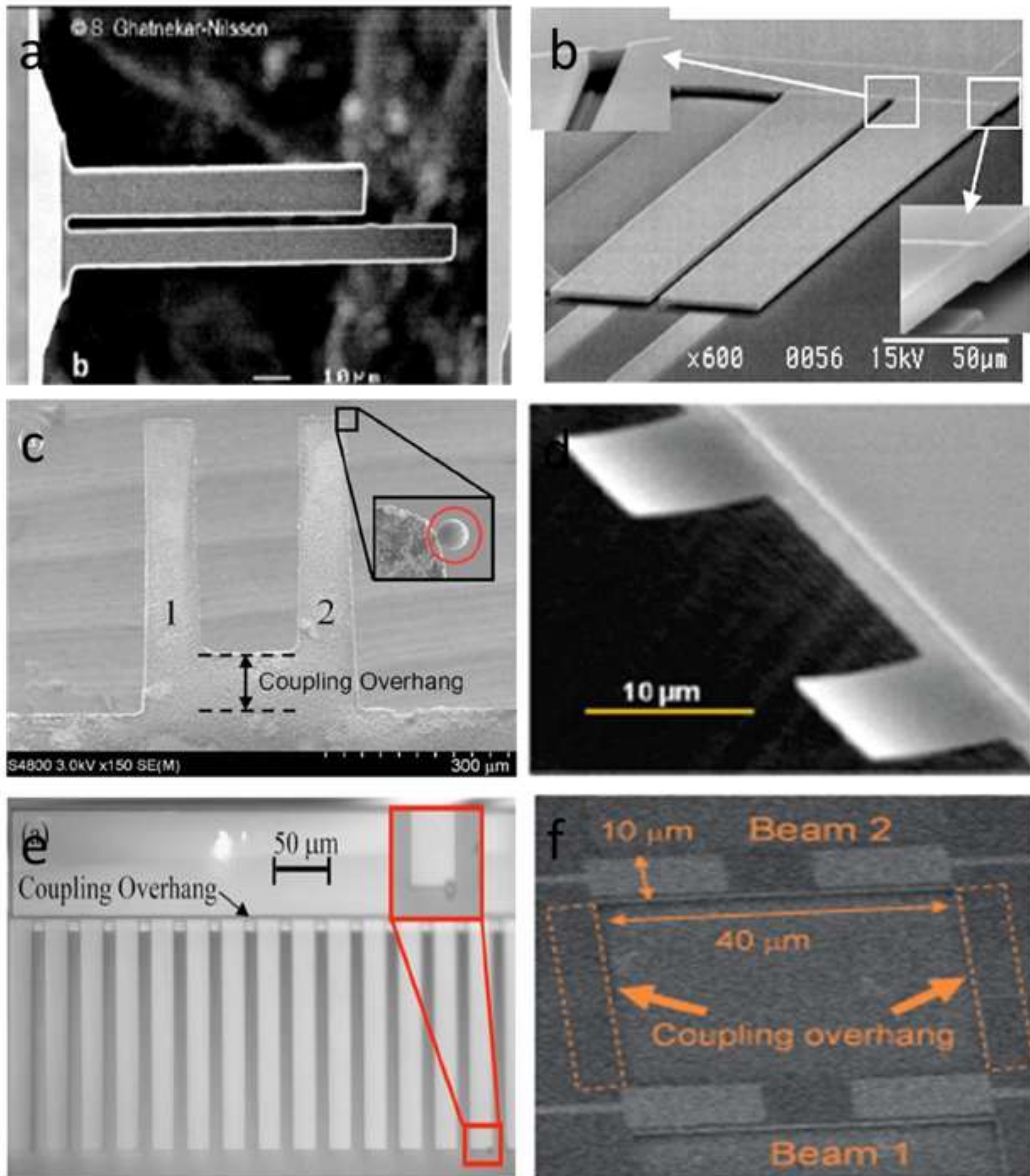

Figure 1.5: Coupled microcantilever devices.

(a) Array of two cantilevers are fabricated by Focused Ion Beam, offering possibility for mass sensor applications [71].

(b) A pair of electrostatically and mechanically coupled microcantilevers [72].

(c) The two nearly identical coupled microcantilevers are proposing an ultrasensitive mass sensing by using mode localization in the vibrations [68].

(d) Coupled nanomechanical systems and their entangled eigenstates offer unique opportunities for the detection of ultrasmall masses [69].

(e) Mass detection and identification of using vibration localization in coupled microcantilever arrays [73].

(f) Frequency tuning of two mechanically coupled microresonators by laser irradiation is demonstrated. [70].

1.4 Transduction methods

Various micro-sensing and -actuation principles have been developed for different application areas [74], including chemical sensors, gas sensors, optical sensors, biosensors, thermal sensors, mechanical sensors, etc. The main point in the actuation mechanisms is that an electrical signal need to be transferred to a mechanical vibration, as it is in the case of a mechanical microresonator. In the following some of the main sensing mechanisms for mechanical microresonators will be introduced.

1.4.1 CAPACITIVE SENSORS

Capacitive sensors consist of a pair of electrodes arranged in such a way that one of the electrodes moves when the input variable (pressure, acceleration, force, etc.) is applied. The deformation of the structure change the capacitance of the system which in turn converts into electrical signals (such as changes in oscillation frequency, time, charge, voltage, etc.), as seen in figure 1.6a. The drawback of this sensing mechanism is that it requires the circuit to be integrated on the chip, thus, increasing the complexity of the fabrication process. There are some limitations about this technique. For example the measurement of a cantilever deflection depends on the dielectric material between the conductive plates that must be constant during the experiment. If the analyte diffuse also within the gap it may change corresponding dielectric constant and invalidated the measurements. For a parallel plate capacitor, the capacitance, is inversely proportional to the gap between the capacitors plates and the force, is inversely proportional to the gap between the capacitor plates squared. The capacitance and the force of the parallel plate capacitor are highly nonlinear. As the displacement of the distance between the plates goes to zero, the electrostatic force becomes very large. In the case where the two plates get close to each other, may stick together, which limits the deflection of the cantilever. In fact, when the two electrodes are closer than one particular threshold, called *Pull-in point* (instability point), the attractive force, which goes as the inverse of the separation, overcome the restoring force which is just linear with the

displacement, and the two arm collapse on each other. The scaling down of the electrodes or cantilever will decrease the sensitivity as well, due to the fact that the capacitance of a capacitor is proportional to its surface area. At this level the parasitic effects become more than the actual detection signals. A capacitive sensor is fabricated based on cantilever-fingers by Scott Miller *et al,* as shown in figure 1.6b.

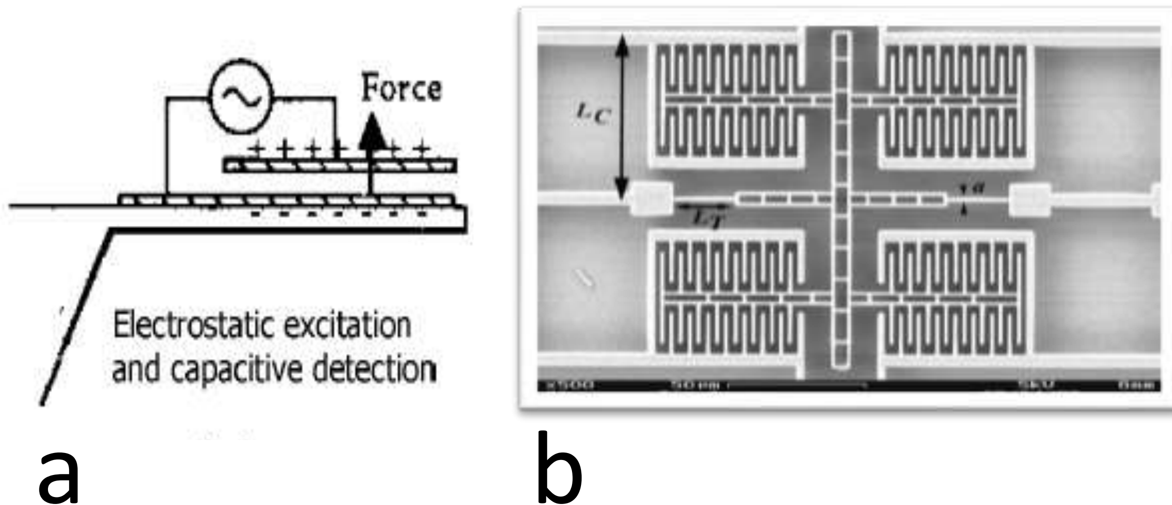

Figure 1.6: Capacitive detection sensor based on cantilever. a) A schematic of capacitive detection and electrostatic excitation [75]. b) An example on capacitive sensor on cantilever-fingers [76]

There are fix electrodes and movable electrodes. The cantilevers are movable electrodes, as shown in figure 1.6b. The vibration of the movable electrodes is coming from the asymmetric field which creates moving away from the substrate (fix electrodes). This system is very sensitive to small changes in the distance and can be measured as well. The pull-in depends in a capacitive system on the geometric quantities (i.e., not a function of spring constant, area, etc.). The pull-in phenomena make constraint on the design of capacitive sensors and actuators.

1.4.2 PIEZOELECTRIC SENSORS

Simply stated, piezoelectric materials produce a voltage in response to an applied force, usually a uniaxial compressive force. Similarly, a change in dimensions can be induced by the application of a voltage to a piezoelectric material. In this way they are very similar to electro-strictive materials.

These materials are usually ceramics with a perovskite structure , see figure 1.7. The

perovskite structure exists in two crystallographic forms. Below the Curie temperature they have a tetragonal structure and above the Curie temperature they transform into a cubic structure. In the tetragonal state, each unit cell has an electric dipole, i.e. there is a small charge differential between each end of the unit cell.

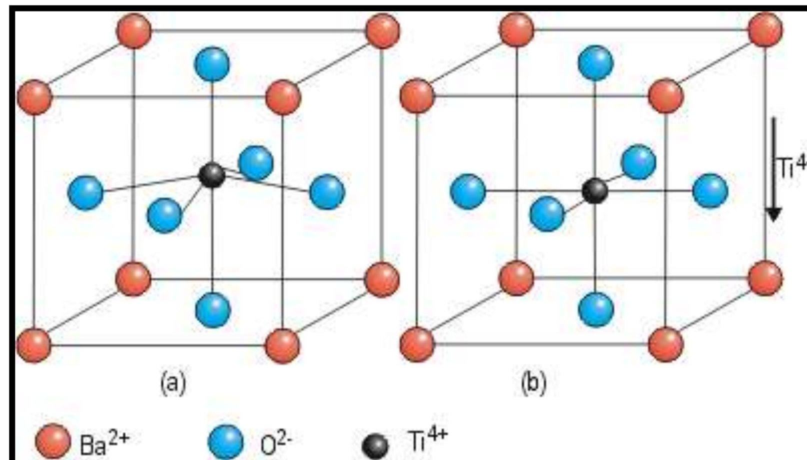

Figure 1.7: Shows the (a) tetragonal perovskite structure below the Curie temperature and the (b) cubic structure above the Curie temperature [77].

A mechanical deformation (such as a compressive force) can decrease the separation between the cations and anions which produces an internal field or voltage.

In MEMS applications, thin films of piezoelectric materials are deposited on the device, usually by evaporation or sputtering, and are used as movement sensors and actuators. . By applying an AC signal, the material will expand and compress at in time in request to the applied DC and AC signal. When the mechanical modulation reaches the resonance frequency of the resonator it is possible to induce large oscillations, orders of magnitude larger than the actual displacements produced by the piezoelectric actuator, figure 1.8. The QCM (Quartz crystal mass balance) is one example of commercial device using a piezoelectric material, quartz, to put the detector into resonance frequency. A QCM device works by sending an electrical signal through a gold-plated quartz crystal, figure 1.8b, which causes a vibration at some resonant frequency

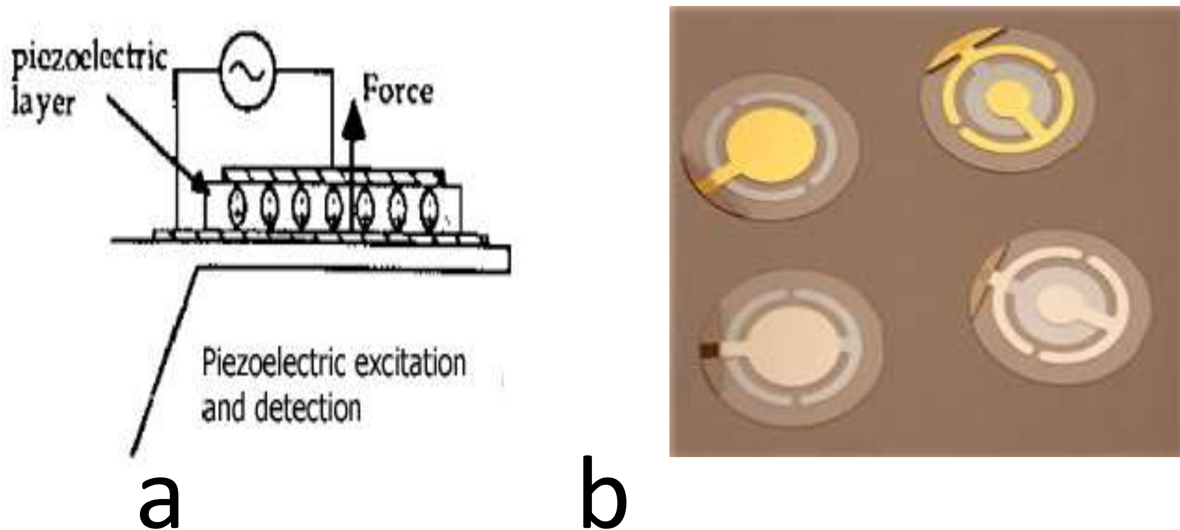

Figure 1.8: a) A schematic of piezoelectric actuation on a cantilever. Reproduced from [75] b) The QCM is a piezoelectric mass-sensing device.

The PZT material as actuating mechanism has several advantages over other actuating mechanisms. Since this sensor generates its own voltage, it does not require any further steps in microfabrication processes. Therefore, the application of piezoelectric actuation has been used in many biosensor applications. Furthermore, the piezoelectric effect depends only linearly with the size, therefore also the smallest NEMS can be actuated with this approach. In alternative, external piezo slab can be used to oscillate the whole MEMS chip as is used done in AFM instruments operating in dynamic modes. Unfortunately in this way all the eigenfrequencies of the whole chip are excited: a piezoelectric base excitation applied to the ensemble of the cantilevers cannot efficiently excite many of the entangled coupled eigenstates thus limiting the sensitivity of such arrays [69].

1.4.3 PIEZORESISTIVE SENSORS

A typical structure for a piezoresistive microsensor is shown in figure 1.9a. The resistor can be produced by a selective doping by implantation or diffusion of the moving part in silicon or by depositing a conductive layer with a significant piezoresistivity. To maximize the effect, the resistor is usually located in the region where the displacement is larger e.g. in cantilevers close to the fix end. The deflection of the cantilever induces a change of the resistor strain, hence resulting in the resistance changing due to the piezoresistive effect in silicon. To enhance the sensitivity, four piezoresistors could be made and connected into a Wheatstone bridge configuration [78], thus obtaining a differential reading and minimizing the noise.

These kinds of built-in detection can make the fabrication process more complex, but can be efficient for a fast response time.

The performance of piezoresistive microsensors varies with temperature and pressure. The sensitivities of the sensors decrease as the temperature increases, while any residual stress generated during the fabrication will also influence the sensitivities of the sensors. The piezoresistive method is mostly used in static mode, because there cantilevers are thin and softer and the forces generated by the adsorbed molecules result in large bendings. [79], thereby it is easy to measure the quantitative of molecules by calculating the resistance changes.

In some cases, the piezo resistance has been used also in dynamic mode, as in the experiment illustrated in figure 1.9b. Here a very thin (10nm) layer of gold is deposited ontop of insulating silicon nitride cantilevers that operate at very high frequency. Because of the reduced thickness of the film, the change in the grain boundaries induced by the strain produces a detectable effect in the resistance of the film itself.

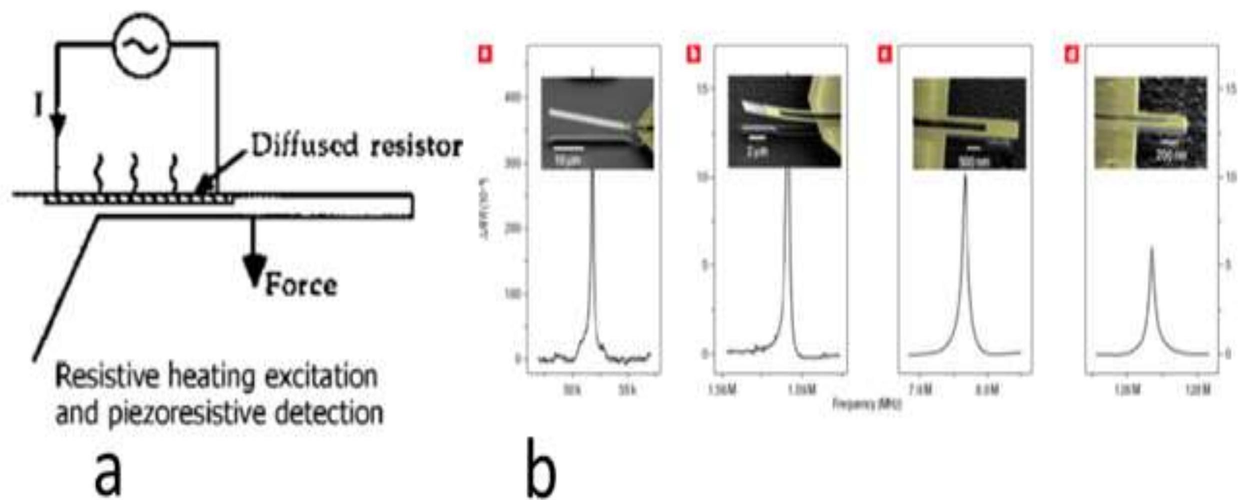

Figure 1.9: a) A schematic of piezoelectric actuation on a cantilever. Reproduced from [75] b) The resistance strain vs. frequency spectrum. There are four different lengths of cantilevers. The detection of resonant frequency is done by piezoresistors. [20]

1.4.4 Optical actuation

The vibration modes can be excited by focusing a frequency-pulsed laser beam near the fix end of the microcantilever. The laser induces a time-periodic temperature change around the spot region, which gives a cantilever vibration via the periodic stress in the material.

Usually, the photothermal excitation of the cantilevers was achieved by a red laser diode beam. It is a non-contact and local excitation of micromechanical resonator. The spot size can

be around 2-10 µm. One of the advantages of using photothermal actuation is that it can select which spatial mode of a microcantilever can be excited.

Optical actuation has been demonstrated to work also a liquid environment [80]. The optical actuation does not need any electrical connections on the device nor a specific fabrication procedure and the most common approach of using a microcantilever with multilayer of different thermal expansion coefficients will affect a deflection of the microcantilever when it is heated by the absorption of the incoming laser beam, see figure 1.10.

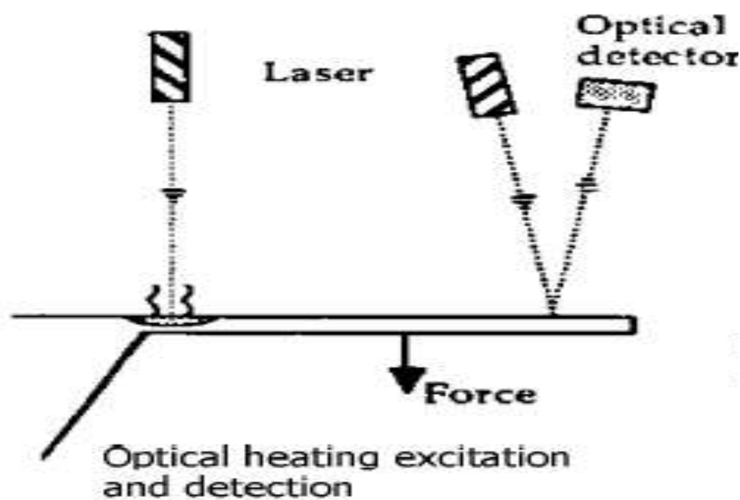

Figure 1.10: An optical actuation technique. Reproduced from [75]

The photothermal excitation technique has been used by Datskos *et al.* [81] to illustrate that the microcantilevers can be actuated by optically actuation, shown in figure 1.11.

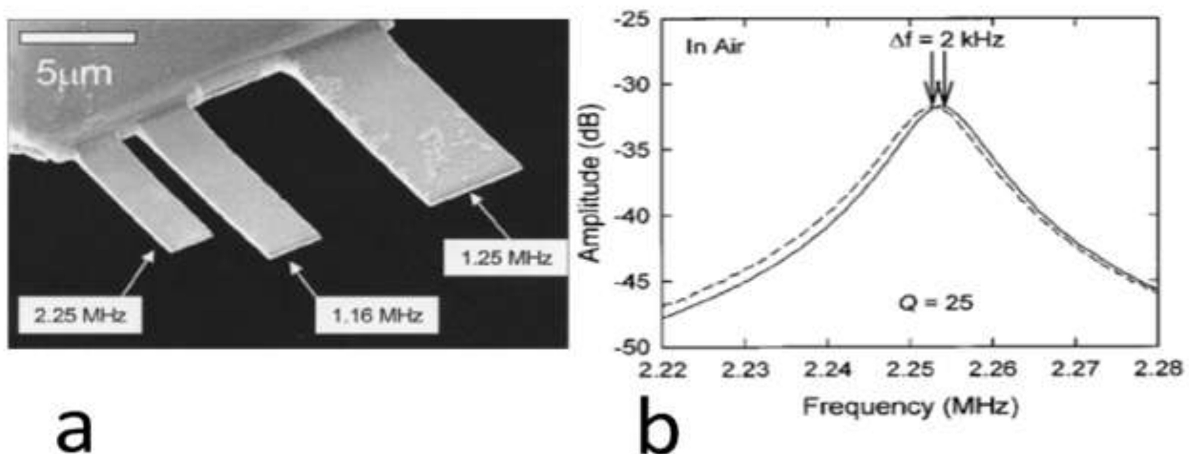

Figure 1.11: a) The picture is a SEM image of different lengths and resonance frequencies. These microcantilevers are made of gold-coated Silicon. b) An experimental result illustrates a frequency shift of the smallest cantilever at the resonance frequency (f_0=2.25 MHz) before and after adsorption of 11-mercaptoundecanoic acid in air surrounding. [81]

One example is illustrated in figure 1.11. This experiment is done with the gold-coated Silicon microcantilever that has a resonance frequency at 2.25 MHz, see figure. 1.11a. It is illustrated in figure 1.11b the measurements of before and after evaporation of the 11-mercaptoundecanoic acid absorbed. The measurement is done in an air ambient, which means that the damping has a big affect on the vibration of the cantilever.

1.4.5 Dielectric gradient force

A recently published paper by P. Quirin *et al.* [82] in Nature has illustrated that it is possible to actuate any kind of dielectric materials in an inhomogeneous electric field. The basic principle is that the electrodes, usually coated with gold, are connected to a DC (direct current) and an RF (radio frequency) sources. The DC is applied to the electrodes and indirectly polarize the resonator which should b made of a dielectric material, such as Silicon nitride. The force that is created by the static voltage, V_{DC}, can be modulated by applying RF. This configuration can be able to excite the dielectric material, which in the case of the cited paper was a double clamped beam, as shown in figure 1.12.

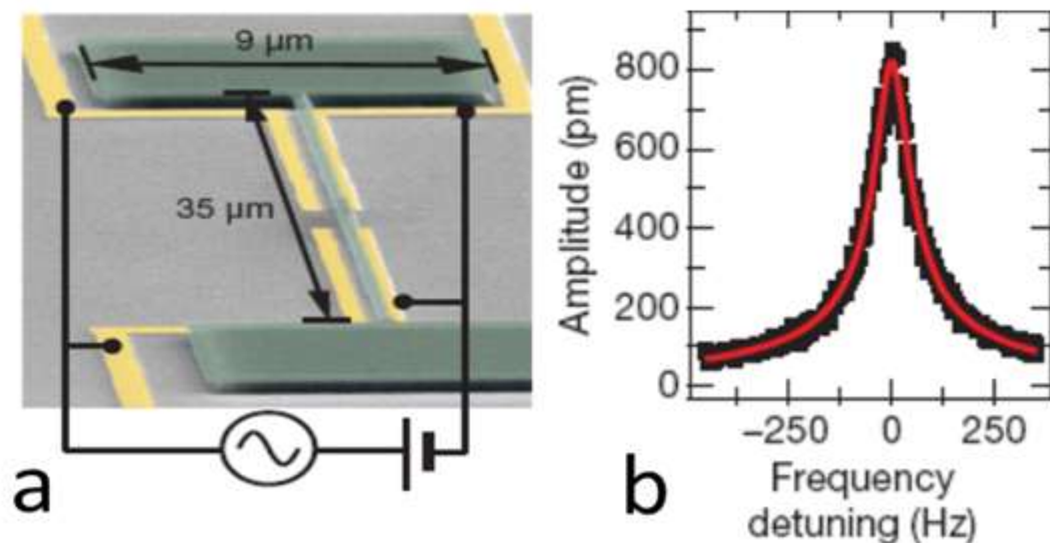

Figure 1.12: a) A depicted image of suspended double clamped beam of silicon nitride. The electrodes (yellow) are connected to DC and RF. b) The suspended double clamped beam is actuated by dielectric force. [82]

There are both advantages and disadvantages for all the different actuation and detection methods. The choice of the optimal approach depends highly on the environment and on the specific application of the resonator with respect to the fabrication process. Furthermore, the actuation and detection configurations are not limited, can be combined and interchanged

1.5 Cantilevers as mass sensors

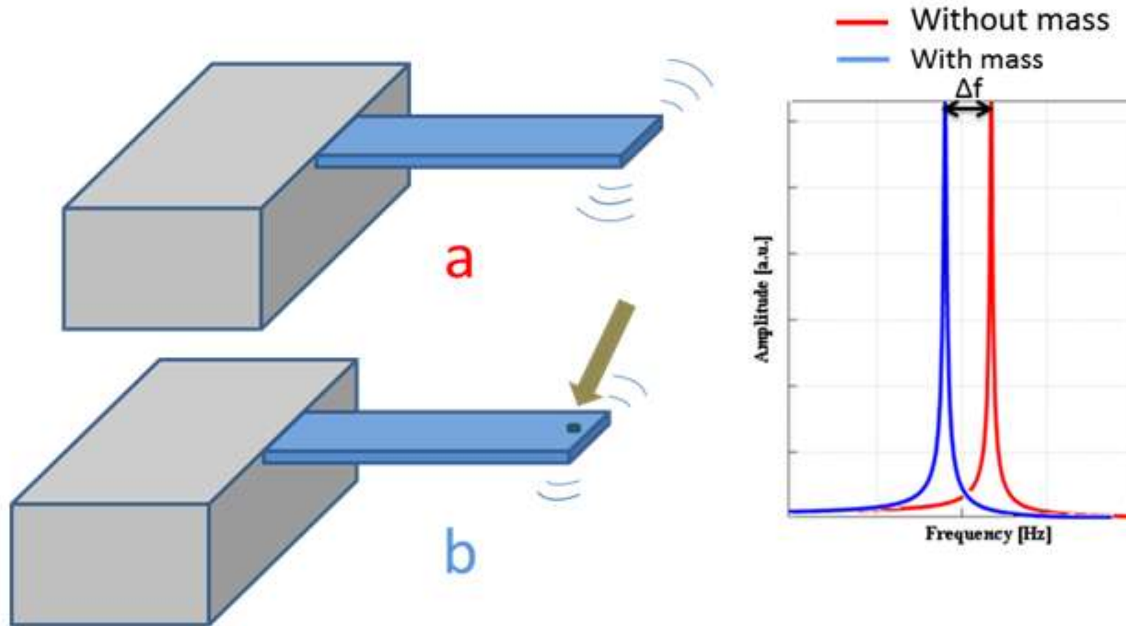

Figure 1.13: It is a sketch of the basic principle of mass detection cantilever. a) The cantilever is vibrating at a certain resonance frequency red curve plot. b) When a mass is loaded at the free end of the cantilever occurs a down-shifting of resonance frequency which corresponds to the blue curve plot.

The principle of a mass sensor based on a cantilever is shown in figure 1.13. The added mass is detected by the resonance frequency shift means, the resonance frequency depends on the structure of the device and the specific added mass. The interpretation is that the adsorption of a mass on the surface of the cantilever induces a decreasing of resonance frequency as illustrated in figure 1.13. There are other properties that affect the resonance frequency, such as the effective spring constant including spring softening/hardening, and especially the surface stress in the material with Q-factor and the drive schemes. By down-scaling of the cantilever, the resonance frequency will increase and thereby the sensitivity changes. This means that going from micro to nano-size cantilevers can increase the mass sensitivity from femtogram range to yoctogram-range (10^{-24}g). In the following the mass sensitivity of different type of mechanical resonators are presented.

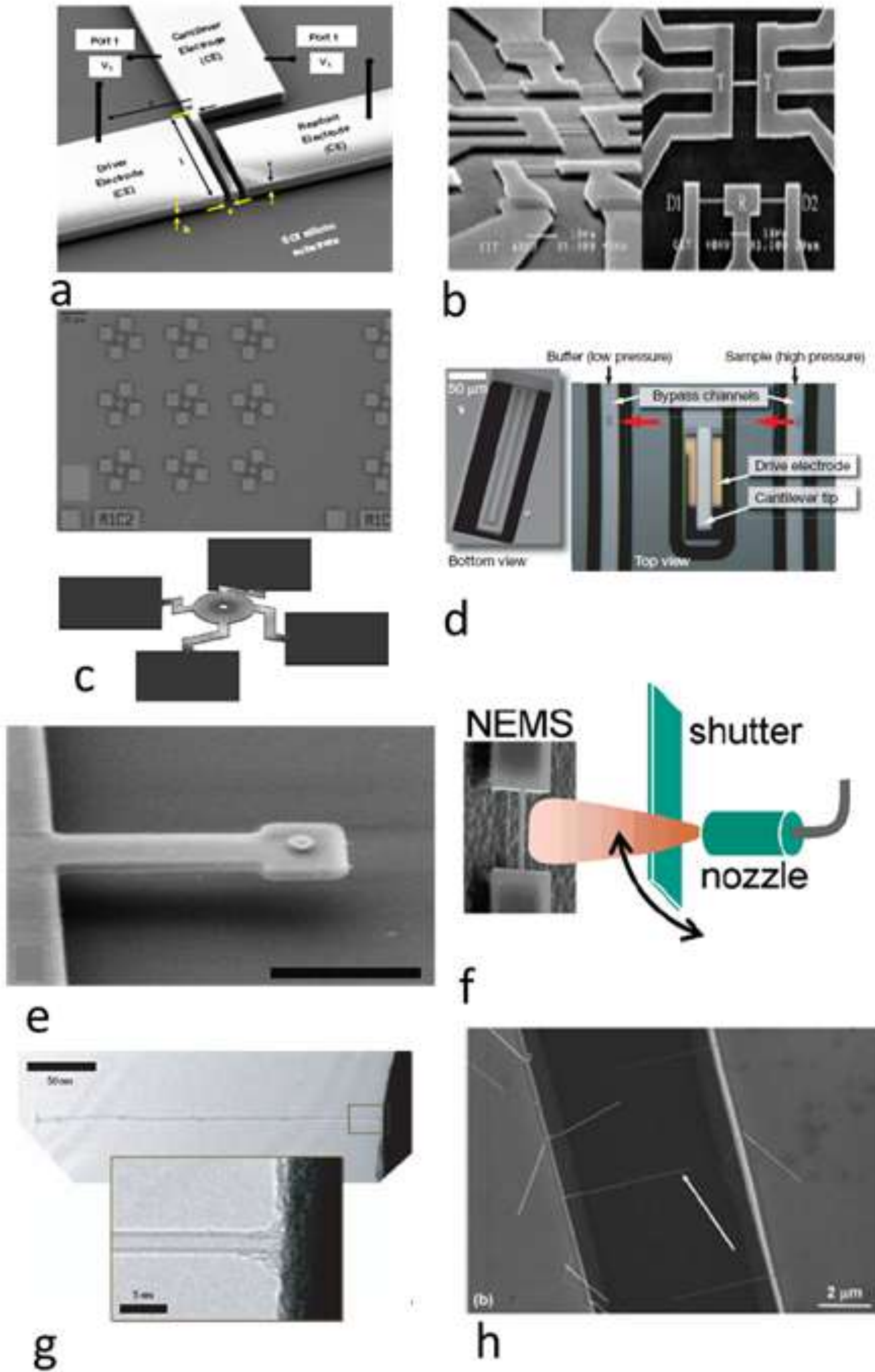

a) The mass responsitivity is increased by doping the cantilever. Thereby increases Q-factor. The resonance frequency of the cantilever is $f_{res,0V}$=1.6 MHz for zero voltage,

gives a mass responsitivity of the cantilever 0.3 fg/Hz. The length, thickness and thickness are l=40µm, w=2.3µm and t=5µm, respectively [83].

b) The SiC beam is double clamped. The resonator is in an ultra-high vacuum (UHV) environment. The adsorbed mass is Au atoms that are generated by a thermal evaporation source and travel towards the beam resonator. The mass of the Au atoms are modulated by a shutter which could be registered by QCM. The NEMS resonator is excited by RF bridge configuration and has a resonance frequency 32.8 MHz with a mass sensitivity 2.53ag [84].

c) The circular disk with four arms are used to measure the mass of a prostate specific antigen (PSA). The dimensions of the resonator is 6µm in diameter and the support arms are 1µm wide. The mass sensitivity (equation 2.10 to 2.12) increases by having thinner and lower density resonators. The large surface area is 54µm^2 will increase the probability of capturing analytes at extremely low concentrations, which may improve sensitivity. The resonator was able to detect and measure the weight PSA to 55 zg. It was mechanically excited by using PZT. The resonance frequency is 2.2 MHz and Q-factor 6000 [85].

d) A microchannel with walls 2-3µm thick inside the cantilever. Under each cantilever there is an electrostatic drive electrode and the cantilever vibration is detected by optical laser. The microfluid cantilever can be measured in air with water inside. The resonance frequencies are not significantly changed. The advantage of the device is that it can measure the mass of objects that are not attached to the surface. The device can measure with 300 ag precision. If the sizes of the microfluidic cantilever decreases the precision of the mass will increase. [86]

e) An oscillator has dimensions l=4µm, w=500nm and t= 160nm made of siliconnitride. Au dot is deposited on the paddle (1µmx1µm). This cantilever has a mass sensitivity 0.39 ag. The Au dot is used to measure the mass of thiolate self-assembled monolayers (SAM), and demonstrate single dsDNA molecule sensitivity [61].

f) The NEMS resonator is a double clamped beam. The dimensions of the beam is l= 2.3µm, w=150nm and t=70nm and 100nm. The resonance frequencies are 133MHz and 190MHz, respectively. The beam is actuated by RF-signal. The NEMS device is cryogenically cooled down and in a ultrahigh vacuum. The adsorbed masses are Xe and N_2 molecules that are flux controlled by a mechanically shutter and a gas nozzle. The device with 190 MHz is measured to 100 zg. The device with 133 MHz is measuring to 200 zg [16].

Some resonators were based on nanowires and nanotubes that have yoctogram-range (10^{-24} g) in mass sensitivity.

g) The double-walled nanotube is placed in a vacuum chamber, where the Au atoms can be evaporated during the oscillation. The initial resonance frequency is 328.5 MHz. The mass responsivity is 0.104 MHz/zg (1zg=1x10^{-24}kg). The evaporation is controlled by a mechanical shutter. The first time of opening of the shutter is measured to 51 Au atoms [87].
h) A cantilever nanowires are grown by CVD. The Si nanowires are actuated by peizoelectric element and detected by an optical laser. The resonance frequency of this nanowire is 2MHz. The dimensions of the nanowire is diameter=40nm and length = 5µm. This gives a mass sensitivity 10 zg [88].

Generally, the drawbacks of decreasing the dimensions of the cantilever will effect reduction in the sample volume, detectable mass density, limiting effective mass [89] and providing a high resonance frequency and Q-factor, but practically becomes difficult to fabricate as well as detection of the vibration movements.

Detectors based on two weakly coupled cantilevers have two major limitations. (1) Upon mass adsorption on one cantilever the initial symmetry is broken and the modes become localized: in particular the cantilever under-going mass adsorption will have a greater contribution to the high frequency mode while the reference cantilever will have a higher oscillation amplitude on the low frequency mode; however, both cantilevers retain a nonzero amplitude in their least significant mode and the mass adsorption event cannot be easily recognized. (2) Unless the frequency is tuned, e.g., by stressing one cantilever as already demonstrated for clamped beams [70.], the relative amplitude in the two modes is not controllable. Upon mass adsorption the amplitude variation is relatively small and depends on the initial amplitude.

In summary, we demonstrated reviewed the principal MEMS sensors, in particular cantilever based MEMS sensors and actuation strategies have been presented. The advantages of coupled cantilevers compared to single cantilevers have been elaborated. In this thesis, by considering several advantages and disadvantages, we have used triple coupled cantilever (TCC) sensor with optical and force gradient actuation strategies has been used for the mass detection. A detailed design and introduction about TCC is demonstrated in chapter 2.

1.6 Thesis overview

The aim of this project is to design and fabricate triple coupled cantilevers (TCC). Investigations of two actuation strategies are done. The one is with piezoelectric (pzt) and the second one is the optical (laser). Finally, a totally new actuation strategy has been implemented on the *SiN Electrodes TCC* design.

We will show through this thesis that TCC device is used for two applications. The first application is for mass detection and the second is for micromechanical transistor. The main focus has been on solving design and technological problems in fabrication process.

Three designs of TCC are:

- Fabrication of TCC in silicon-on-insulator (*SOI TCC*), and actuation methods were with piezoelectric (pzt) and optical (frequency puls-modulated laser) strategies. The read-out was done with a normal CW green laser.
- A new strategy of fabrication of TCC in silicon nitride (*SiN TCC*), the actuation strategy was made by optical laser.
- Further improvement of TCC design (*SiN Electrodes TCC*) was made to integrate the electrodes with the cantilevers. The new actuation (dielectric interaction) mechanism was possible to apply TCC device.

1.6.1 Outline of chapters

In **chapter two** the main points of microcantilever theory are analytically described for simple resonator structures, such as static and dynamic modes. The main damping factors (surrounding loss, structural damping and internal dissipation in a structure) in a microcantilever are explained and described. The mechanics of a microcantilever system is described. Theoretical explanations of choosing triple coupled cantilever configurations are given.

In **chapter three** finite element analysis is presented. In this chapter the eigenfrequency modes of TCC is simulated by using finite element method (FEM). This method gives us the advantage to optimize the design (width and length) of the overhang of the TCC

device. Several simulations were made such as the dependence of the displacement amplitude ratio of the cantilevers with respect to the added masses. The dependence of the dimensions of the overhang with respect to the frequency and displacement amplitudes.

In **chapter four** I will describe the fabrication process flow and the designs of TCC devices (*SOI TCC*, *SiN TCC* and *SiN Electrodes TCC*) in detail.

In **chapter five** I will explains both the experimental measurements of TCC devices and the experimental setup. The setup is custom built for frequency response measurement. The experimental results of *SOI TCC*, *SiN TCC* and *SiN Electrodes TCC* are shown in this chapter. There is a section with an optimization of the experimental setup with respect to the actuation methods (piezoelectric and optical) and the rotation of the photodetector. The *SiN TCC* is measured with two different sizes of silica beads for mass detection. The FIB process is also used for a better control of removing materials. The results of TCC devices are evaluated and discussed. Moreover, the chapter contains considerations and proposal of a micromechanical transistor. In the last section I will present the measurement done using another type of cantilever which has a paddle (200x200μm^2) that is suspended to a cantilever. These cantilever plus the paddle was used to grow cells on top of the paddle and to measure their dried mass.

In **chapter six** conclusions are drawn.

2 THEORY OF MICROCANTILEVERS

2.1 Introduction

Microcantilever sensors rely on their motion to indicate sensing, where the motion could be static deflection or dynamic oscillation in one or several resonance modes. Microcantilever can be modeled as a cantilever beam having thickness, width and length and fixed at one of its ends. This chapter describes the theory for the mechanical response of microcantilevers in bending, lateral and torsional modes and array coupled cantilevers when used as sensors.

2.2 Static Mode

Static deflection occurs due to differential surface stress. A beam which experience a different surface stress on two opposite sides, bends itself and the deflection *δ* is proportional to the differential stress *Δσ* according to the Stoney's equation:

$$\delta = \frac{3(1-v)}{E}\left(\frac{L}{t}\right)^2 \Delta\sigma \tag{2.1}$$

Where v is Poisson's ratio, E is Young's modulus, L is the beam length and t is the cantilever thickness. This model is valid also for microcantilever and by means of selective functionalization of one side of the cantilever it possible to transduce molecular adsorption to mechanical bending. The selective functionalization it is usually obtained by

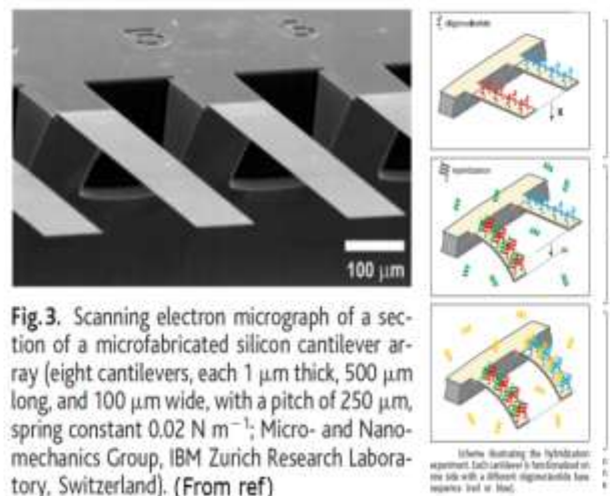

Fig. 3. Scanning electron micrograph of a section of a microfabricated silicon cantilever array (eight cantilevers, each 1 µm thick, 500 µm long, and 100 µm wide, with a pitch of 250 µm, spring constant 0.02 N m⁻¹; Micro- and Nanomechanics Group, IBM Zurich Research Laboratory, Switzerland). (From ref)

exploiting gold-thiol interaction. Probe molecules are functionalized with a thiol group and one side of the cantilever is coated with gold. Thiolated molecules covalently bind with the gold substrate. [21] Subsequently the target molecules bind to the probes. Each step induces a bending. Arrays of cantilevers allow to perform differential measurements to recognize different molecules.

2.3 Dynamic mode

Mechanical system responds to an external oscillating force with different amplitudes as a function of the frequency. The spectral distribution is characterized by peaks which are known as resonant frequencies which correspond to oscillating modes. Small driving force at the resonance can induce large oscillation. The load on the end of cantilever induces a deflection which is linearly proportional to the force applied [90]. Therefore, it is natural to introduce a lump element model to describe the dynamics of a cantilever. A dynamic mechanical system in the scope of this chapter will be dealing with an oscillatory mechanical microcantilever and is explained by a simplified model. This model contains a spring-mass-damper elements, as depicted in figure 2.1, which can be described by a second-order differential equation (2.2). On the left hand side of the equation (2.2) there are three different forces and on the right hand side there is an external force $f(\omega_{ext}t)$. This equation (2.2) is a well-known one in the classical mechanics: the second Newton's law.

The different forces are the inertial force $M\ddot{x}=F_I$, this term is a product of mass and acceleration, which is the kinetic energy of the system. The second term on the left hand side is the damping force $C\dot{x}=F_D$, which is a product of velocity and damping coefficient. The energy dissipates in the system due to the different damping mechanisms that will be treated later. There are many different models of the damping coefficients, but this is the commonly used one and it is easier to calculate the equation (2.2) in the analytical calculation. The third term on the left hand side is the restoring force $kx=F_k$, where k stands for the stiffness in the material, e.g. silicon, silicon-nitride etc. and x for the displacement from the equilibrium point which in cantilevers corresponds to cantilever deflection. The elastic deformation of the resonator during the mechanical vibrations gives a potential energy. This is another well-known law from the classical mechanics, which is called Hook's law. While the resonator oscillates there will automatically be a balance between the potential and kinetic energy. The required energy to oscillate the resonator comes from the external applied force, $f(\omega_{ext}t)$. All the terms are written in the following equation (2.2) [91].

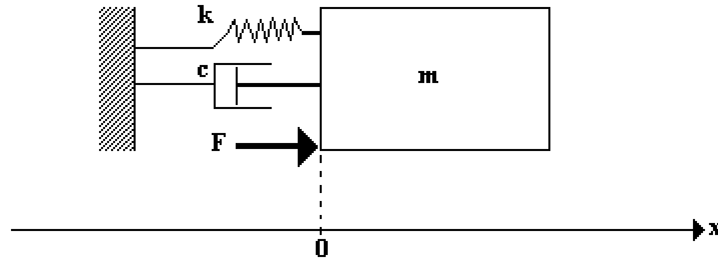

Figure 2.1: It is a schematic drawing of an oscillating resonator. The *m* is representing the resonator (microcantilever) which is connected to a spring, *k*, and dashpot, *c*. The resonator is moving in x-direction which is indicated by x. The external force is applied from the left (black arrow). This model is called Lumped-Element-Model.

$$\mathrm{m_{eff}\ddot{x} + c\dot{x} + kx = f(\omega_{ext}t)} \tag{2.2}$$

Where m_{eff} is the effective mass of the cantilever, k the spring constant, c is the damping, the $f(\omega_{ext}t)$ is the external force and angular frequency ω_{ext} angular frequency. The equation can be written into

The equation (2.2) is normalized with respect to the effective mass m_{eff}. Then the eqn. (2.2) is expressed in following equation (2.3)

$$\ddot{x} + \frac{c}{m_{eff}}\dot{x} + \frac{k}{m_{eff}}x = \frac{f(\boldsymbol{\omega_{ext}}t)}{m_{eff}} \tag{2.3}$$

$$\ddot{x} + 2\beta\omega_0\dot{x} + \omega_0^2 x = \frac{f(\boldsymbol{\omega_{ext}}t)}{m_{eff}} \tag{2.4}$$

Where ω_0 is the system's eigenfrequency and β is a damping factor of the system.

$$\beta = \frac{\mathrm{c}}{2m_{eff}\omega_0} \tag{2.5}$$

$$\omega_0 = \sqrt{\frac{k}{m_{eff}}}$$

The stationary solution for equation (2.4) is

$$x = A_0 \sin(\omega_{ext}t - \Theta) \tag{2.6}$$

After large t the transient is finished. This equation shows, A_0 the maximum oscillation amplitude of a mechanical resonator (cantilever) can be reached when the frequency of the external force, ω_{ext}, is matching with the natural frequency, ω_0, of the mechanical resonator (cantilever). This phenomenon is known as a resonance frequency, as illustrated in figure 2.2. The resonance frequency changes from different materials and dimensions of the mechanical resonators. In the energy distribution point of view the kinetic and potential energy is equally contributing at amplitude of the resonance frequency.

$$A_0 = \frac{F_0/m_{eff}}{\sqrt{(\omega_0^2-\omega_{ext}^2)^2+\beta^2\omega_{ext}^2}} \tag{2.7}$$

The phase of the oscillation amplitude is defined as

$$tan\theta = \frac{\beta\omega_{ext}}{\omega_0^2-\omega_{ext}^2} \tag{2.8}$$

Now, there are two variables that are called natural frequency ω_o, and damping ratio, β, [92,93]. The quality factor, Q, is defined as.

$$Q = \frac{1}{2\beta} \tag{2.9}$$

Further analyses show that the resonance frequency peak is dependent on the damping factor which is included in the equation (2.7). In an ideal system or in a simulation program can the damping parameter be described as zero ($\beta=0$). But in a real system there will always be a damping, which causes that the vibration of the cantilever or mechanical resonator decreases over a time.

2.4 Q-factor

The *Q*-factor or “quality” factor of the resonator is one of the most important factors in a mechanical resonator, because it is related on how sensitive the mechanical resonators are in the different environmental conditions. The definition of the *Q*-factor is the total energy stored, E_{tot}, in the resonator structure divided by the sum of the energy lost, ΔE, from the resonating element per cycle [75]. The *Q*-factor can be measured by looking at the amplitude vs. frequency spectrum of the resonator as seen in figure 2.2.

As the *Q*-factor changes its value, meaning that different dissipation mechanisms and intensities are involved, the oscillation amplitude and shape of a given resonance frequency is modified as a consequence, in figure 2.2 the *Q*-factor value is changed from 1 to 1000, from the orange curve to the red

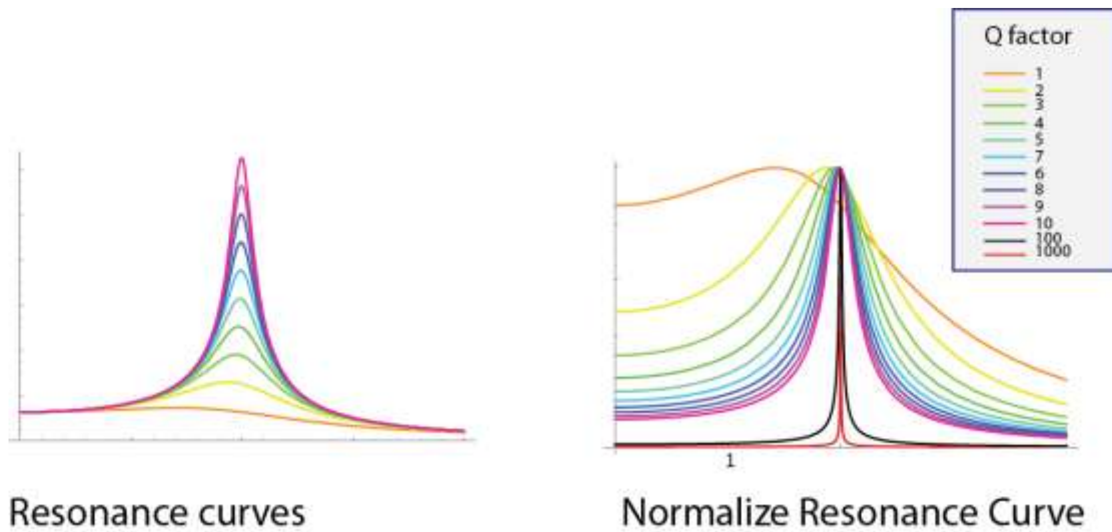

Figure 2.2: Oscillation amplitude vs. frequency spectrum. The Q-factor values are changed from 1 to 1000. The shape of the resonant frequency peaks are getting narrower.

The importance of the *Q*-factor can be observed in figure 2.2, since a high value of Q-factor gives a sharp resonant peak, which is needed to accurately measure a resonant frequency change (one-single-cantilever system). The *Q*-factor can be calculated in several ways. One of the methods is to find a resonant frequency, f_{res}, and divide this value by the bandwidth at the 3dB-amplitude point, Δf_{3dB}.The most common way is to take the width of the resonance frequency peak at full width half maximum (FWHM), as a direct measure of the damping of the system. Q is then the resonance frequency divided by the FWHM. The various definition of the *Q*-factor is given in equation (2.10):

$$Q = \frac{\omega_o}{\Delta\omega} = \frac{1}{2\xi} = \frac{f_0}{FWHM} \tag{2.10}$$

In a real cantilever system the main *Q*-factor contributions are described in the following. Other factors can further contribute but they will not be treated because of very less influence on the cantilever system during the vibration. The main influential *Q*-factors are the following:

1) Viscous and acoustic damping, Q_a,
2) Q_s, damping due to internal material parameters
3) Damping at the mechanical constraint, Q_i, such as crystal structure, lattice defects, etc.

The total *Q*-factor can be related to these individual Q-factors as $1/Q = 1/Q_a + 1/Q_s + 1/Q_i + \ldots$.

2.4.1 *The energy lost to a surrounding fluid ($1/Q_a$):*

The energy loss to the surrounding is the most important of the all the loss mechanisms. These losses appear between the resonator and the surrounding gas. The losses depend on the nature of the gas, surrounding gas pressure, size and shape of the resonator, the direction of the resonator's vibrations, and the surface of the resonator. In the case of vacuum these losses can be made negligible therefore for high sensitivity applications the micromechanical resonators are operated in the vacuum. Other damping mechanisms associated with surrounding fluids are acoustic waves and squeezed film damping.

2.4.2 *The energy coupled through the resonator's supports to a surrounding solid ($1/Q_s$):*

The structural damping is related to the resonator constraint to the substrate. The vibration energy of the resonator can be dissipated from the resonator through its supports to the surrounding structure. If the supports are carefully designed this dissipation mechanism can be significantly reduced. For instance, it possible to find the natural nodes in the vibrational movement of a resonator (non-vibrational-points), as illustrated in figure 2.3, where the supports can be placed to bond the resonator to the support.

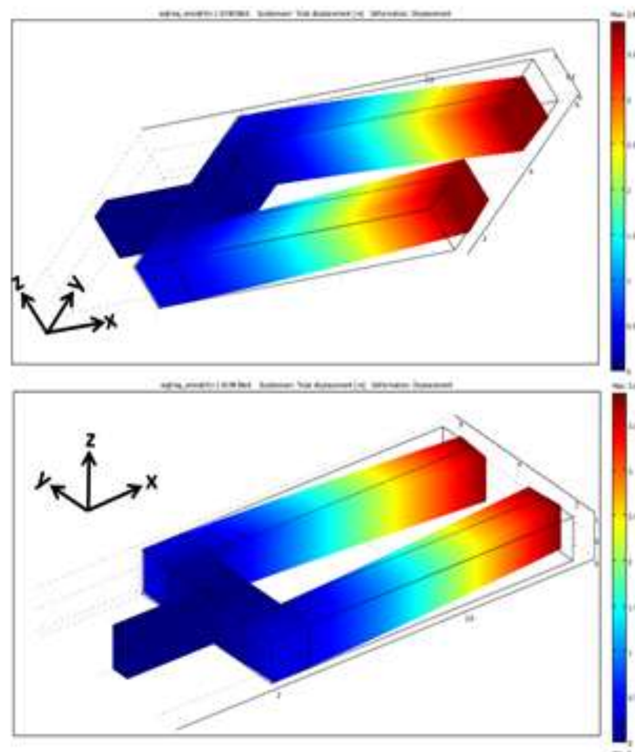

Figure 2.3: A tuning fork where the bottom of the base is fixed.

The figure 2.3 shows that a careful design can really minimize the energy dissipation in the supports. As it is illustrated in figure 2.3, the mechanical supports can be very important for a mechanical resonator in order to minimize the energy dissipation, thereby increase the *Q*-factor for the given mechanical resonator, in this case is a tuning fork.

2.4.3 The energy dissipated internally within the resonator's material ($1/Q_i$):

The last energy dissipation contributes come from the material of the resonator structure that can play role in the value of the Q-factor. The presence of impurities in the crystal can give lower Q-factor. It has been reported [75] that low-level impurity single-crystalline silicon have resonator Q-factors of approximately 10^6 in vacuum, while highly boron doped single-crystalline silicon resonators typically have a Q-factor of approximately 10^4. The conclusion is that the just impurities (boron-doped) could reduce the value of the Q-factor with factor 100

The main energy losses that could be considered in a micromechanical resonator system, combine together to the total quality factor, as in equation (2.11):

$$\frac{1}{Q} = \frac{1}{Q_a} + \frac{1}{Q_s} + \frac{1}{Q_i} \tag{2.11}$$

This equation expresses that the lowest *Q*-factor determines the total *Q*-factor. The most influential affect on the *Q*-factor is the viscous and acoustic damping, Q_a [94].
If the damping is negligible, the peak position of the lowest mode corresponds to the natural frequency and is given by:

$$f_0 = \frac{1}{2\pi}\sqrt{\frac{k}{m^*}} = \frac{1}{2\pi}\sqrt{\frac{E}{\rho}\frac{t}{L^2}} \tag{2.12}$$

Where ρ is the density, E is Young's modulus, t is thickness and L is the length of the cantilever. If the damping is not negligible the peak it is not at the natural frequency but is reduced by the factor $\sqrt{1-\frac{1}{4Q^2}}$ (For *Q*-factor of 10 the reduction is 0.12%, for *Q*-factor of 1000 is 0.12 ppm). The adsorption of molecules changes the shape of the resonance curves and thereby effects a shift in the resonance frequency. As first approximation, the mass of the resonator increases by the quantity Δm which corresponds to the mass of adsorbed molecules. According to equation 2.12 the resonance changes to the value:

$$f_{\Delta m} = \frac{1}{2\pi}\sqrt{\frac{k}{m^{*}+\Delta m}} \tag{2.13}$$

assuming the elastic constant does not change. If the added mass is much smaller than the mass of the resonator it is possible to obtain a linear relation between the shift in frequency and the variation of mass:

$$\frac{\Delta f}{f_0} = -\frac{1}{2}\frac{\Delta m}{m^0} \tag{2.14}$$

2.5 Mechanics of Cantilever Systems

We described the motion of a particular cantilever in detail with the motion equation (2.2) and with the corresponding damping parameter. The resonance frequency of a microcantilever depends on the geometry and material properties. In general, there are three fundamental resonance frequencies. The first is the bending in the vertical direction, the second is the lateral and the last is the torsional vibrations. These fundamental resonance frequencies characterize the dynamic motions of a given microcantilever. These resonance frequencies are called natural vibrations.

The resonance frequency of one cantilever is been fully explained in the previous section with the equations (2.2) to (2.9). The resonance frequencies of a single cantilever can be simulated as graphically in figures 2.4.

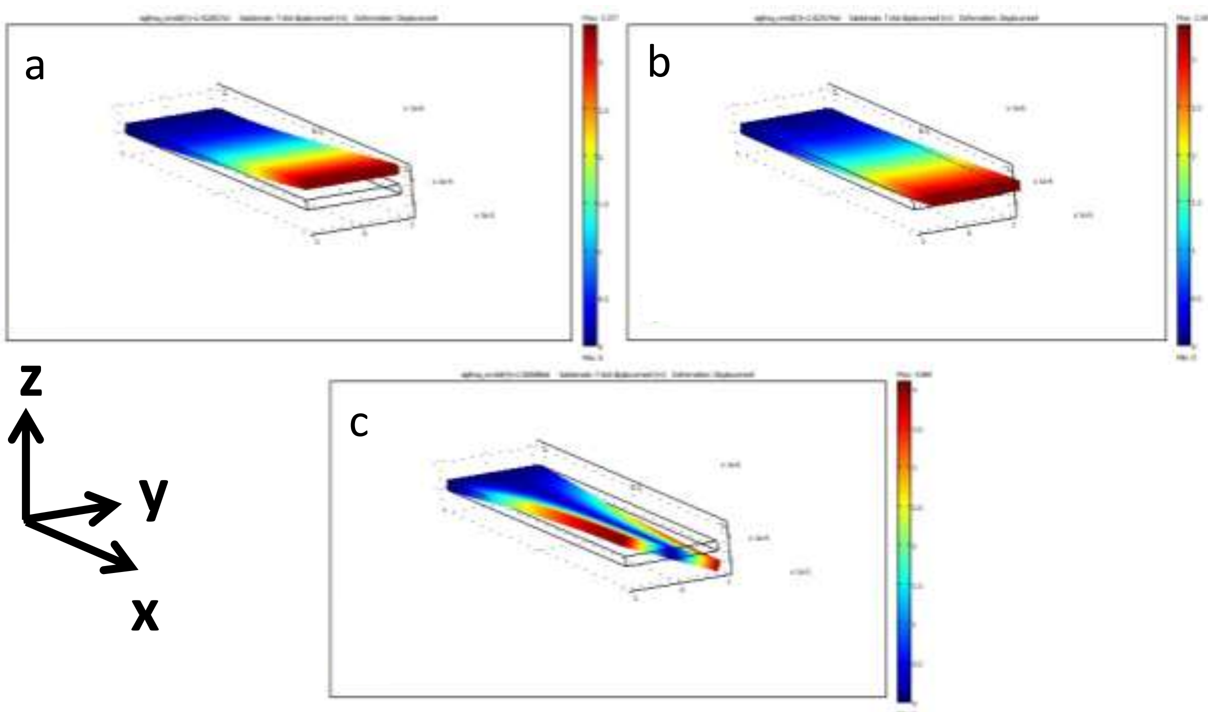

Figure 2.4: The resonance frequency modes of a microcantilever. The dimensions are 100x20x2µm^3. The colors scale is proportional to displacement from the rest position going from zero (blue) to maximum (red). The highest oscillation is at the free end. a) The first mode where the movement is in vertical (z) direction, b) the second mode is only moving in lateral (x and y) directions and c) the last eigenmode has a torsional (twisting) motion.

All the resonance frequencies that are shown in figure 2.4, can be calculated analytically, but when the structure of the mechanical resonator becomes complex, then it is difficult to calculate the eigenfrequencies analytically. Therefore, it is more convenient and less time-consuming to apply the Finite Element Method (FEM), which we have applied in order to find the fundamental of the vibrational modes. The FEM-software is used to solve the resonance frequencies of more complex structures of microcantilevers that are mechanically coupled together.

2.6 Triple Coupled Cantilevers (TCC)

The two coupled cantilevers by M. Spletzer *et al.* [68] have shown that it is more sensitive than the frequency shift method. A schematic lumped element model of two identical cantilevers are shown in figure 2.5a.

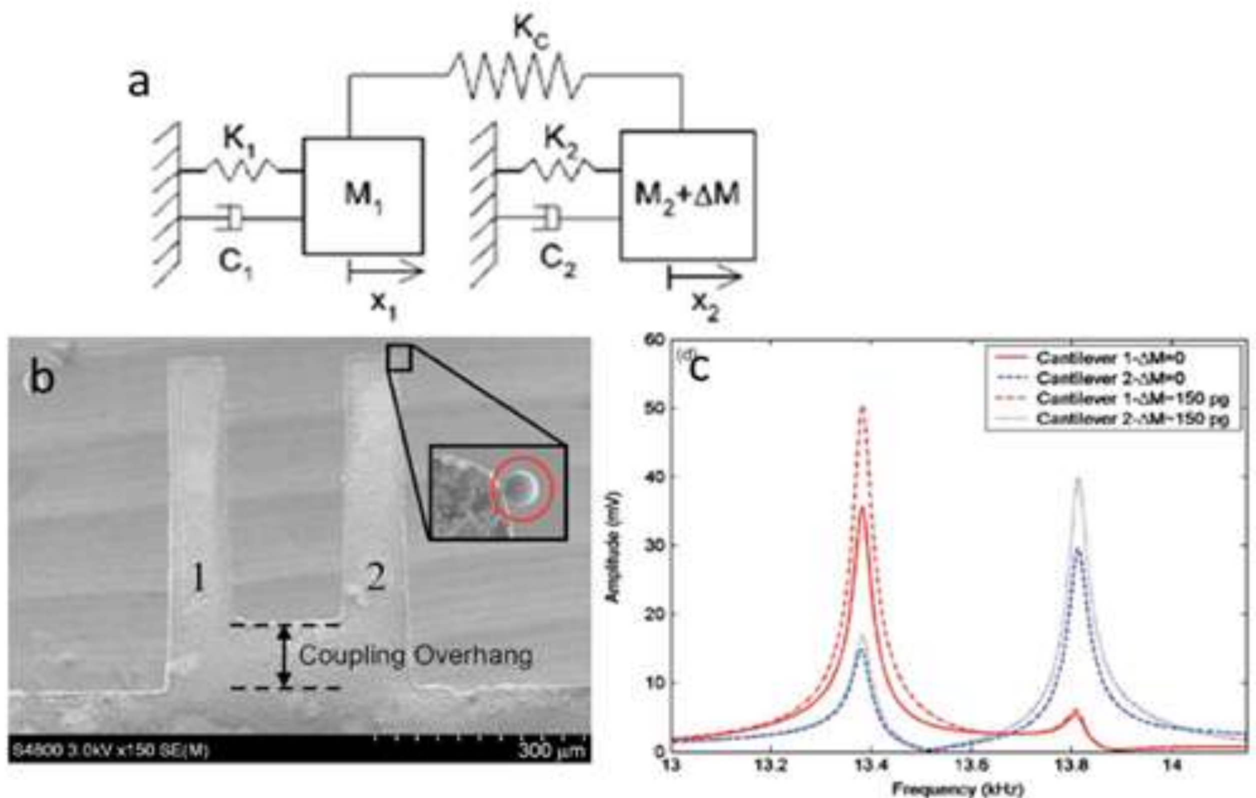

Figure 2.5: a) Schematic lump-element model of two identical coupled cantilevers. b) A SEM image of the coupled cantilevers with gold-foil on one of the corners. C) The measurement before and after the mass is added.

Each cantilever is represented by a mass and spring K_1, M_1 or K_2, M_2 respectively. If the added mass is zero $\Delta M=0$, the spring constants of each cantilever is $K=K_1=K_2$. The common

coupling is the overhang which has a spring constant K_c. The ΔM represents the added mass to the one of the cantilever as shown in figure 2.5a,b. If we are considering the first case where $K_1=K_2=K$, $M_1=M_2=M$ *and* $\Delta M=0$. Then the cantilevers have the same spring constants as well as masses and the oscillation amplitudes are shown in figure 2.5c that the lower frequency corresponds to a symmetric and in phase eigenmode, where in higher frequency corresponds to an antisymmetric and antiphase oscillation eigenmode. The point here is that none of these modes are localized because the amplitudes of the displacements of each mass (cantilever) are very close (in an ideal system the energy is equally partitioned between the two modes, thus high frequency amplitude should be smaller by a factor $(f_s/f_a)^{0.5}$). The second case is when the added mass is different from zero, $\Delta M\neq 0$, the spring constants and masses are different $K_1\neq K_2$, $M_1\neq M_2$, respectively. The added mass is breaking the symmetry of the system and results in plot in figure 2.5c. The dotted lines show the added mass localizes the eigenmodes, and it is clearly shown that the displacement amplitudes for either cantilever 1 or 2 in the corresponding eigenmodes oscillates more than the other.

Two important parameters can be expressed in term of the ratio $\kappa=K_c/K$. The shift of resonant frequency of the modes is given by $\Delta f/f_o = \pm 2\kappa$ and the minimum mass detectable $\Delta m/m$ is proportional to $K_c /(1+2K)$. It is clear that the mass sensitivity is maximized when the coupling goes to zero and the first and second mode are closer than f_0/Q = FWHM, or, in other words, are experimentally indistinguishable. In their paper, Gil-Santos and coworkers concluded that the two coupled cantilever system is never more sensitive than the single cantilever counterpart. Therefore we have purposed three independent identical cantilevers oscillate at the same frequency, see figure 2.6a. The spring elements are illustrating on the cantilevers. The oscillation is three-fold degenerate. By adding a coupling element, see figure 2.6b, the degeneracy is split and three distinct modes, with different symmetry are generated, as illustrated in figure 2.6.

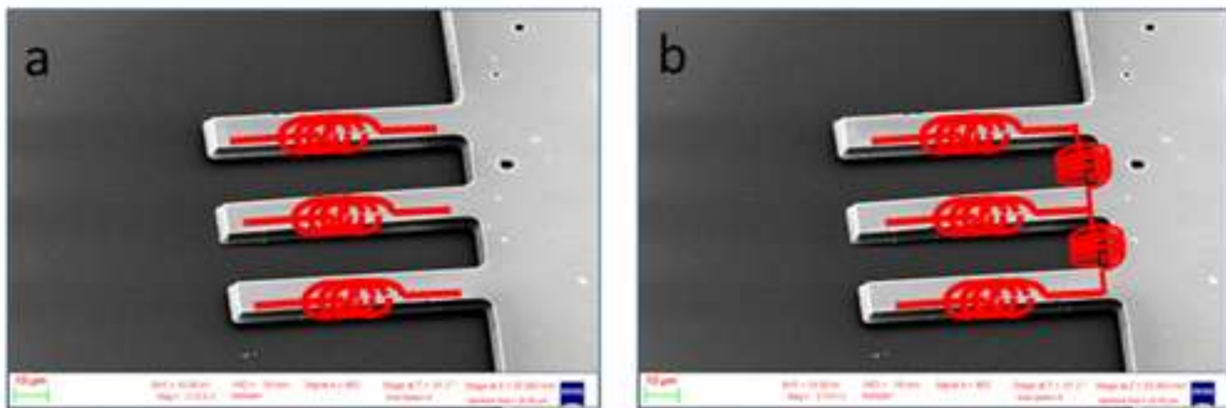

Figure 2.6: The a) picture is showing the cantilevers are not coupled and the cantilevers have the same resonance frequencies. In the b) picture the resonance frequencies are changed because of the coupling elements.

The three uncoupled cantilevers, figure 2.6a, are simulated in Comsol Multiphysics to illustrate that the three uncoupled cantilevers have the same oscillation amplitudes, as illustrated graphically in figure 2.6.

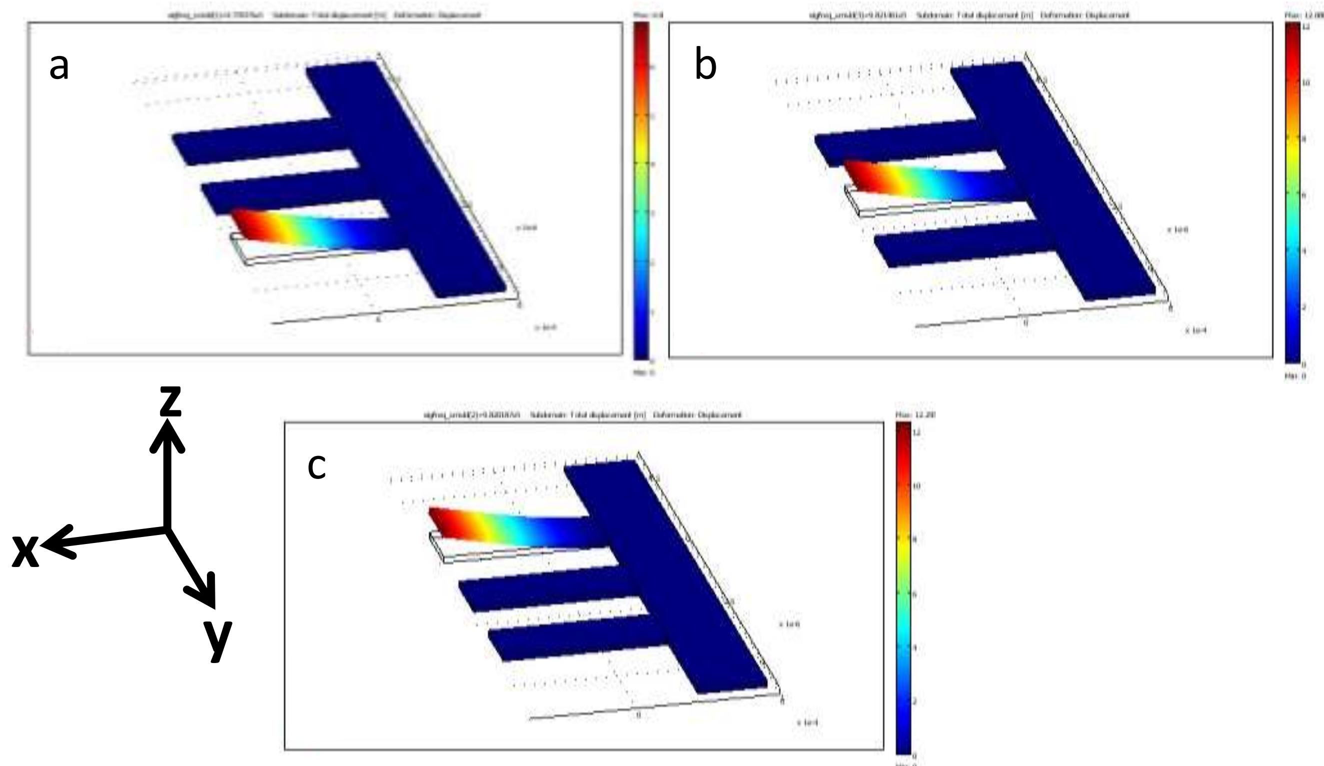

Figure 2.7: Three independent microcantilevers, where each of them is vibrating independently of each other. The maximum oscillation amplitudes are the same for all of cantilevers. These cantilevers are not coupled at all, therefore the resonance frequencies for identical independent cantilevers are the same.

The cantilevers are coupled as illustrated with coupling elements (springs) depicted in figure 2.6b, and thereby the dynamic behavior of each cantilever becomes dependent on each others. The resonance frequency as shown in figure 2.7, each cantilevers have their own resonance frequencies. With the coupling system the identical cantilevers have dependent resonance frequencies as illustrated in figure 2.8

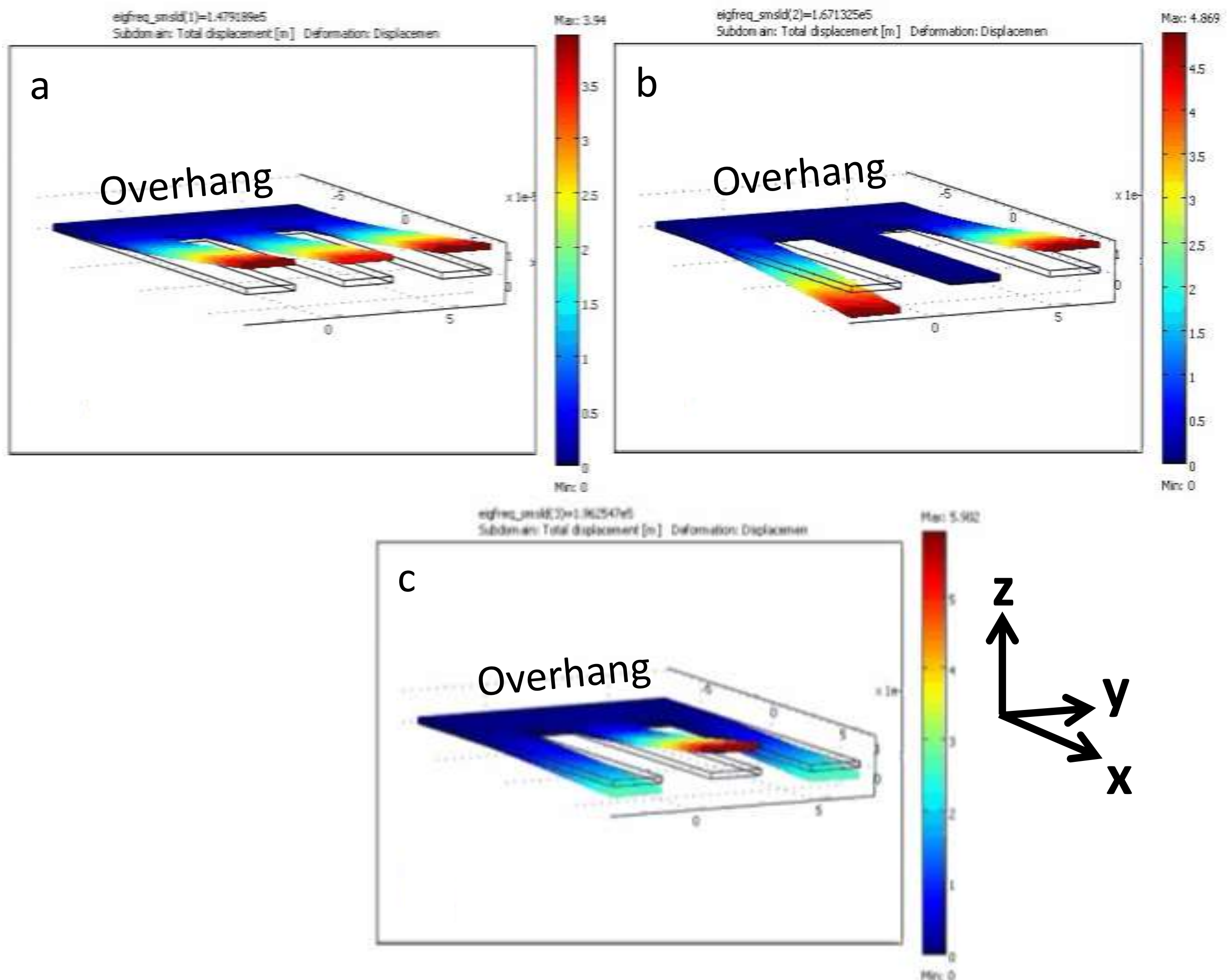

Figure 2.8: The three microcantilevers are connected at the common base, which is called overhang. With simulation program the correspondent frequency modes are simulated. In this case there are three fundamental resonance frequencies. The red color is indicating the maximum oscillation amplitude and the blue color is indicating the zero movement. a) the first mode which all the cantilevers are oscillating in the same phase and direction as called symmetric mode. b) the second mode shows that the lateral cantilevers are moving in antiphase and the central cantilever is not moving, also called antisymmetric mode. c) the third mode shows that the central cantilever is moving in antiphase to the lateral cantilevers. The lateral cantilevers are moving in the same direction and phase.

When the three identical microcantilevers are coupled as shown in figures 2.8, the mechanical behavior will be significantly changed from that of a single cantilever. The coupling gives three unique modes with distinct symmetry and increasing resonance frequency. The first mode is characterized by all the microcantilevers oscillating at the same amplitude and phase. The second mode shows that the central one is not moving and the lateral cantilevers are moving in antiphase. The third mode is showing that the central one is moving more than the lateral cantilevers. The lateral cantilevers are in the same phase than the central one.

In a conventional single cantilever system the detection of a mass is done by actuating the microcantilever and thereby detecting the oscillation by optical detection. The cantilever is measured before and after added mass. The frequency shift is calculated in order to find the

added mass.

Our proposal is an alternative way to detect masses without minimizing the dimensions of microcantilevers further or applying expensive equipments such as ultra high vacuum. The best performances and advantages of using a triple-coupled microcantilever systems are obtained when the microcantilevers are in the 2nd mode (or anti-symmetric mode), which is shown in figure. 2.8b. One of crucial step is the microfabrication process in order to fabricate perfect identical and symmetrical microcantilevers. In the simulation and experimental chapters will be explained in more detail.

3 SIMULATION OF TRIPLE COUPLED CANTILEVER (TCC) SYSTEMS

3.1 Introduction

The development of Finite Element Methods (FEM) spread the feasibility to design and develop various products in various fields, especially in MEMS field. Number of designs have been made in the area of BioMEMS, MOEMS, NEMS and is been continuing. Several FEM simulation tools including *ANSYS, Coventor, COMSOL Multiphysics* etc., are commercially available with several packages such as thermal, electromagnetic, microfluidics, structural mechanics environments. Mostly, in structural mechanics simulations, FEM helps excellently to understand the mechanical properties of the design with visualizations, and also in reducing the cost and materials.

Finite element analysis (FEA) is used for simulating a range of engineering applications, such as a mechanical structure. The structure is simulated and broken down into small elements, a process called meshing. The idea is to simulate geometries similar to the cantilever devices we have fabricated using microfabrication. The first step is to construct the structure of interest and mesh it by a suitable mesh size. An example of a cantilever structure and its mesh in COMSOL is shown in figure 3.1. The overall computational time depends on the size of the mesh.

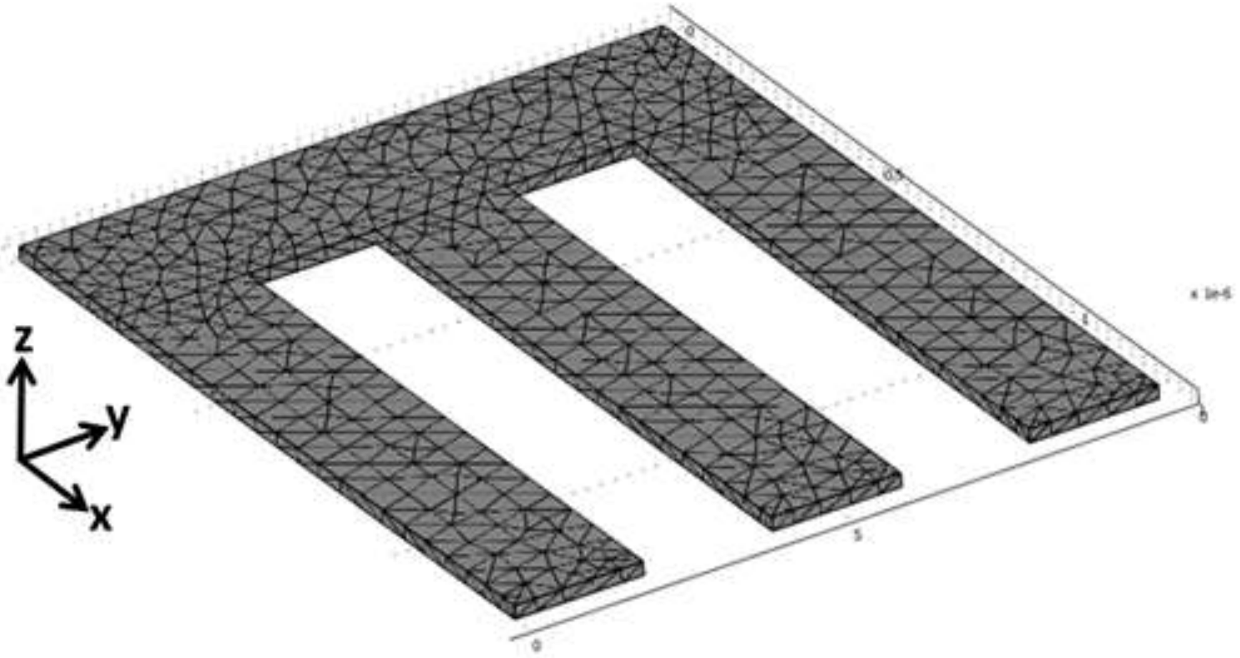

Figure 3.1: The model shows a mesh of TCC

COMSOL Multiphysics allows the users a detailed visualization of bends and twists of structures with the accuracy which is required for most of the applications. *COMSOL* allows entire designs to be constructed, refine and optimize whenever it is needed before going to fabricate the devices. In this project, *COMSOL* tool with structural mechanics package was used to design the TCC device. Also, various studies have performed such as dynamic behavior of TCC to find out the minimum and maximum range of the length and width of the overhang, vibrations in cantilever, symmetry break in the second mode, and finally relation between added mass on the lateral cantilever with respect to the central cantilever.

In this project, the TCC device has been modeled as shown in figure 3.2, simulations have been performed on the TCC before and after the added mass and investigated the dynamic behavior of the device, observed that placing additional mass on one of the lateral cantilever starts triggering the central cantilever. As shown clearly in figure 3.2, the overhang is mechanically connected with the three cantilevers.

The purpose of the simulation was threefold. We aimed at find:

1) The fundamental resonant frequencies of TCC.
2) The dependence of resonant frequency and of the coupling on the dimension of the overhang.

3) The relation between the added mass and oscillations of cantilevers especially, in the second mode for the central cantilever.

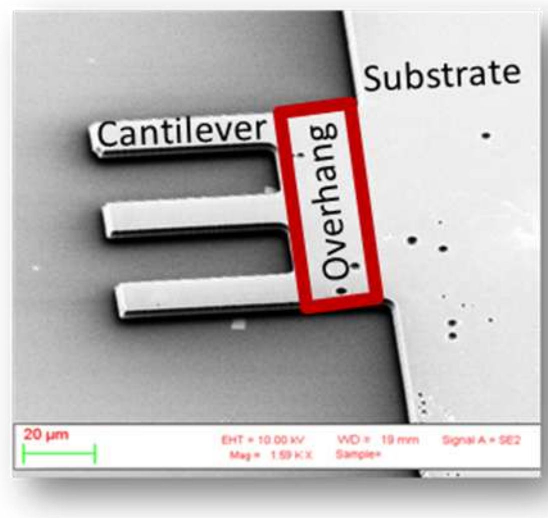

Figure 3.2: A SEM image of TCC. The overhang is framed in red rectangular shape and the overhang is attached to one side to the substrate.

3.2 Eigenfrequency Modes of TCC by using FEM Simulation

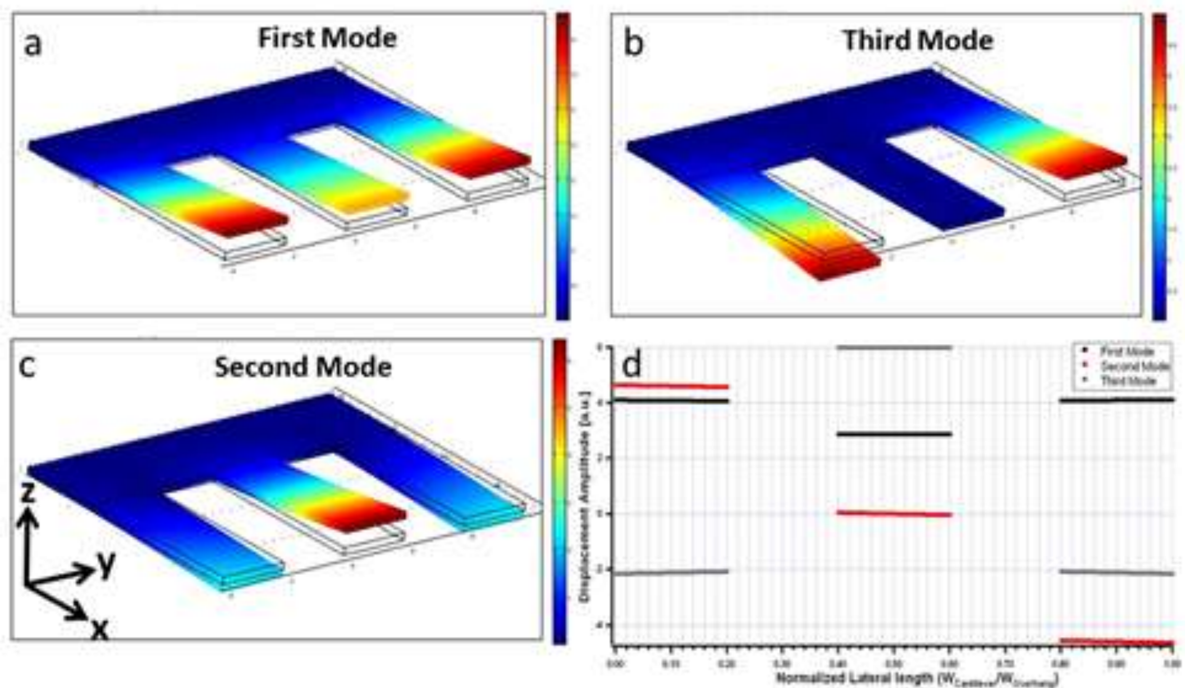

Figure 3.3: The three fundamental resonance frequencies are simulated by *Comsol Multiphysics*. Different colors are indicating the vibration of TCC. The blue color represents non-displacement and the red stands for the highest displacement of TCC. (a) Cantilevers are vibrating in the same direction and phase. This mode is called symmetric mode. (b) The lateral cantilevers are vibrating in antiphase. The central cantilever is in non-vibrating mode. This mode is called antisymmetric mode. (c) The lateral cantilevers are vibrating in the same directions and phases compared to the central cantilever. This mode is called third mode. (d) The oscillation amplitude vs. normalized width of each cantilever. The plots are taken from the displacement measured on the front-face of

each cantilever. All the modes are collected in one line plot, in order to have a better overview of all three modes. The first, second and third modes are black, red and grey colors, respectively.

We first observed that three cantilevers generates three different eigenmodes as clearly illustrated in figures 3.3, with corresponding shapes in figure 3.3a,b,c. The plots show the displacement from the equilibrium position in false colors from dark blue to red. The maximum displacement is localized at the free ends of the cantilevers. In the first mode all the three cantilevers are in phase as illustrated in figure 3.3a, but, the central cantilever has a lower oscillation amplitude in the first mode compared to the lateral (outer) cantilevers, as plotted in figure 3.3a,d in black color This lower oscillation amplitude of the central cantilever in the first eigenfrequency mode is related to the finite size of the overhang that do not extend laterally beyond the cantilevers. If the size of the overhang (125 microns) is bigger than the cantilevers, as illustrated in figure 3.4, then the difference in the displacement amplitudes in all the three cantilevers are the same in the first mode.

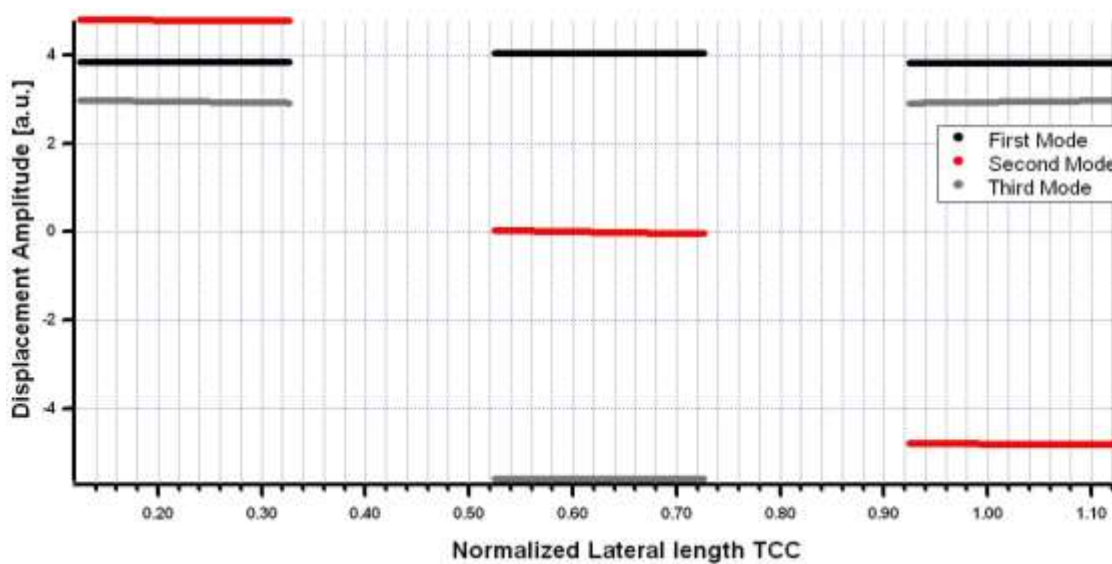

Figure 3.4: width of the cantilever are drawn with respect to the displacement amplitude.

This will be discussed in detail in the section of optimization of the overhang. In the second mode in figure 3.3b, the displacement of the central cantilever is on average equal to zero.
The third mode or the last fundamental mode of device, as shown in figure 3.3c the lateral cantilevers are in the same phase and the central cantilever is in opposite phase to the lateral cantilevers. Also for this mode, the extension of the overhang induce a more ideal ratio of the oscillation amplitude and the central one has nearly twice the amplitude of the lateral ones.

The plot in figure 3.3d report on the x-axis the y coordinate of the simulated structure and in the y-axis the displacement along z from the equilibrium position measured at the extreme

end of the cantilevers. The displacement is plotted only in correspondence of the cantilevers while no data are plotted for the gaps. These simulation results clearly show how the three coupled cantilevers of TCC device dynamically behaves. The main information we obtained is the existence of a not negligible tilt around the cantilever x-axis, especially in the second eigenmode. Here the central cantilever does not oscillate vertically but rotate along the central axis with the same frequency. The presence of this rotation will require particular attention in the measurement in laser deflection configuration, as we will see in the following. It is important to notice here that these movements are not related to torsional eigenmodes which have much higher resonance frequencies. These results are independent from the cantilever length since they provide qualitative information which is valid for any cantilever/overhang length.

3.3 Optimization of the overhang (width and length)

Overhang is nothing but a mechanical coupling of cantilevers. Overhang plays an important role in the operation of the TCC device. The dimension of overhang decides the oscillation amplitudes of each and every cantilever, as well as the amount of the frequency mode splitting as shown in figure 3.7. In the simulation, the external edge of the overhang shown in pink color in the figure 3.5 is fixed. There is only one boundary condition that is set to be zero, which means that all the other edges or boundaries are free to move, as in the real device. The three fundamental modes are obtained as represented in figure 3.3a,b and c. The width and length of overhang are defined and optimized and are plotted in figure 3.6 and 3.7, respectively.

The sequence of process steps performed using Comsol Multiphysics can be seen in the appendix A. It is investigated from the results shown in figure 3.7 primarily, the maximum and minimum width and lengths of overhang below certain stage effects the resonant frequency, next, the behavior of device seems constant as the length of the cantilevers vary from 50 to 100 microns. Results of TCC device having length of the cantilever 100 microns is shown here in figure 3.7 and lengths 50 microns and 75 microns respectively are presented in appendix B.

Simulation is the foundation for fabrication of device. Based on simulation knowledge, an approach is made to fabricate the device. In fabrication, it is to be observed the overhang is suspended to a membrane.

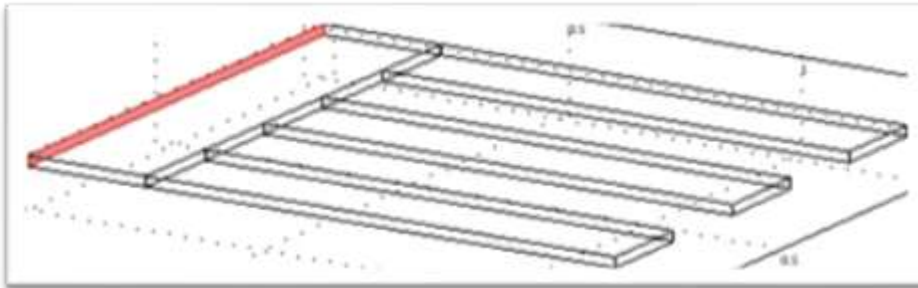

Figure 3.5: A typical drawing of a TCC device with the overhang. The pink color is showing the fixed edge. This means the edge is fixed to a suspended membrane. This can be done by setting the boundary condition be zero.

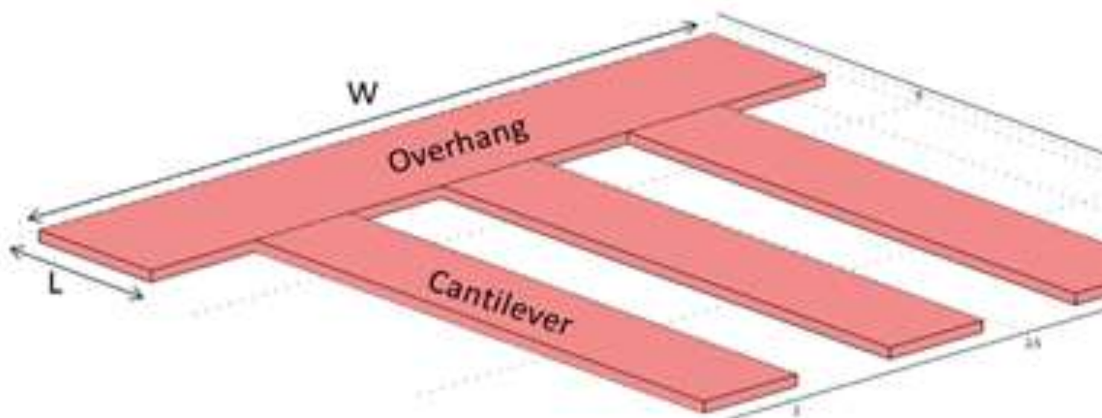

Figure 3.6: Definition of the width and length of the overhang is represented.

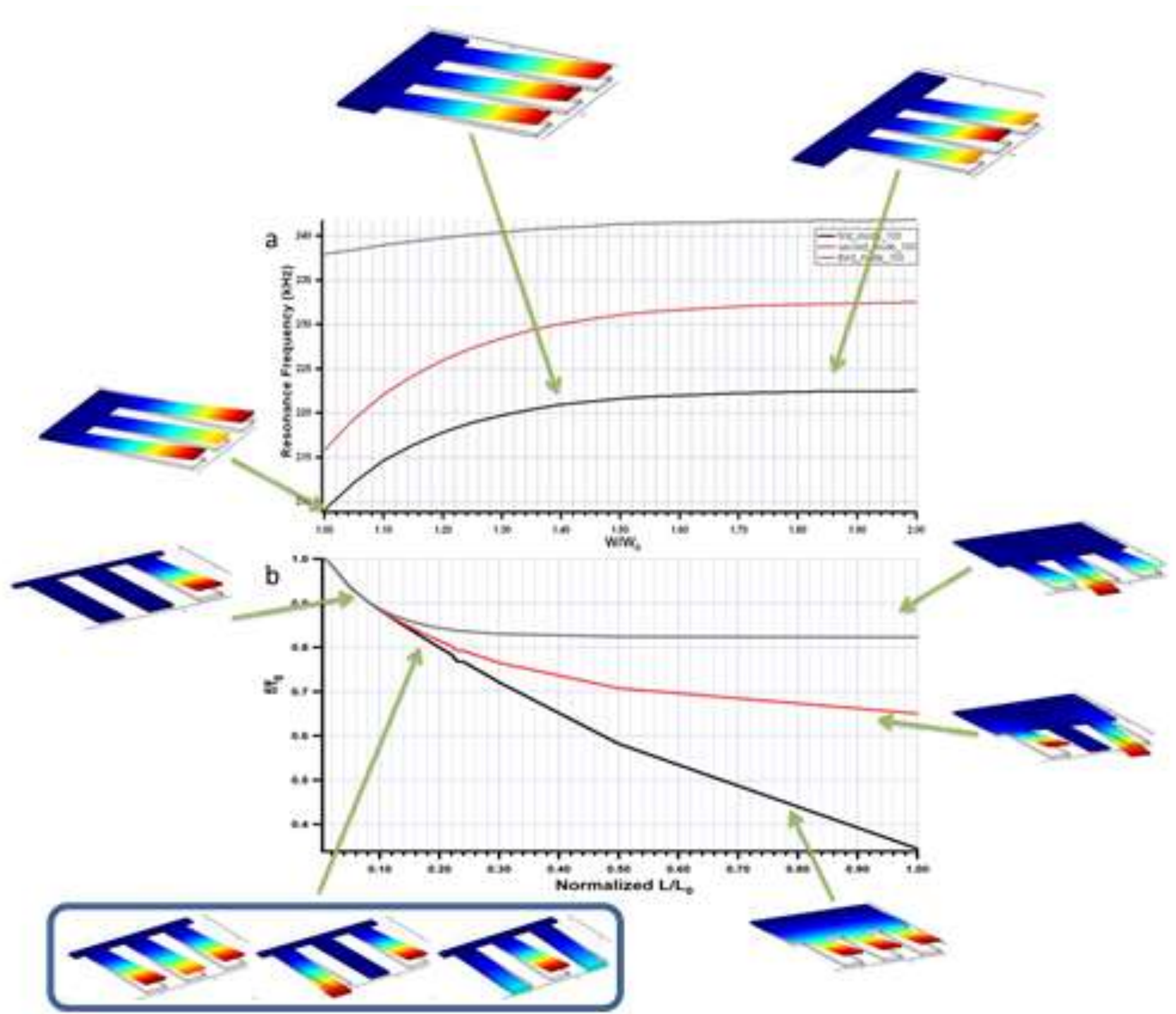

Figure 3.7: The eigenfrequency dependence on the width and the length of overhang are plotted a and b, respectively. The width is normalized to the width of TCC W_0 =100microns.The length is normalized to the length (100microns) of the cantilevers. The resonance frequencies are normalized. a) The resonance frequencies increase slowly while the overhang width outside the external cantilevers. When the extension is comparable with W_0 no further is observed in all three modes. Plot b) is showing the region 0.10 to 0.20 where the overhang length is optimal in order to achieve a coupling effect on all cantilevers. The region from 0.2 to 0.35 on plot b shows that the coupling is giving three distinct modes as illustrated in a frame. The small simulation images are showing the respective length and width of the overhang for all the modes that are plotted.

The width of the overhang in figure 3.7a, is varying from 100µm, which corresponds to overhang not exceeding the lateral limit of the left and right cantilevers to 200µm which corresponds to 50microns lateral extension of the overhang on both sides and is normalized. The symmetry of the structure is maintained. The resonance frequency of three modes is a function of normalized width of the overhang.

It is observed that in the initial point of the curve the resonance frequency depends on the width, means, is increased with the increase of the width of the overhang, as the extra overhang increases the rigidity of the systems. On the other hand, the extra mass added to the

system plays a minor role since it is placed in a region which is not subject to large oscillation. Interestingly, when the width of the overhang reaches a value $1.5W_0$ in all the three modes the curve starts to stabilize and/or saturate with respect to the resonance frequency. So, beyond the value $1.5W_0$ in all the three modes, it is confirmed the resonance frequency does not change significantly with increase in width. This information has been used for an optimized design and fabrication of device, has an optimal width with stable resonance frequency and the highest vibration amplitude. The next plot b), shows the effect of the length of the overhang. The length of the overhang and the resonance frequency are plotted in normalized units. There is a clear threshold for the onset of the cantilever coupling. For overhang length shorter than one tenth of the cantilever length the three modes are still degenerate in frequency and each one corresponds to the independent oscillation of one of the three cantilevers. At longer overhang the degeneracy is splitted and the three modes with different symmetry are observed. At increasing overhang length the resonance frequency for each mode decreases, which is the joined consequence of the system mass and system overall length increase, without a significant increase of longitudinal rigidity, as well as the frequency splitting between the three modes, which derives from an increase of the coupling constant.. With this information, it is possible to design and fabricate the optimized TCC device that has the highest sensitivity. The design and fabrication chapters, discuss how these values are used to design a TCC that is fully optimized in both width and length of the overhang. In particular, we choose to use the shorter possible overhang in order to reduce the system mass and thus increase the sensitivity and to keep the three frequencies as close as possible, so that they can be measured in a single frequency scan. The behavior oscillation amplitude with respect to the length of the overhang is also simulated.

Figure 3.8 shows the ratio between the amplitude of a lateral cantilever in the first mode versus that of the central cantilever in the second mode.

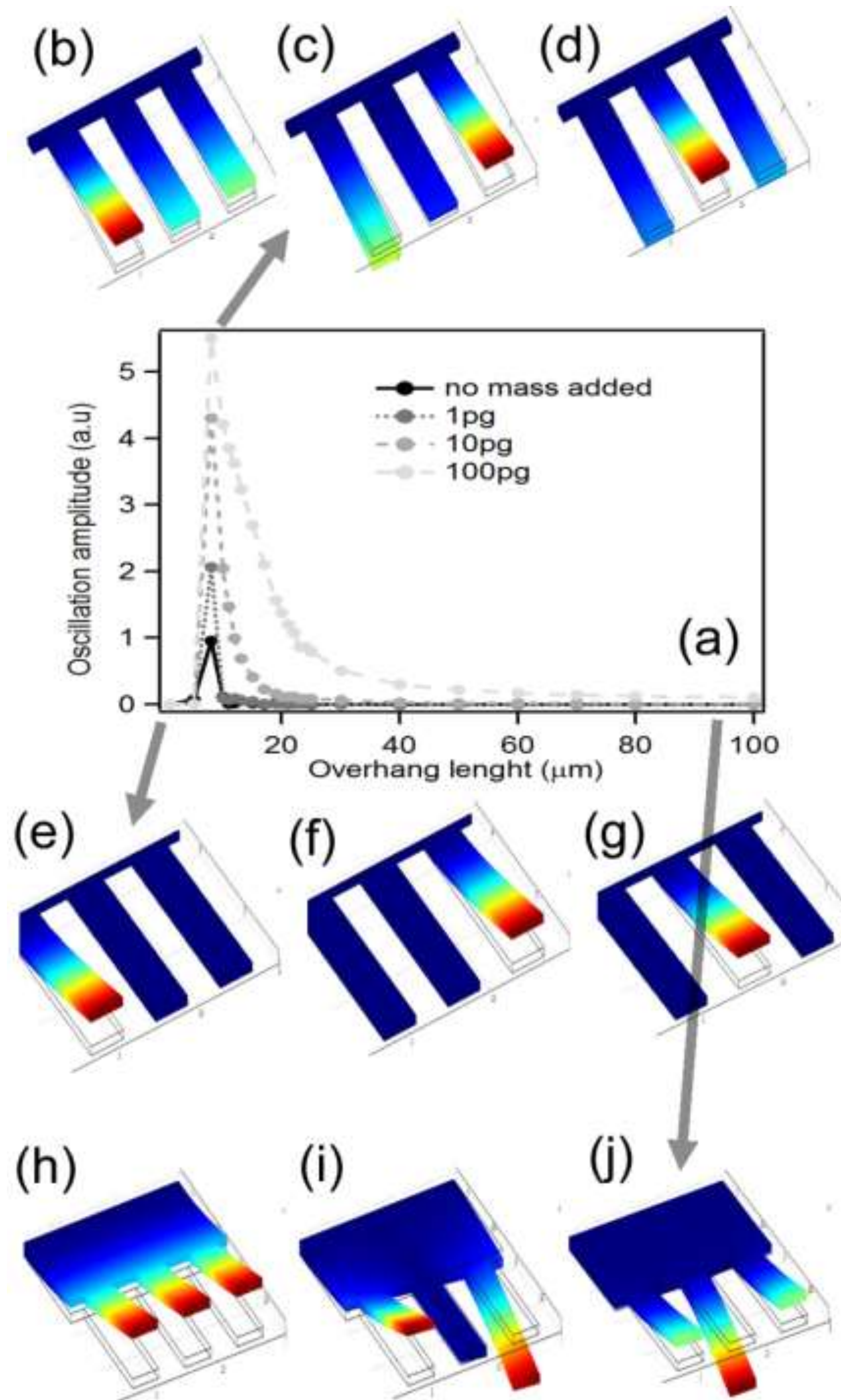

Figure 3.8: Oscillation amplitude versus overhang length in micro range. The different curves show the different added masses. The pictures around the curves are the simulations of the resonance frequency of first, second and third modes. The black continues line is without the mass has the smallest amplitude compared to the other added masses (1pg, 10pg and 100pg).

As discussed earlier, an approach is made to prove the TCC device can be used as a mass sensor. Simulations have been performed to investigate the performance of the TCC device. Different masses of 1pg, 10pg and 100pg are added to one of the lateral cantilevers. The results are shown in the figure 3.8. Different curves with different colors/sketches illustrate different masses added to one of the lateral cantilever. The curve with black color is a case of

TCC device, in which the lateral cantilever without mass. As it is observed, when the length of the overhang is below 10µm, the vibration amplitude is became zero in all the cases, includes even cantilever without mass. The inset simulation images in figure 3.8e, f and g, shows that TCC is behaving as a single, non-coupled individual cantilever system in all the three modes. The highest vibration amplitude ratio occur around 10-15µm in length of overhang. It is observed as the mass increases the oscillation amplitude increases. The inset simulation images in figure 3.8b, c, and d, are showing that the coupling effect is working on TCC. Then slowly the vibration amplitudes decrease and after 20µm, there is no affect on the vibration amplitudes observed as the length of the overhang increases in all the cases. The lowest peak value is when there is no mass. The highest peak value is due to heaviest mass i.e. 100 pg. It means increase in mass gives increase in oscillation amplitude in the lateral cantilever which is having no mass. An experiment is also performed with maximum applied length of overhang, which may be around 100 microns. The simulation images in figure 3.8h, i and j, shows the behavior of TCC when the overhang length is 100 microns. It gives the information about the limitation of the overhang length in all the cases so as to predict the device performance. From the figure 3.8 it emerged that the maximum variation of the amplitude ratio upon mass addition is in the region where the length of the overhang is around 0.2-0.4. For shorter length the modes are not completely formed, and the amplitude slightly depend on mass. For longer length the overhang contributes substantially to the cantilever motion and sensitivity decreases. The selected range of the length of overhang gives the necessary coupling effect to obtain the usual distinct modes with the highest vibration amplitudes.

It is also been performed some studies on the width of the overhang as shown in figure 3.9.

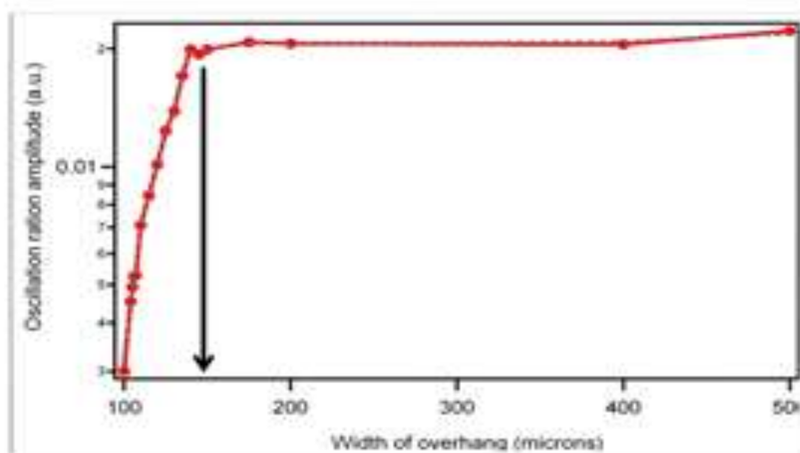

Figure 3.9: The oscillation amplitude ratio versus width of overhang in microns. The red dots are the simulation

points. The minimum value of the width of the overhang can only be 100µm.

It is observed from the plot in figure 3.9 that increasing the width of the overhang can increase the vibration amplitude less than a factor 7. The threshold value of the width of the overhang is 145µm: below this value the amplitude ratio decreases. Above this value the amplitude ratio does not change. This clearly conveys that the mass sensitivity can be improved 7 times. On the other hand, it is very important to note that the TCC device is very sensitive to any perturbation to the symmetry of the system, therefore it is very important to have reproducible fabrication process. The larger the microfabricated area, the more defect due to impurities, dust and errors. For these reasons we choose to sacrifice a factor 7 in sensitivity and to keep the overhang width at its minimum to reduce the probability of defect generation.

3.4 Added mass vs. Amplitude ratio

The difference in oscillation amplitudes of the central cantilever before and after that a mass is added will give the exact value of the added mass, this method is called for mode localization for the central cantilever. It is also possible to calculate the added mass by using the conventional method, in which shift in the frequency can be observed due to the application of added mass. One of the main advantages of TCC is that the added mass can be calculated in any kind of environment without losing resolution; this is described in the experimental results chapter. In this way it is possible to study the relation between the added mass on one of the lateral cantilever with the ratio amplitudes. The ratio amplitude is intended as the ratio of amplitude of the non-mass-lateral cantilever to the central cantilever. It is observed, as the added mass increases, the oscillation amplitude of the central cantilever increases, as illustrated in figure 3.10. The method used to realize the simulation is by adding an artificial mass in the form of a box with known fixed size. Instead of increasing the dimensions of the box, in this experiment, the mass density of the box is increased, thus avoiding differences in the mesh at different added mass. Indeed the FEM results in the TCC simulation are very sensitive to mesh. If the mesh is not sufficiently precise, it alone can break the symmetry in the structure, and thereby the central cantilever result as vibrating even without any additional added mass.

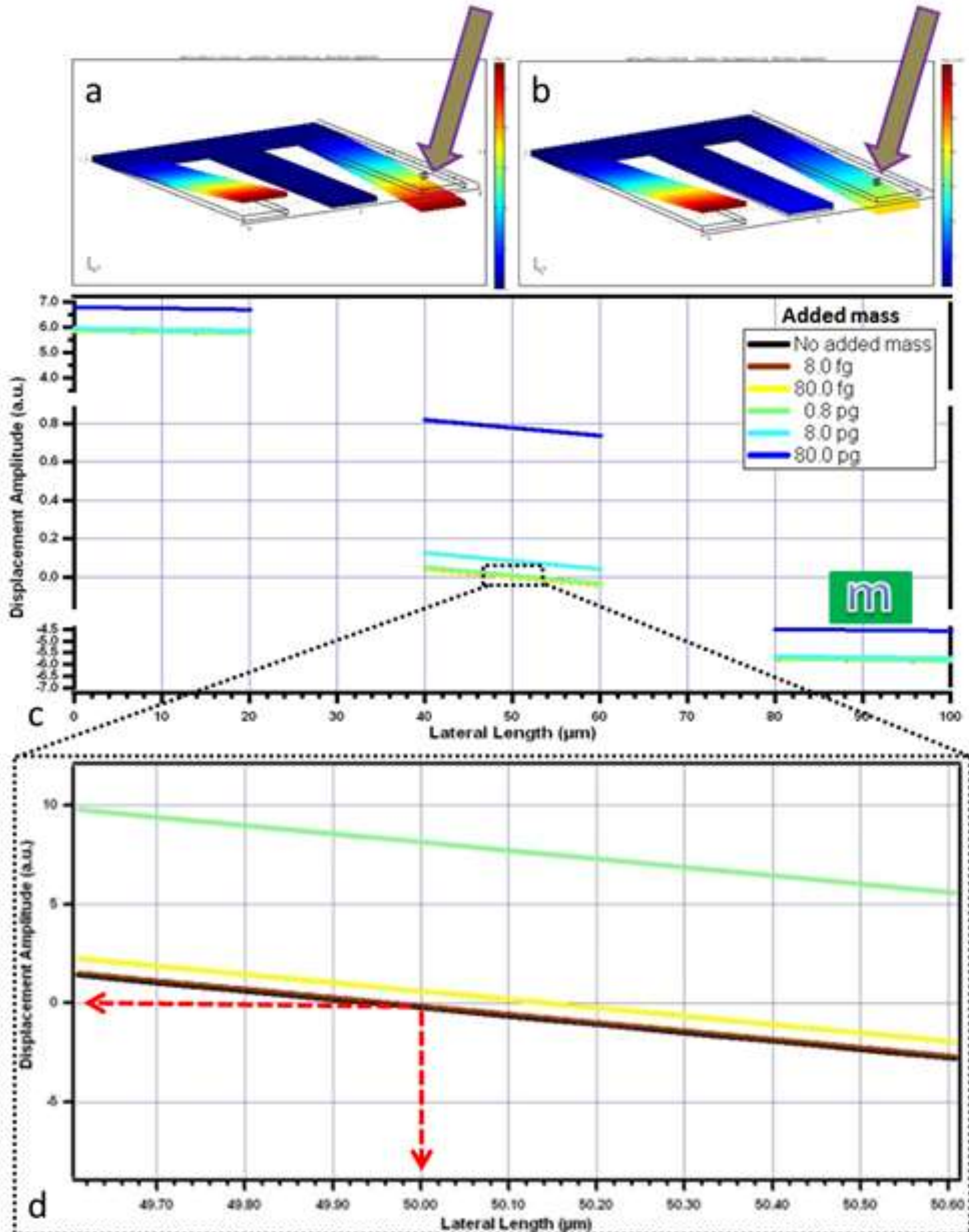

Figure 3.10: (a) This image is a simulation model of the TCC and the arrow is indicating the position of the additional mass. The central cantilever is moving but for the low range of added masses is not visible in this image. The added mass is 0.8 fg. (b) In this simulation image the added mass is 80 pg. The central cantilever is visible in this image. This is a snapshot of one particular mass density is added, just to show that the central cantilever is oscillating due the breaking symmetry. (c) The graph is a plot of the front-side-face of the three cantilevers. The lines are representing oscillation amplitudes. The additional mass is on the right side as drawn and shown in (a,b). As the added masses are increasing the oscillation amplitude of the central cantilever should also be increased, as the color is getting close to the blue. The black color is showing the zero mass condition and it is obvious that the structure is changed from added mass and after added mass.

A series of six simulations have been performed, added different masses: 0.8fg, 8.0fg, 80fg, 0.8pg, 8pg, 80pg to the cantilever shown in figure 3.10a. This particular TCC design in figure 3.10a has been used to demonstrate the sensitivity of mode localization in three coupled cantilevers configuration. The grey arrow in figure 3.10a, b is indicating the position of the additional mass on the lateral cantilever. It is observed that the amplitude of the central cantilever has been increased by the application of mass 0.8fg and 80.0pg respectively on the lateral cantilever as shown in the figure 3.10a and b. It is clearly observed that there is vibration of the central cantilever when the mass is zero.
The position of added mass (box) is approximately close to the free end as at this particular position the cantilevers have the highest oscillation amplitude. An attempt is made, all three cantilevers are drawn from the front-face-side for the second mode in all six different added masses are plotted in one plot as illustrated in figure 3.10c. In this way, the vibration amplitude of the central cantilever can be observed as added mass is increasing. An interesting observation is that vibration amplitude of the *added-mass-lateral-cantilever* decrease with mass addition, while that of the *not-added-mass-lateral-cantilever* increases as a result of center of mass balancing during oscillation. Also, as shown in figure 3.10d, a tilt in the central cantilever is observed before and after deposition of the mass on the lateral cantilever. Hence, it is concluded that the second mode of TCC design can be used as mass detection sensor.

As shown in figure 3.10, that adding mass on the lateral cantilever will disturb the symmetry of TCC, and the consequence is that the central cantilever starts to vibrate. The figure 3.10 has also shown that adding more masses increases the vibration amplitude of the central cantilever. The vibration amplitude of the non-mass lateral cantilever is in percentage less increased compared to the central cantilever. The mass of box on 2x2x2μm^3, with the same material as used for TCC, but the density is changed. By changing the density of the box, changes the mass of the box, and thereby the amplitude of the central cantilever increases, as illustrated in figure 3.11.

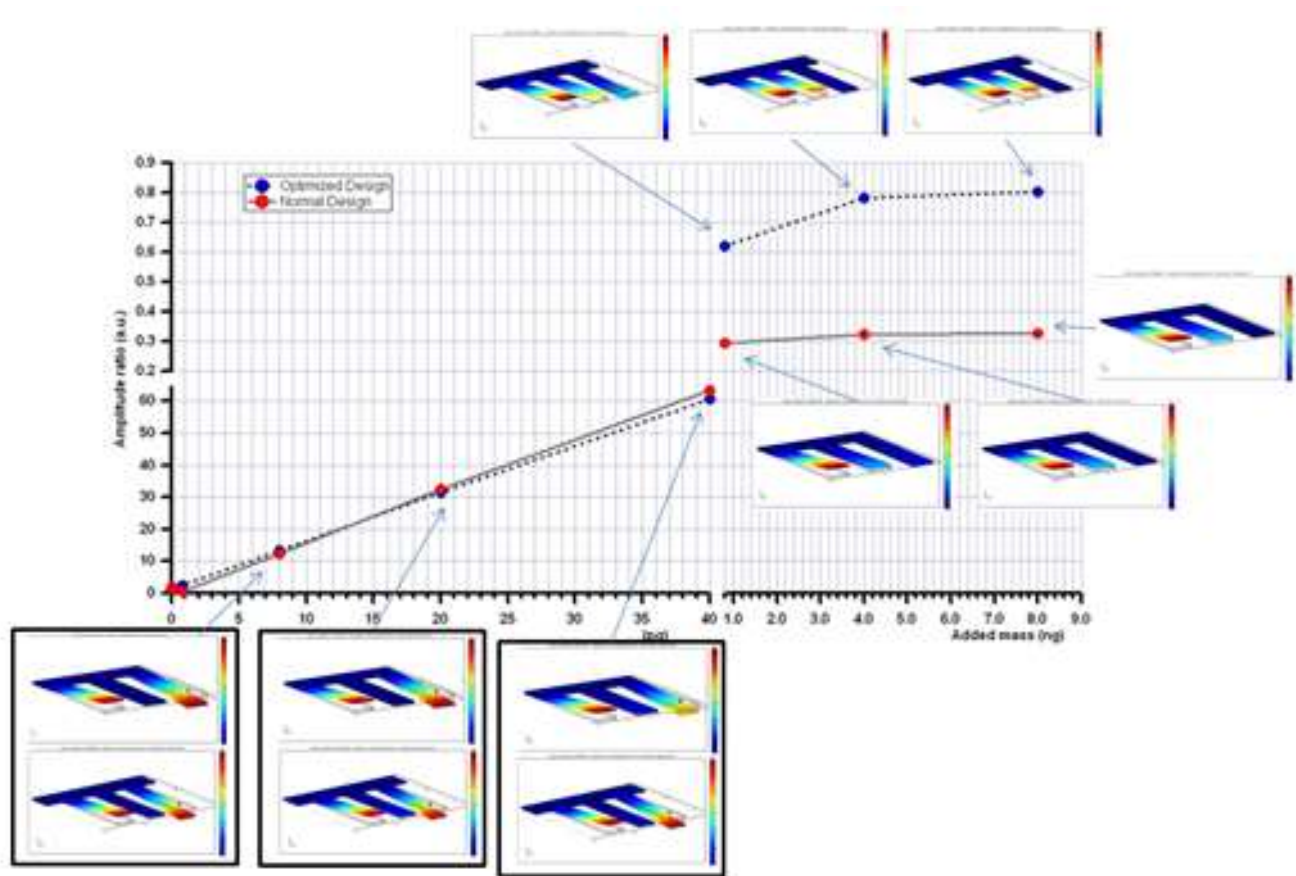

Figure 3.11: Amplitude ratio of central and non-mass lateral cantilevers versus additional mass. The FEM is performed on two different designs. The red dots are illustrating the normal design of TCC and the blue dots are illustrating the optimized design of TCC. The amplitude of central cantilever is increasing in picograms range (pg) in both designs. The amplitude for both designs are saturated in nanograms range (ng). In the pg-range the amplitude ratio is linear, where the central cantilever is increasing, and in the ng-range, where the amplitude of the central cantilever is reaching almost the non-mass-lateral cantilever. It shows that the optimized design that the amplitude of the central is reaching the non-mass lateral cantilever. By adding more masses turns TCC to uncoupled system.

The mass sensitivity of TCC is determined by taking the amplitude of the central cantilever with respect to the non-mass lateral cantilever by gradually increasing the added masses on the lateral cantilever as shown in figure 3.11.

In order to understand the performance of the TCC device as a mass sensor, two designs have been simulated. The major difference between the two is the dimension of the overhang. The first design and second designs have the widths of the overhang of 100 microns and 140 microns respectively, which are represented with red and blue dots.

As shown in figure 3.11, a huge difference is observed in ratio amplitude between two designs in a ng range. On the other hand, there is no much difference is observed in the pg range. And also an experiment has been performed with two different designs with varying the width of the overhang to estimate the ratio amplitude of the TCC.

From this it can be concluded that there is no significant improvements observed in ratio amplitude between two designs in pg range. In the ng range, the ratio amplitude is not only depending on the added mass but also on the width of the overhang. So, it can be finalized that the TCC device no longer will work as mass sensor in a ng range and also no coupling effect can be maintained between the cantilevers as shown in the inset simulation images in figure 3.11 and figure 3.12. It should be noted, masses in fg range can be measured comfortably using the proposed design, shown the figure 3.12.

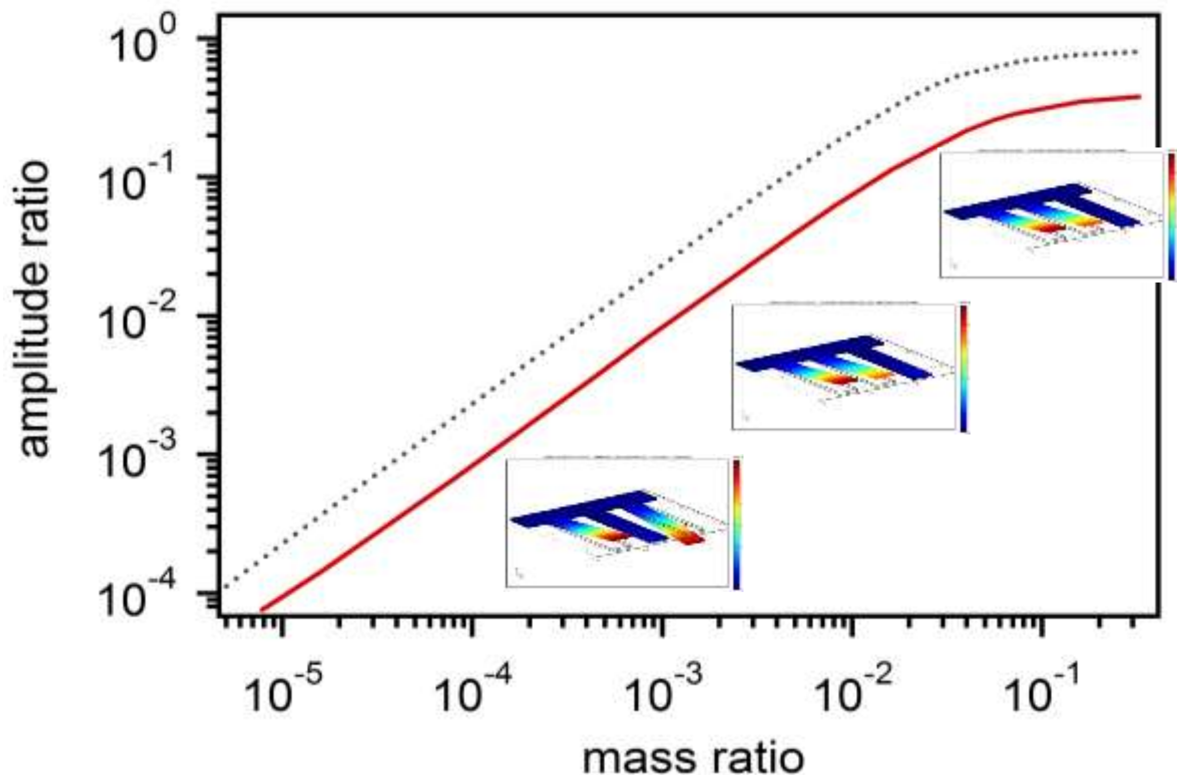

Figure 3.12: Mass response expressed as the ratio of the amplitude in the second mode and the first mode measured on the central cantilever versus the added mass express as a fraction of the cantilever mass. Dotted line: overhang length 0.2; solid line: overhang length 0.4. The three oscillation mode sketched in the inset refer to a situation in which the added mass is larger than 1% of the cantilever mass. In the lower frequency mode only the loaded cantilever oscillate (left inset). At higher frequency the two unloaded cantilevers oscillate as two coupled oscillator with quasi-symmetric (central inset) and quasi-antisymmetric (right inset) character.

It must be noted that in the real world it is demanding to fabricate the proposed TCC device as there is always a movement of central cantilever due to the uncontrolled parameters influences during the process of fabrication. However, in this project, at most care has been taken to fabricate TCC device that can measure up to pg range, more details about the fabrication process flow is discussed in the forthcoming chapters.

In conclusion, the detection of few molecules pushed the development of more and more sensitive devices, which have been pursued mainly through downscaling of the devices. In this thesis, the mass detection has shown that vibration localization in coupled

microcantilevers could represent an alternative strategy as a mass detection sensor.

4 DESIGN AND FABRICATION PROCESS OF TCC

4.1 Introduction

Microfabrication is at the basis of the Micro Electro Mechanical Systems (MEMS) technology and is constituted by all the techniques which permit to fabricate structures with dimensions from sub-millimiters to sub-microns. Microfabrication takes place in a particular environment called “clean room” where particle, temperature and humidity are controlled. In fact, if dust particles, which have dimension comparable with microstructure, land on a micro fabricated device, they will ruin it. Moreover, in order to obtain robust and repeatable processes, temperature and humidity must have always the same value with very low fluctuations. The most studied and used material for fabrication is single crystalline silicon. Another common substrate in MEMS technology is silicon on insulator (SOI). It consists in a thick wafer of silicon covered by a thin thermal silicon oxide and of a thin crystalline layer of silicon which may have several different crystallographic orientation in the device layer while the thicker handle layer can be maintained on the most common <100> substrate. It widely used in MEMS because by removing the insulator layer (called in this contest sacrificial layer) it possible to make suspended structure. There are three fundamental processes: lithography, etching and film deposition.

The fabrication approach used in MEMS devices can be classified into three general types; bulk micromachining [95], surface micromachining [96] and high-aspect-ratio micromachining (HARM) [97]. MEMS fabrication is similar to the fabrication of integrated circuits, involves the addition or subtraction of two dimensional layers on/from a substrate (usually silicon) based on photolithography and chemical etching. As a result, the 3 dimensional aspects of MEMS devices can be due to patterning and interaction of many 2D layers. If required, additional layers may also be added using a variety of thin-film and bonding techniques as well as by etching through sacrificial layers. On the other hand, the

complexity of the device may increase by the addition of independent structural layers.

4.1.1 Photolithography [98]:

A thin layer of an organic polymer, which is very sensitive to UV (ultraviolet) radiation, is deposited on Silicon nitride or Silicon; this is called a photoresist (PR) and can be either *negative* or *positive:* in positive PR polymer chains are broken by UV radiation, and become soluble in specific solvents, named developer so that the exposed region can be removed. In negative photoresist the polymers are cross-linked upon UV exposure and become insoluble while the unexposed areas can be removed. A photolithographic mask made up of a quartz (glass plate) which is a transparent in the UV spectral region, coated with a chromium pattern (opaque), is placed in contact with the photoresist coated surface. The wafer is exposed to the ultraviolet radiation transferring the pattern from the mask to the PR which is then developed. On developing, the rinsing solution removes either the exposed areas or the unexposed areas of PR leaving a pattern of bare and PR-coated Silicon nitride or Silicon on the surface of the wafer. The resultant PR pattern is either the positive or negative image of the original pattern of the photomask. The details of photolithographic process of TCC device is explained in the forthcoming topics.

4.1.2 Bulk Micromachining Technique [95]:

Bulk micromachining involves the removal of part of the substrate. It is a process that uses dry etching or a wet etching method.

Dry etching depends on vapour phase or plasma-based methods of etching using suitable reactive gases usually at high temperatures. The most common form for MEMS is Reactive Ion Etching (RIE) which utilizes additional energy in the form of Radio Frequency (RF) power to drive the chemical reaction. Energetic ions are accelerated towards the sample to be etched within a plasma phase supplying the additional energy needed for the reaction; as a result the etching can occur at much lower temperatures (typically 150^0C - 250^0C, sometimes room temperature) than those usually needed (above 1000^0C). RIE is not limited by the crystal planes in the silicon, and as a result, deep trenches and pits, or arbitrary shapes with vertical walls can be etched [99].

4.1.3 Wet Etching [100]:

Wet etching involves the removal of material through the immersion of a material (typically a silicon or silicon nitride wafer) in a solution of a chemical etchant. These etchants can be isotropic or anisotropic.

Isotropic etchants etch the material at the same rate in all directions, and consequently remove material under the etch masks at the same rate as they etch through the material; this is known as undercut. The most common form of isotropic silicon etch is HNA. A mixture of hydrouoric acid (HF), nitric acid (HNO3), and acetic acid (CH3COOH), and lead to rounded shape isotropic features in single crystalline silicon. HNA (hydrofluoric, nitric, acetic) is an extremely aggressive acidic mixture which will vigorously attack silicon. It is an isotropic wet etchant which etches silicon at a rate of approximately 1-3 microns per minute.

Anisotropic etchants etch faster in some crystallographic direction than in the others. Potassium hydroxide (KOH) is the most common anisotropic etchant as it is relatively safe to use. Structures formed in the substrate are dependent on the crystal orientation of the substrate or wafer. Mostly such anisotropic etchants progress rapidly in the crystal direction perpendicular to the <110> plane and less rapidly in the direction perpendicular to the <100> plane. The direction perpendicular to the <111> plane etches very slowly [101].

4.1.4 Surface Micromachining [101]:

Surface micromachining involves the addition of material to the substrate in the form of layers of thin films. These layers can either by structural layers or act as spacers, later to be removed, they are known as sacrificial layers. Hence the process usually involves films of two different materials: a structural material out of which the free standing structure is made (generally polycrystalline silicon or polysilicon, silicon nitride and aluminum) and a sacrificial material, deposited wherever either an open area or a free standing mechanical structure is required.

4.1.5 Substrates [100]:

The most common substrate material for micromachining is silicon. The reasons to have silicon are

- Silicon is abundant and inexpensive material

- Other crystalline semiconductors including germanium (Ge) and gallium arsenide (GaAs) are used as substrate materials due to similar inherent features, but silicon is distinguished from other semiconductors in that it can be readily oxidized to form a chemically inert and electrically insulating surface layer of SiO_2 on exposure to steam at high temperatures.

- The homogeneous crystal structure of silicon gives it the electrical properties needed in microelectronic circuits, but in this form silicon also has desirable mechanical properties.

- Silicon forms the same type of crystal structure as diamond, and although the interatomic bonds are much weaker, it is harder than most metals. In addition, it is surprisingly resistant to mechanical stress, having a higher elastic limit than steel in both tension and compression. Single crystal silicon also remains strong under repeated cycles of tension and compression.

- The crystalline orientation of silicon is important in the fabrication of MEMS devices because some of the etchants used attack the crystal at different rates in different directions.

- Silicon is dominant as a substrate for MEMS but research and development is ongoing with other non-semiconductor substrate materials including metals, glasses, quartz, crystalline insulators, ceramics and polymers [102].

4.2 Design of TCC with Silicon nitride (SiN)

We used L-Edit software tool in this project, to draw the design of MEMS TCC device. These designs are used to prepare the photolithographic mask. The process of photolithography is explained in detail in the previous sections. Cantilevers and overhangs have been designed using this software tool and can be observed in figure 4.1. The fabrication process is explained in the next section.

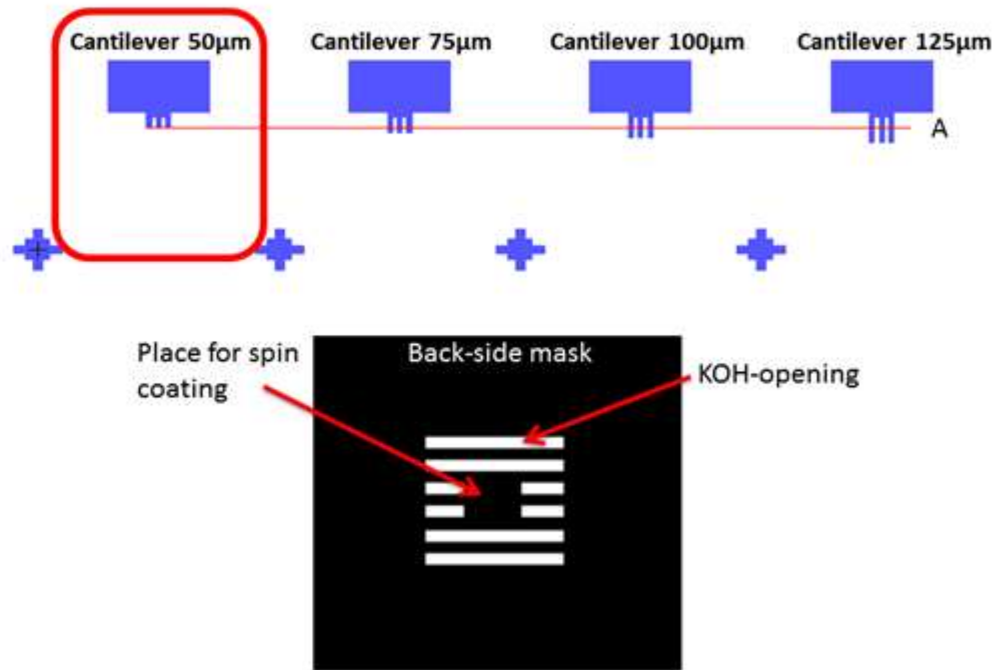

Figure 4.1: The cantilevers are mechanically coupled with an overhang. The lengths of the cantilevers are varying for each step as written on top of the designs. As the lengths of the cantilevers are increasing the resonance frequency is decreasing. The back-side mask is used for KOH opening widows. The black square is used for spin coating of PR. The spin coater needs to hold the sample by vacuum, this can destroy the membranes, and therefore the black square can prevent the breaking of the membranes during the rotation of spin coater.

4.3 Fabrication process flow of SiN

We fabricated cantilevers (details in appendix C) starting from a bulk silicon wafers with a 2 micron-thick low-stress silicon nitride on both sides grown by LPCVD. The cantilevers are thus made of silicon nitride.

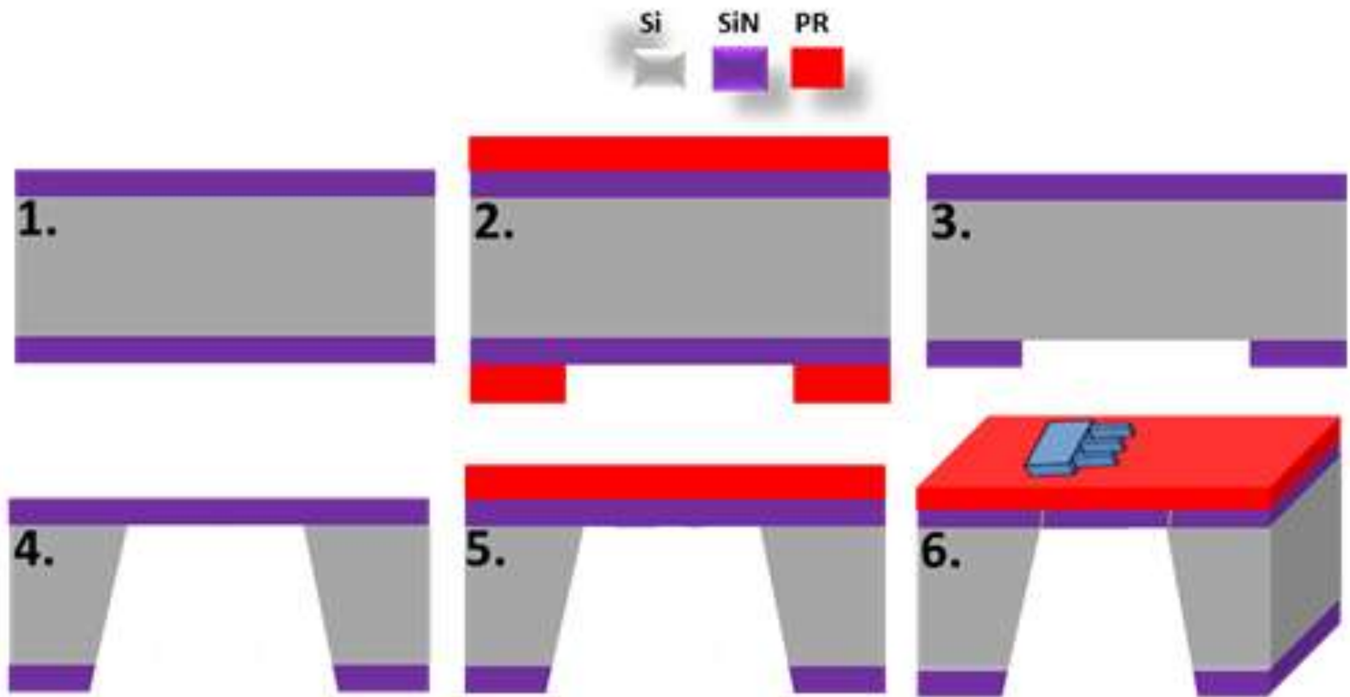

Figure 4.2: Different steps of the fabrication process of TCC devices in silicon nitride are sketched.

1st step: The Si wafer is a commercial product available in the market. The thickness of the silicon is 500µm. We used a wafer with 2 microns silicon nitride on both sides. The wafer is cut in small pieces at $2x2cm^2$ so as to fit in vacuum chamber.

2nd step: The fabrication process is done from the bottom of the sample. The photoresist is deposited on the sample and photolithographic process is done with the back-side mask design as shown in figure 4.1. The areas of PR which is not exposed to UV light will not be developed. The areas of the PR which is exposed to UV light are removed.

3rd step: In this step, we etched silicon nitride using Reactive Ion Etching (RIE). The sample after photolithography process is place in RIE chamber. The sample and the chamber acts as a two parallel plate capacitor. Different materials have different etch rates. Two different gases CF_4 and O_2 with proper composition have been introduced in the chamber. 28.5 sccm of CF_4 and 1.5 sccm of O_2 are selected from the panel of RIE. An RF signal of 250V and 100W of power is also applied. The gases inside the chamber are ionized and react with the surface of the sample. 2 microns of silicon nitride has been etched in 30 minutes of process time. There are two ways to find out that the etching is finished. The first way is to see any changes in color from violet to green and silicon will remain as a combination of white and grey when we tilt the sample. During the titling of the sample the color of the silicon nitride changes and silicon will not change at all.

The second way which is the safest way is to measure the height of the sample with a profilometer. A profile meter is a tool that measures the height of the sample. If the etching went successful the height of the silicon nitride and the silicon should be $\Delta h = 2$ µm as illustrated in figure 4.3.

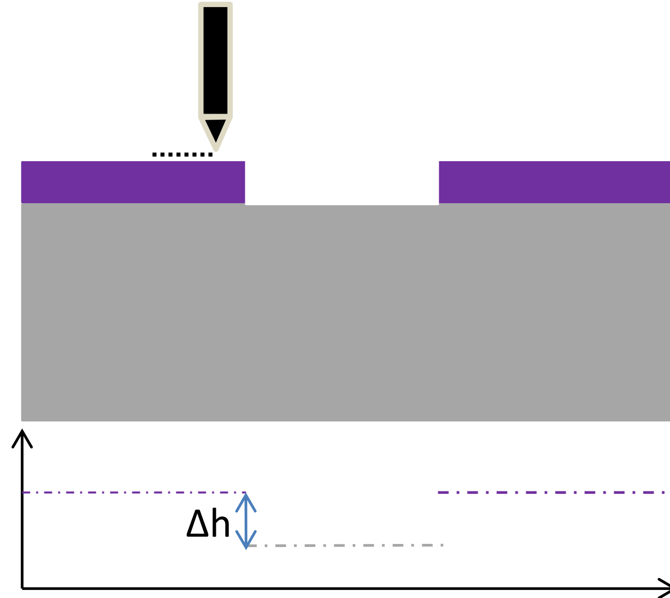

Figure 4.3: The first layer is the silicon nitride and the second is the silicon. With a cantilever plus a tip the level of silicon nitride and silicon is measured. The profiles of the heights of the two materials are sketched. The profile meter is used to measure the height of different materials.

The unetched part of silicon nitride is used as a protection mask for silicon substrate in the next step of fabrication process.

4th step: We etching through the silicon substrate by using KOH solution. The sample is immersed in solution of KOH having a concentration of 7.5M with a temperature of 70^{0}C kept approximately 7-8 hours time. The etch is observed along the crystal plane <111> can be seen in the above figure 4.2. The etch shape is a pyramid, and the angle is 54.7^{0} [100].

5th and 6th steps: In these steps, we performed the fabrication processes on top of the sample. The PR layer is deposited on the top of the silicon nitride membrane. This is the critical and crucial step of fabrication of the TCC devices, as shown in step 6 of figure 4.2. The figure 4.4 shows that the TCC device has to be aligned with the edge of the suspended silicon nitride membrane. Due to this step the overhang of TCC has been angled as shown in figure 4.4.

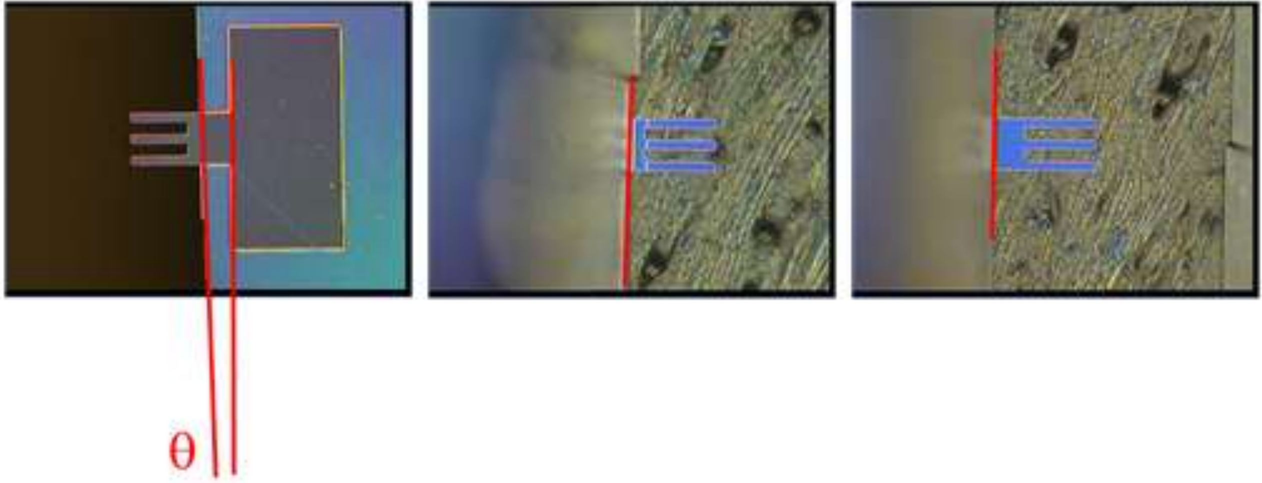

Figure 4.4: It is an optical image of TCC devices. The alignment of the overhang with the crystallographic planes of silicon wafer (edge of the membrane) play a major role in the device measurement. All the three optical images the alignment is not perfectly aligned with the membrane.

The red lines highlight the alignment as shown in figure 4.4. The result of misalignment of few microns may affect the symmetry of the system and thus the mechanical behavior of TCC device.

To conclude, we fabricated TCC device with the standard fabrication methods. However, one of the major disadvantage of the device is the overhang of TCC has to be aligned with respect to the edge of the membrane. It is hardly possible to align in a perfect manner in order to not affect the mechanical properties of the TCC device. Hence, a new approach in design and fabrication of TCC device has been proposed and implemented to overcome the alignment problems in order to achieve better performance characteristics of TCC device.

The modified design and fabrication process is explained in the next section.

4.4 Fabrication Process of TCC device:

In this section, we introduced a new design and fabrication process to overcome the difficulties of earlier design.

As we mentioned earlier, L-edit is the software tool that has been used in this project, to draw the design of MEMS TCC device. These designs have been used to prepare the photolithographic mask. The process of photolithography is explained in detail in the previous sections. Cantilevers, overhangs, electrodes for RF have been designed using this software tool and can be observed in figure 4.5.

The overhang of the designs in figure 4.5a, b and c are of same dimension and the lengths of the cantilevers are 50µm, 100µm and 125µm, respectively.

The process if etching undercut allows a better alignment. The electrodes are designed on the same mask and therefore are intrinsically aligned.

4.5 Second design with silicon nitride (SiN)

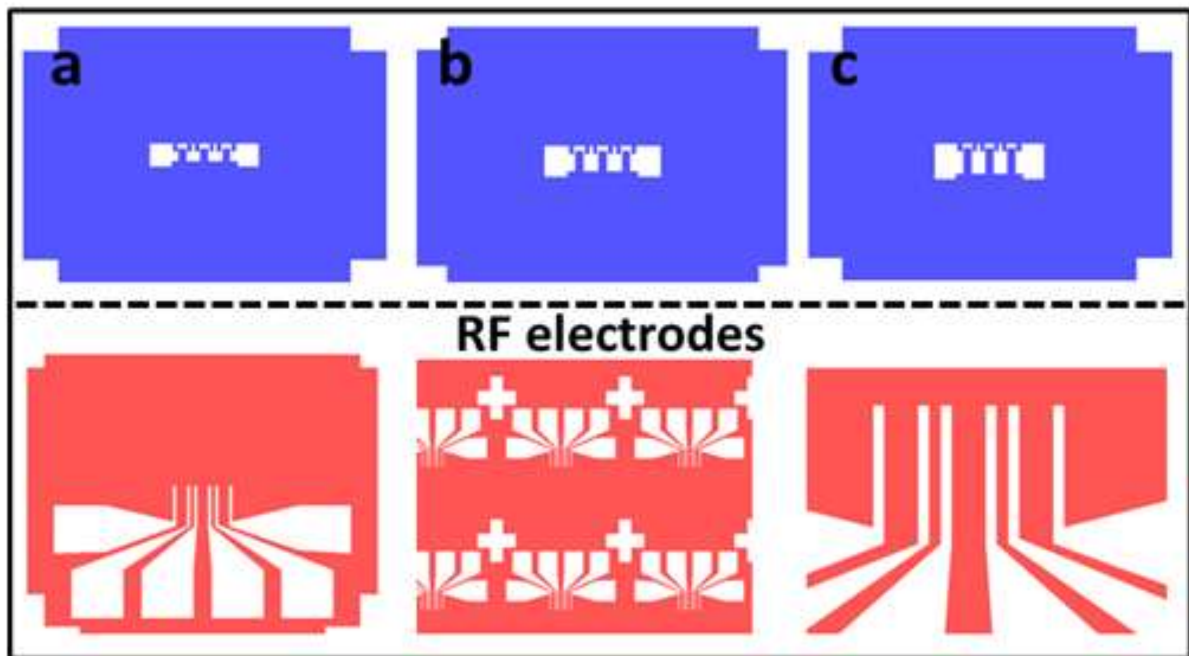

Figure 4.5: These designs are made with silicon nitride. The overhang of the designs in a), b) and c) are having the same widths and lengths and the length of the cantilevers are 50µm, 100µm and 125µm, respectively. The main point of fabricating electrodes is to align with the cantilevers. The electrodes are etched during the etching process. However, each cantilever will have two set of electrodes. The purpose of having two electrodes for one cantilever is to control the vibration amplitude of each cantilever. The red colors are the electrodes for applying RF signal to polarize cantilever.

As shown in the figure 4.5a, b and c, the advantage is the position of the electrodes is already aligned during the KOH etching process. Each cantilever is having two electrodes on either side as showing in figure 4.6a.

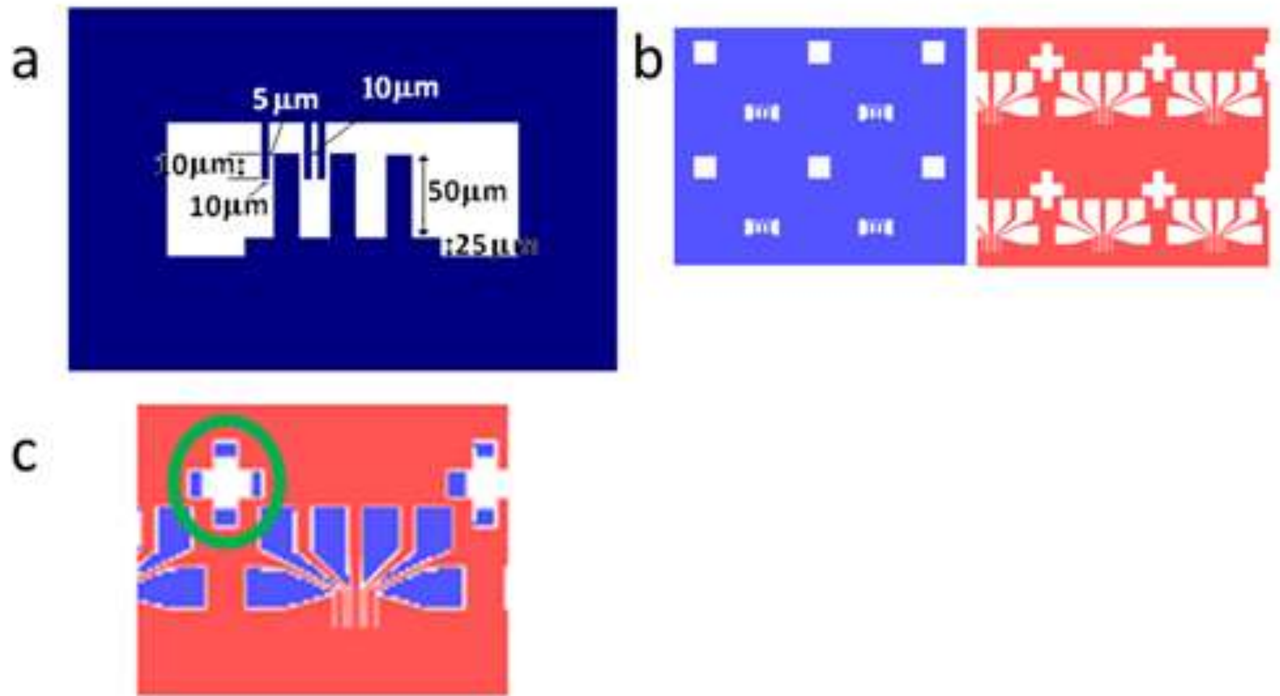

Figure 4.6: The dimensions of the electrodes and cantilevers of TCC in silicon nitride. a) The cantilever is 50µm in length, 75µm and 100 µm, respectively. The height of the overhang is constant in all the three designs. b) This process needs two alignment marks. The first alignment is the square that is coming with making the TCC. c) The alignment is to align the white cross with the square, as shown with the green circle when all the sides are equally spaced, then the electrodes are aligned very well with the TCC cantilevers.

4.6 Fabrication Process Flow of TCC device

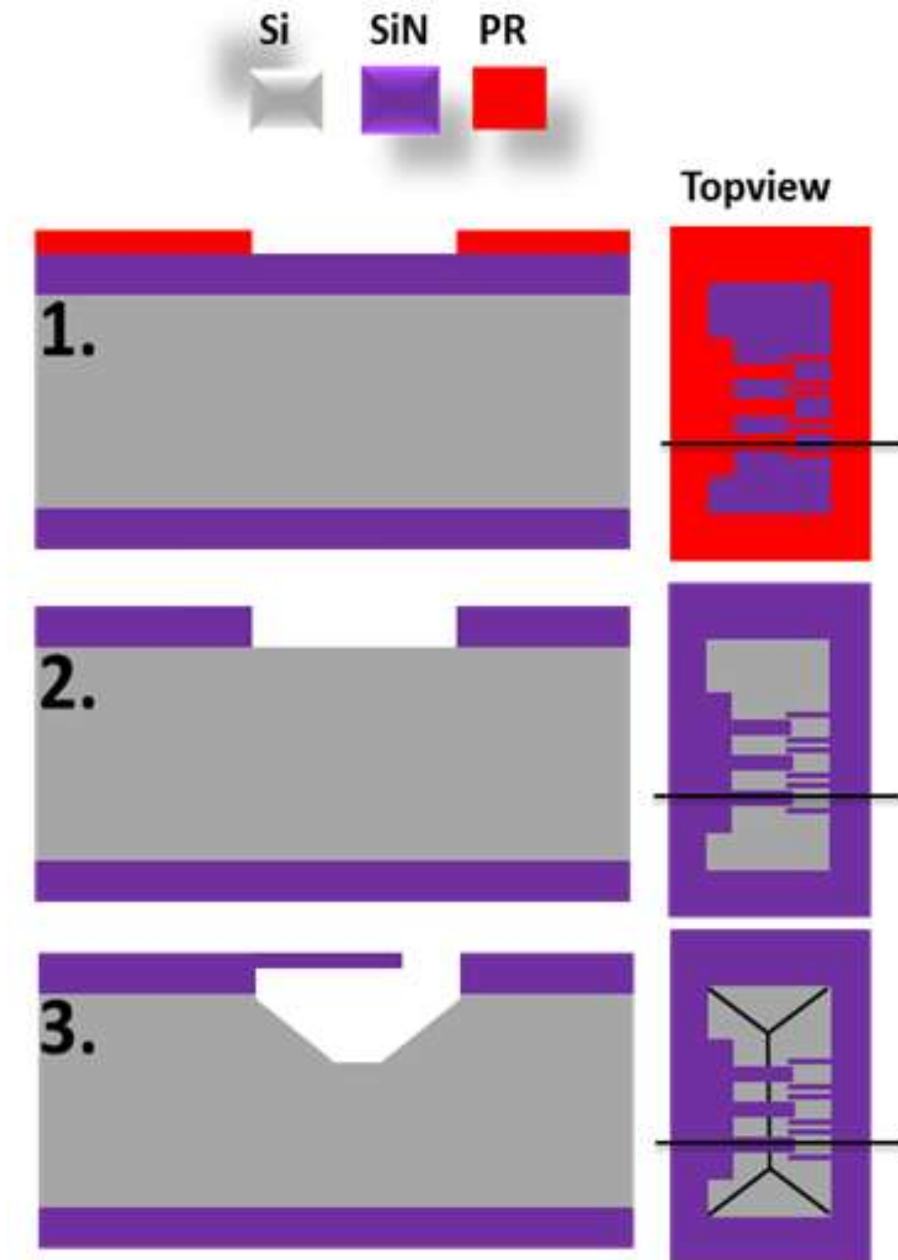

Figure 4.7: The second approach of TCC fabricated in silicon nitride. The main steps are taken in this flow. The whole processes are performed on the top of the TCC sample. The top views are to show the top of the surface of the sample. The black lines illustrating the place the three steps are sketched.

1st step: In the first step, we transfer the designs of patterns, onto the surface of a substrate using photolithographic process. Initially, the sample is coated with PR using spinner. A mask as shown in figure 4.7 has been used for photolithographic process. The purpose of PR layer is to protect the some part of the silicon nitride against RIE etching. The most critical action in this step and in general for this process is a careful alignment along the <111> crystallographic direction. Indeed wafer have always a “flat” indicating the crystallographic direction. Since both mask edges and wafer flats are macroscopic, alignment is rather easy

and can be made with a significative precision.

2nd step: In the second step, we etched the silicon nitride using Reactive Ion Etching (RIE). The sample is place in RIE chamber after photolithographic process. The sample and the chamber acts as a two parallel plate capacitor. Different materials have different etch rates. Two different gases CF_4 and O_2 with proper composition is given in the chamber. 28.5sccm of CF_4 and 1.5sccm of O_2 are selected from the panel of RIE. An RF signal of 250V and 100W of power is also applied. The gases inside the chamber are ionized and reacted with the surface of the sample. It has been observed that 2 microns of silicon nitride has been etched in 30 minutes of process time.

3rd step: In the third step, we etch the silicon substrate by using KOH wet etch process. The sample is immersed in solution of KOH having a concentration of 7.5M with a temperature of 70^0C kept approximately 4 hours time. The etch is observed along the crystal plane <111>. It is to be observed that the overhang, cantilevers and electrodes are etched out at the same time. The positions of the electrodes are self-aligned as discussed earlier.

After that we fabricated the electrodes. After the process of KOH etch, the sample is spin coated using spinner with the two different materials. The first one is the Lift-Off Resist (LOR 3B) and the second one is the PR (S1828). The LOR is used to make lift-off Au. The corresponding mask is shown in figure 4.5 RF electrodes. More attention has been taken to align the RF electrodes with the sample.

Finally, we deposited Gold (Au) on the top of the sample (or electrodes). Evaporation is a common method of thin film deposition. The gold material is evaporated in a vacuum. The vacuum allows vapor particles to travel directly to the sample, where they condense back to a solid state. The final step is to make Lift-Off in a developer solution for 4-5 hours depending on the thickness of the LOR thickness and baking time, 2μm and 180^0C, respectively. The etching along <111> crystal plane gives the cantilevers and location of the electrodes as shown in figure 4.8.

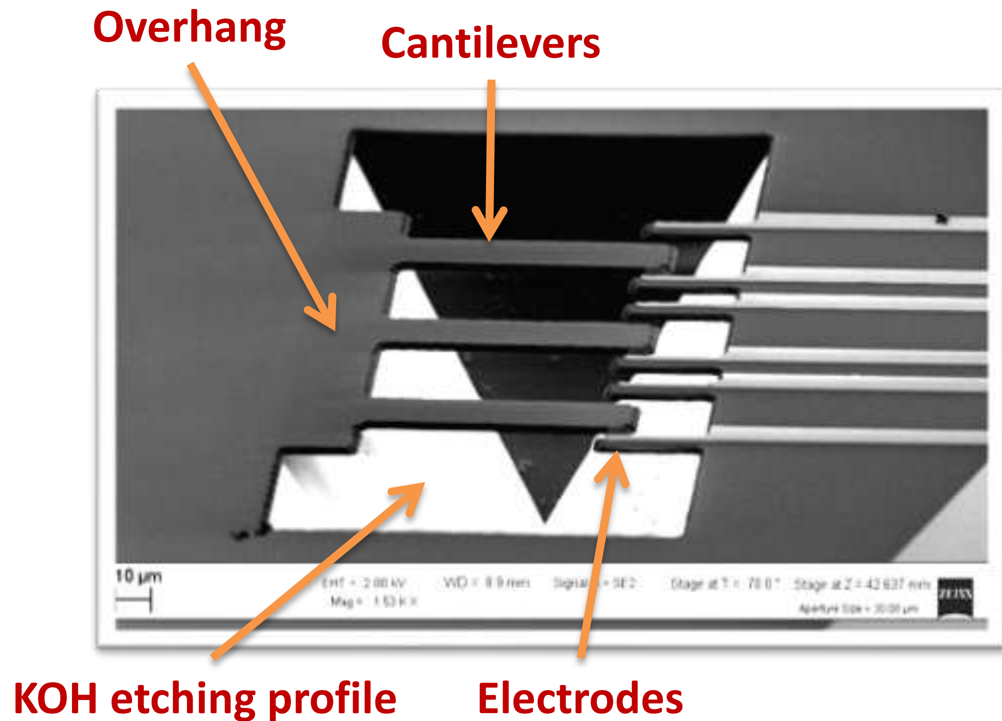

Figure 4.8: The final step of the fabrication process of TCC SiN device. The overhang, three cantilevers and the place of the electrodes are very well aligned. The E-beam evaporation of Au layers is deposited and the Lift-off is also done. The etching profile of KOH is clearly shown that the etching is along the <111> crystal plan.

The alignment of the RF-electrodes with the TCC mask as illustrated in figure 4.6c is done as shown in figure 4.9.

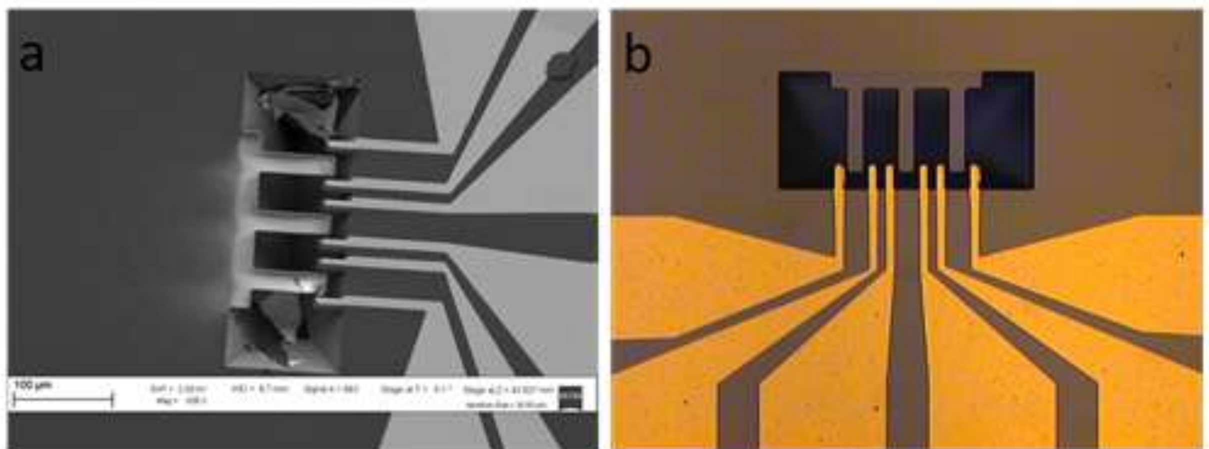

Figure 4.9: The final prototype of TCC with the electrodes. a) The SEM image is taken from the top of the sample. The RF-electrodes are aligned with the cantilevers. The two corners of the KOH-etched hole are metal pieces. This is due to the Lift-off process. b) The optical image is showing a TCC device which the RF-electrodes are very well aligned with the cantilevers.

In conclusion, we introduced and fabricated a new design of MEMS TCC with SiN material using standard fabrication techniques. A perfect alignment between the cantilevers, overhang

and the electrodes has been achieved and is in good agreement with layout as shown in the figure 4.9. This device has overcome all the difficulties such as alignment between the overhang of TCC and membrane as shown in the figure 4.9.

We also attempt to fabricate the same design of TCC with Silicon On Insulator (SOI) material to estimate the mechanical properties and the performance characteristics of the device. The design and fabrication process of SOI TCC are explained in the next section and results are quoted in the forthcoming sections.

4.7 Fabrication with Silicon on Insulator (SOI):

The same designs as shown in the figure 4.1 for overhang 25µm has been used in this section and fabricated accordingly.

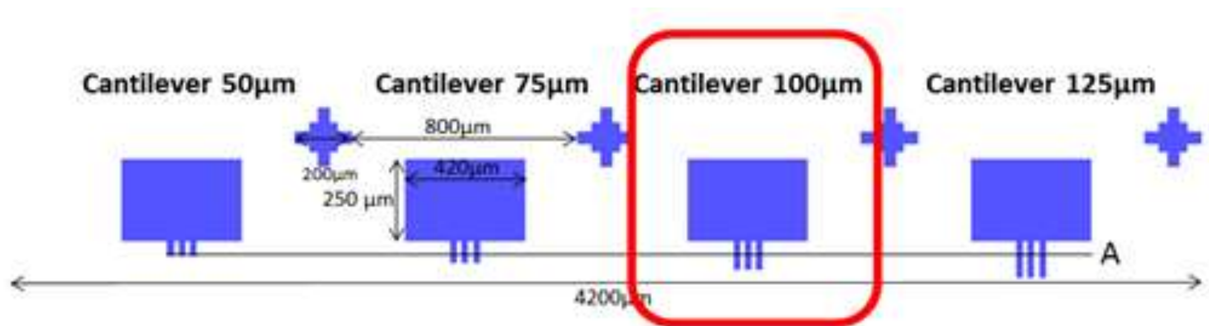

Figure 4.10: These designs of TCC are fabricated in SOI. The lengths of the cantilever start with 50µm increases by 25µm as the line A is indicating. The separation of the cantilevers is 20µm between each other. The length of 100µm is fabricated as framed with a red line.

4.8 Fabrication process of SOI

As discussed, fabrication of TCC cantilevers consists of variety of different processes. In the proposed case, TCC devices are fabricated from a commercial wafer of $Si/SiO_2/Si$ substrate (SOI). The silicon oxide (SiO_2) is etched to release the cantilevers in the final step, as shown in figure 4.11.

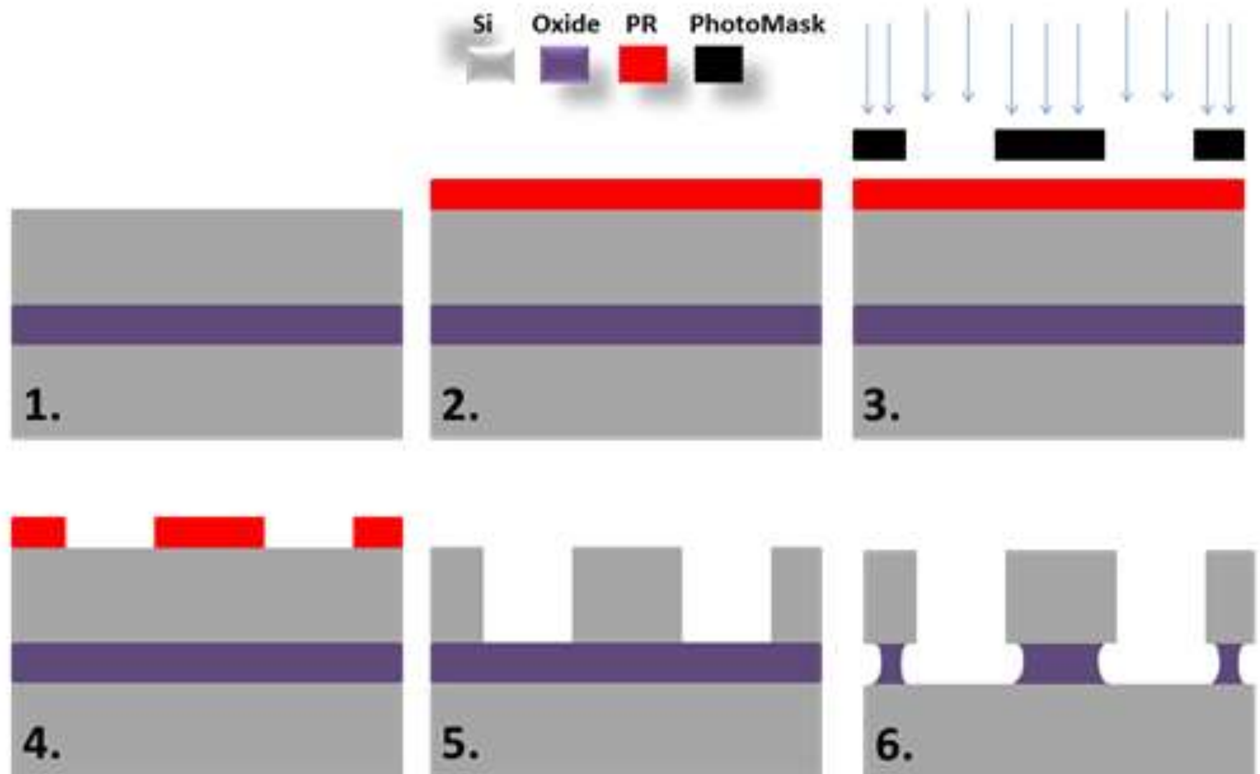

Figure 4.11: Fabrication process of SOI TCC device. There are three small squares that are defining the color labels in the different process steps.

1st step: The SOI wafer is commercially available in the market and is used in this process.

2nd and 3th steps: We deposit 2 microns of PR on top of Si substrate using spinner. After covering the sample with PR, defined the structures of TCC designs by using optical lithography process. As illustrated in the previous sections, a photolithographic mask (black squares), as illustrated in step 3 in figure 4.11, is used in an optical lithography process. The designs of the mask of the cantilevers are illustrated in figure 4.10.

4th step: The PR is developed in developer solution.

5th step: In this step, silicon is etched using Reactive Ion Etching (RIE). The sample after photolithography process is place in RIE chamber. Two different gases CF_4 and O_2 with proper composition have been given in the chamber. 28.5sccm of CF_4 and 1.5 sccm of O_2 have been selected from the panel of RIE. An RF signal of 210V and 100W of power is also applied. The gases inside the chamber are ionized and reacted with the surface of the sample. It has been etched in 30 minutes of process time.

The last step or 6th step: This process releases the cantilevers from the substrate. The releasing process is done by using a HF-based buffered oxide etchant (BOE), as shown in step 6 in figure 4.11. BOE removes 100nm per min and the sample was in the solution for two hours to remove more than 4 microns of SiO_2 from the bottom of the cantilever. The cantilevers are suspended to an overhang or to a base. The image in step 6 in figure 4.11 is showing that the etching process profile of the overhang and base. The silicon oxide under the cantilevers is also etched since the etching of silicon oxide is isotropic. At this point if the sample is dried in room atmosphere, there is a problem with sticking. The cantilevers stick to the Si base because the formation of small droplets of water between cantilevers and substrates which pull down the cantilever due to water surface tension. In order to protect our cantilevers from sticking problem we use a super critical phase drying. In this way it can be protected cantilevers from drying. The space of the cantilevers and the substrate is less than 2 microns, as shown in figure 4.12.

Figure 4.12: These cantilevers are made in silicon. The red circles are illustrating the sticking area in the cantilevers. The sticking happens only at the free ends of the cantilevers. a) and b) All the cantilevers are suspended to a base. The cantilevers are sticking to the silicon oxide. c) The cantilevers are suspended to an overhang. The sticking of the cantilevers is due to the distance between the cantilevers and the substrate. After rinsing the cantilevers in the water, the sticking appears.

We observe the stick area at the free end of the cantilevers as shown in red circles of figure 4.12. This is due to the oxide etching. This may destroy the measurement because; the cantilevers will not be able to vibrate.

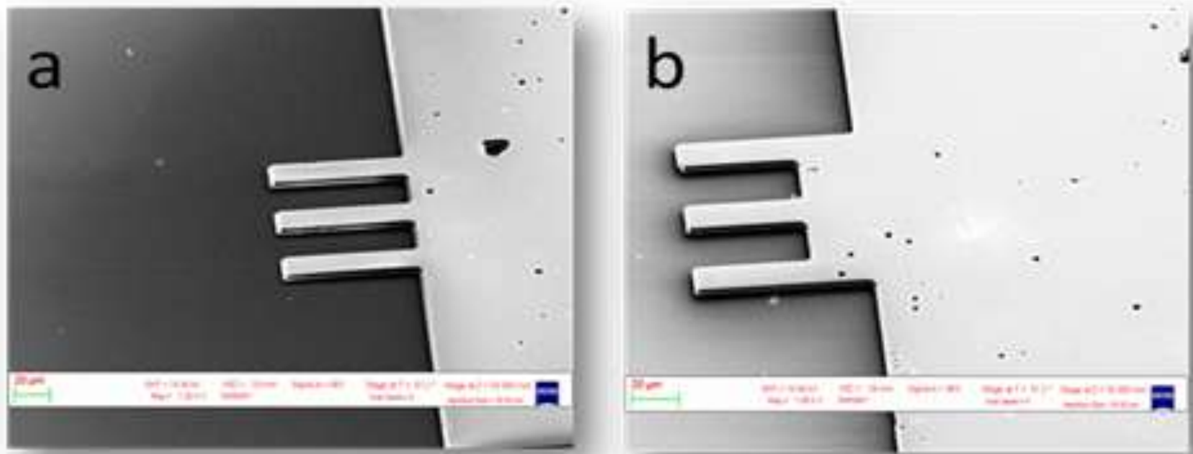

Figure 4.13: The cantilevers that are fabricated in silicon. a) The cantilevers are suspended to a base. b) The cantilevers are suspended to an overhang.

The undercut in SOI samples are intrinsically self-aligned, but as seen in figure 4.14 the coupling overhang is not well engineered. The etching profile is a crucial step because it can change the width and length of the overhang and thereby changing the dimensions of the cantilevers, as is shown in figure 4.14b.

Figure 4.14: a) Before etching silicon oxide layer in HF. b) After HF etching of silicon oxide layer. The dimensions of the cantilevers are changed. The etching profile does not have a symmetric shape under the TCC structure. This can change the mechanical property of the TCC sample.

Finally after super critical phase drying, the sticktion issue is overcome and TCC device is realized. Figure 4.13 shows the SEM images of the TCC devices that are fabricated.

However, we observe numerous defects and disadvantages with this SOI device. The etching profiles of silicon oxide shows that the overhang and the cantilevers are not properly etched and not following the symmetry. This may lead to vary the mechanical properties of the device means the central cantilever may not operate as desired.

5 EXPERIMENTAL RESULTS

5.1 Introduction

In this chapter, frequency response measurements are described. As discussed in the previous chapters, we fabricated three different designs with different fabrication processes. The three designs are

TCC with SOI (*SOI TCC*) shown in figure 5.5c
TCC without electrodes (*SiN TCC*) shown in figure 5.7 , 5.8d and 5.9d
TCC with electrodes (*SiN Electrodes TCC*) shown in figure 5.12

The merits and demerit of each design have been discussed in the previous chapters.

We performed frequency and phase analysis with respect to the oscillation amplitudes on all three cantilevers of all the above said three designs, initially on *SOI TCC* later with *SiN TCC* and finally on *SiN Electrodes TCC.* The three kind of TCC devices are actuated with different actuation strategies. Namely 1. Piezoelectric, which is most convenient, easy to operate [103] 2. Optical which is the most accurate in systems with many different resonances [81,104] and 3. Dielectric gradient force actuation (also called RF actuation), which the newly introduced strategy and can easily integrable with electronics, [82] *SOI TCC* is actuated with both piezoelectric and optical actuation method; *SiN TCC* is actuated with optical actuation; *SiN Electrodes TCC* is actuated with both laser and dielectric gradient force actuation. An attempt is made to investigate the most suitable actuation strategy for the TCC, the results are presented in this chapter. Also, we investigated to make use the *SiN TCC* as a mass sensor and a new approach is introduced to measure the mass as mode localization. *SiN TCC* is used in this project to measure the mass of *silica beads.* The diameters of beads are 1 and 4 microns.

However, the deposition of the beads are not in easy to control therefore it was impossible to locate the beads only at the very end of the cantilevers. On the contrary many beads were observed at the overhang of the TCC device or along the length of the cantilevers as seen in figure 5.7, figure 5.8d and 5.9d. This issue has overcome by using Focused Ion Beam (FIB) technique which can be used to precisely position or remove a given mass with nanometric resolution at the cost, however, of time consuming and very expensive process.

We also performed experiments to use the *SiN Electrode TCC* as Micromechanical Transistor (µMT). We were motivated by an interesting article from the Roukes group in which an interest in the article [105] RF MEMS devices for digital and analog applications were proposed. We applied dielectric actuation strategy to the TCC in order to make use the *SiN Electrode TCC* as mechanical transistor. By the simultaneous application of static voltage (DC Voltage) and RF signal to the central cantilever and static voltage (DC Voltage) to the one of the lateral cantilevers, results other lateral cantilever to vibrate. The vibration amplitude can be controlled by the DC voltage. The behavior of this TCC device resembles the function of a Field Effect Transistor (FET), where the gate voltage controls the current flow in the channel. More explanation is given in the forthcoming sections. Experiments have been performed on *SiN Electrode TCC* and the results are presented in this thesis.

Finally, an attempt to measure the mass of a cell and correlate it to bio-relevant informations, such as genetic alterations is made on a single cantilever having paddle area of 200x200 μm^2. The resonance of the cantilever frequency was around 100-130 kHz and cells were grown directly on the paddle. The idea was to measure the resonance frequency before and after the growth of cell, in order to find out the quantitative weight of the fixe cells per cantilever. The results are presented in this chapter.

5.2 Experimental setup

We measured the frequency response of TCC devices (*SiN TCC*, *SiN Electrodes TCC* and *SOI TCC*) using a custom built experimental setup, as shown in figure 5.1. With this setup three different actuation strategies can be implemented, such as piezoelectric, optical and dielectric gradient force (RF), as explained in the introduction chapter. The setup consists of three main sections. The first section is the actuation, the second section is the detection and the third section is the readout electronics. The *SOI TCC* and *SiN TCC* devices utilize the two different actuation schemes presented in experimental results chapter, on the other hand, *SiN*

Electrodes TCC utilize the dielectric gradient force actuation scheme, because this actuation scheme needs integrated electrodes. For the detection of the vibration amplitudes of the cantilevers a detection system made with a light source (CW green laser), a photodetector (4QP), beam splitters, focusing lens was assembled. The readout system was based on a function generator, a Lock-in amplifier and a computer system for data acquisition with a *Labview*-based acquisition software, as sketched in a diagram in figure 5.1.

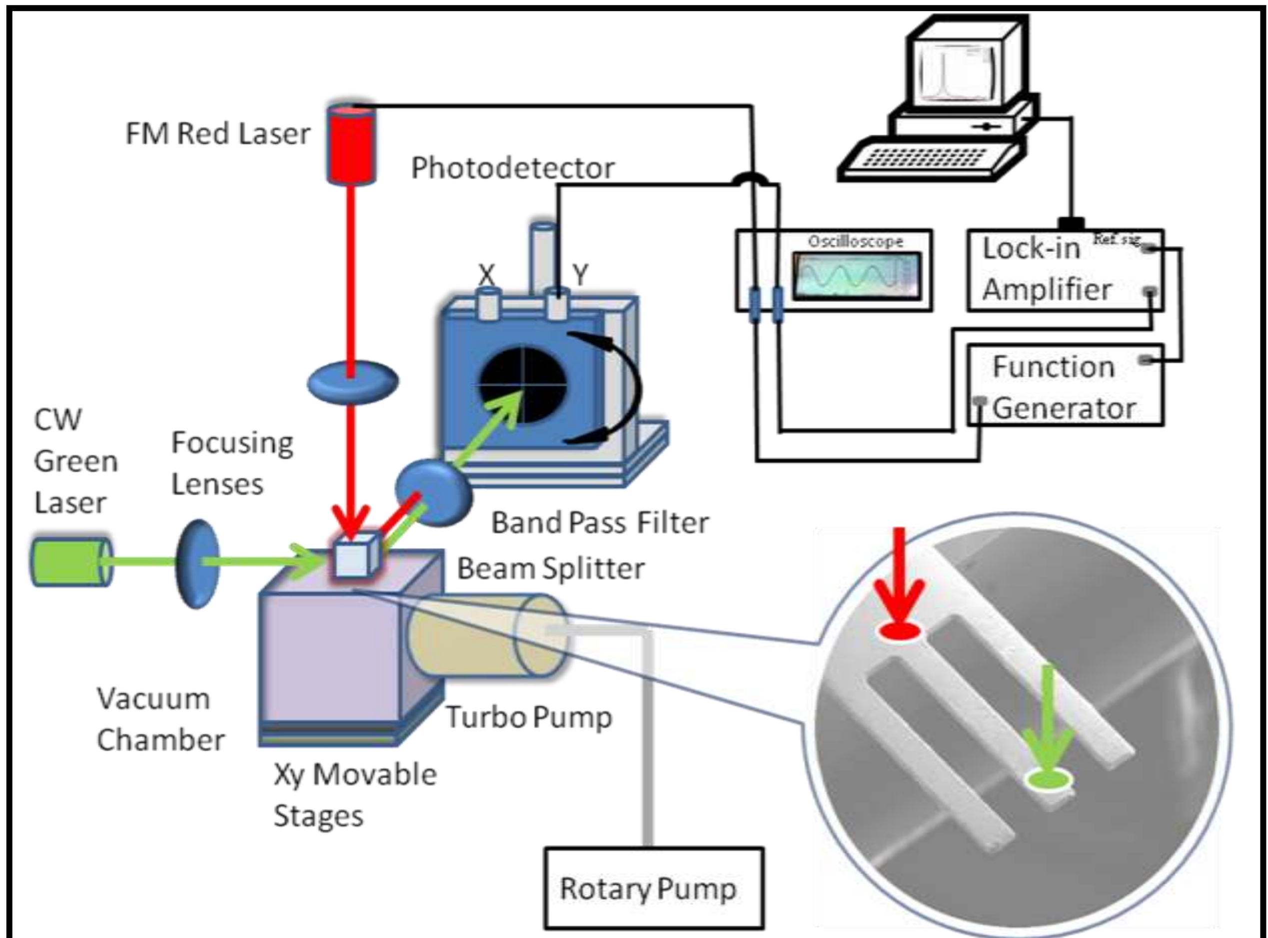

Figure 5.1: This is a diagram of the experimental setup. The main sections are the actuation, detection and data accumulation. The detection laser (green) is used to detect the vibration amplitude of every single cantilever. The frequency pulsed laser (red) is to actuate TCC devices. On the inset SEM image is shown the positions of the spots of the red and green lasers. The red laser spot is placed at the overhang. The green laser spot is placed at the free end of the cantilever. The function generator is used to modulate the pulse of the red laser. One reference signal from the function generator is connected to the Lock-in amplifier. The Lock-in amplifier will extract the signal from 4QP and together with the reference signal generate a resonance frequency. The sample is mounted in a vacuum chamber that can be moved in xy directions.

The TCC devices were mounted in a custom designed chamber with a base vacuum of $1x10^{-6}$ mbar. This chamber is designed in a way to be connected to a pump system, the RF-signals connector, and equipped with suitable sample holder. The details of the drawing of the chamber are in appendix D. The sample holder is on top of the chamber, as shown in figure 5.1 inset SEM image; the sample holder is covered by a transparent plastic, because the red

and green lasers have to be aligned, as shown in figure 5.1 inset SEM image.

The oscillations of the cantilevers were excited by a frequency-modulated red laser [106] which is connected to a function generator. The laser actuation excites selectively those resonance frequencies that are matching the naturally resonance frequencies of the TCC, as presented in this chapter, figure 5.4.

The vibration amplitudes of the cantilevers were detected by an optical readout system as shown in figure 5.2a. The system consists of a green laser and a four quadrant photodiode (4QP) arranged in the optical lever configuration. The latter technique has been used to detect cantilever oscillation amplitudes below 1 nm and therefore is particularly suitable to detect small variation in low amplitude oscillators, as in our case [107]. The green laser beam deflects via two beam-splitters (50%/50% cube beam splitter or prism) one focused onto the TCC device using an optical microscope, as shown in figure 5.2b. A manual micropositioning XY stage is used to move the whole chip with respect to the optical path in order to detect the frequency response of each cantilever. The drive laser signal is removed from the optical lever path using a band pass filter with optical density (OD) 6. A second manual micropositioning XYZ stage is used to move the 4QP to maximize the signal and the rotation of 4QP that can contribute to increase the signal as well as shown in figure 5.2c.

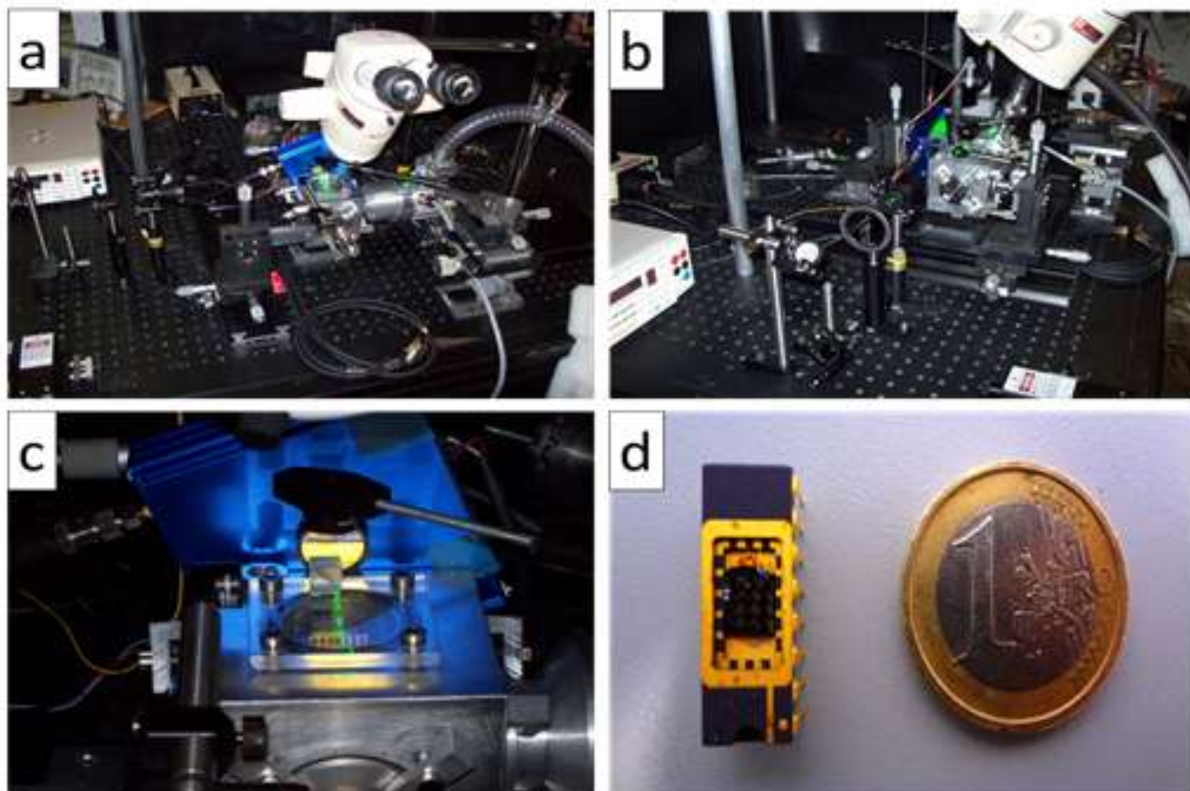

Figure 5.2: Experimental setup images. a) and b) show front and side images of setup of a frequency-pulsed-laser. c) A close view of the photodetector, focus lens, filter and the sample. d) A ceramic dual-in-line package is used to mount the sample with electrical connections to be used for RF dielectric actuation purpose.

5.3 Optimization of Experimental Setup

Moving to SiN cantilever it was possible to obtain more symmetric structures with a very small residual movement of the central cantilever in the second mode. However, it was impossible to obtain zero movement. From FEM simulation, especially in the second mode (antisymmetric mode), a torsional bending was observed with and without added masses on the cantilever in figure 3.10. This is due to the bending of the whole structure which is proportional to the vibration amplitude of the external cantilevers. This torsional mode is present also in the case of a perfectly symmetrical structure. Our interest is to detect the vertical motion of the cantilever and to decouple this information from the always present torsional amplitude. The torsional bending can be reduced by rotating the photodetector. In this way, the torsional bending is decoupled from the vertical vibrations. The frequency response is measured before and after the rotation of the photodetector, in figure 5.3.

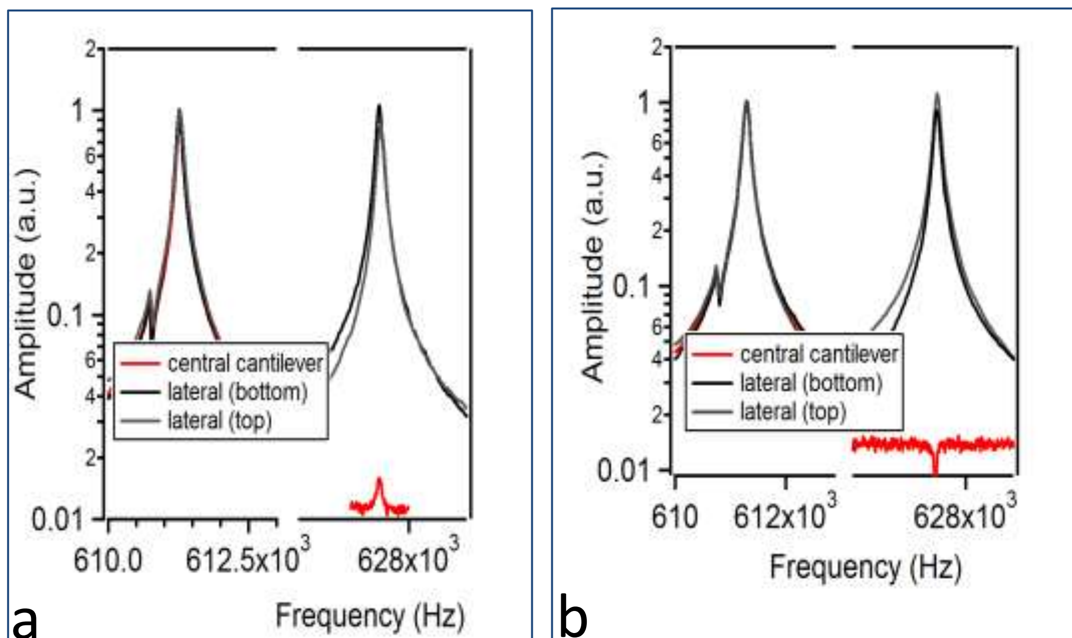

Figure 5.3: The oscillation amplitude versus resonance frequency. The red, black and grey lines are standing for central, upper and down cantilevers, respectively. (a) The angle of the photodetector is not optimized. (b) The angle of the photodetector is optimized.

The above measurements have been performed on the *SiN TCC* device.

5.4 Actuation methods (Piezoelectric and Optical actuation)

In this section, we suggested suitable actuation strategy in order to increase the sensitivity of

the TCC device. Sensitivity of the device can be improved in several ways such as better fabrication process, optimization of the experimental setup and selection of actuation strategy. However, mainly, the actuation method is the key factor in determining the sensitivity. Among several actuation strategies, piezoelectric and optical are the best suitable actuation mechanisms [69]. Frequency response measurements is performed on *SiN TCC* by considering two actuation strategies, the first actuation is to use the piezoelectric material to give a mechanical motion to the sample. The piezoelectric material transforms into the mechanical motion by applying RF signal to the material. The alternative actuation method is the frequency modulated pulsed laser technique to excite the cantilevers of *SiN TCC* device. The respective plots are shown in figure 5.4 below.

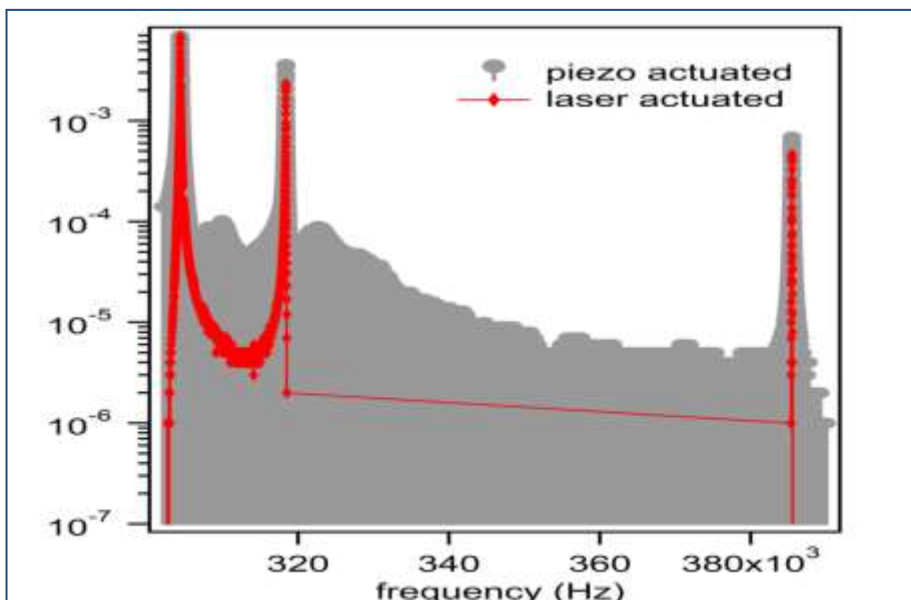

Figure 5.4: The vibration amplitude vs. frequency. The red line stands for optically actuation and the grey line stands for piezoelectric actuation.

The piezoelectric actuation excites the desired resonance frequencies as expected. However, there are some drawbacks for its use. Unwanted spurious frequencies involved in the frequency spectrum is the one the main disadvantage of this actuation as shown in grey color in figure 5.4. A macroscopic piezoelectric slab is placed in mechanical contact with the chip. If we had piezo cantilevers, contacted individually, we will not have the same problems.

The piezoelectric actuation excites preferentially the first fundamental mode more than the second and third. The reason is that in the first mode all the cantilever oscillate in phase and therefore they can be excited all together at the same time by mechanical vibration. In second and third mode, on the contrary, one or more cantilevers are in antiphase with respect to the

other(s): therefore, when the whole chip is excited, part if the energy is transferred to the wrong cantilever, and thus lost. The photothermal actuation on the contrary, can be focused on one particular cantilever so that the maximum energy is transferred for each mode. Moreover, an objective lens is used to focus the position of the excitation laser so that the oscillation intensity can be maximized. As a consequence, as optical actuation excites equally all the modes and the relative intensity respects the amount of energy stored in each mode [108].

The laser beam excites the cantilevers while it focuses by using the objective lens at the overhang of *SiN TCC*. The reason is the modulation of the spring constant is varied by the laser beam by locally heating the spot area (and its temperature gradient), as a result the material will thermally expand, which induces the compressive stress pushing the structure into bending of cantilever [109]. The advantage of applying the optical actuation is it does not require the oscillator to be conducting and no need of additional coils or electrodes located in proximity to the oscillator. It can be easily integrated into existing, widely used optical detection techniques.

5.5 Measurement of SOI TCC

In this design, we fabricated the cantilevers in silicon material. The details of fabrication process are described in design and fabrication process chapter. The fabricated device of TCC of silicon-on-Insulator (SOI) is shown in figure 5.5c.

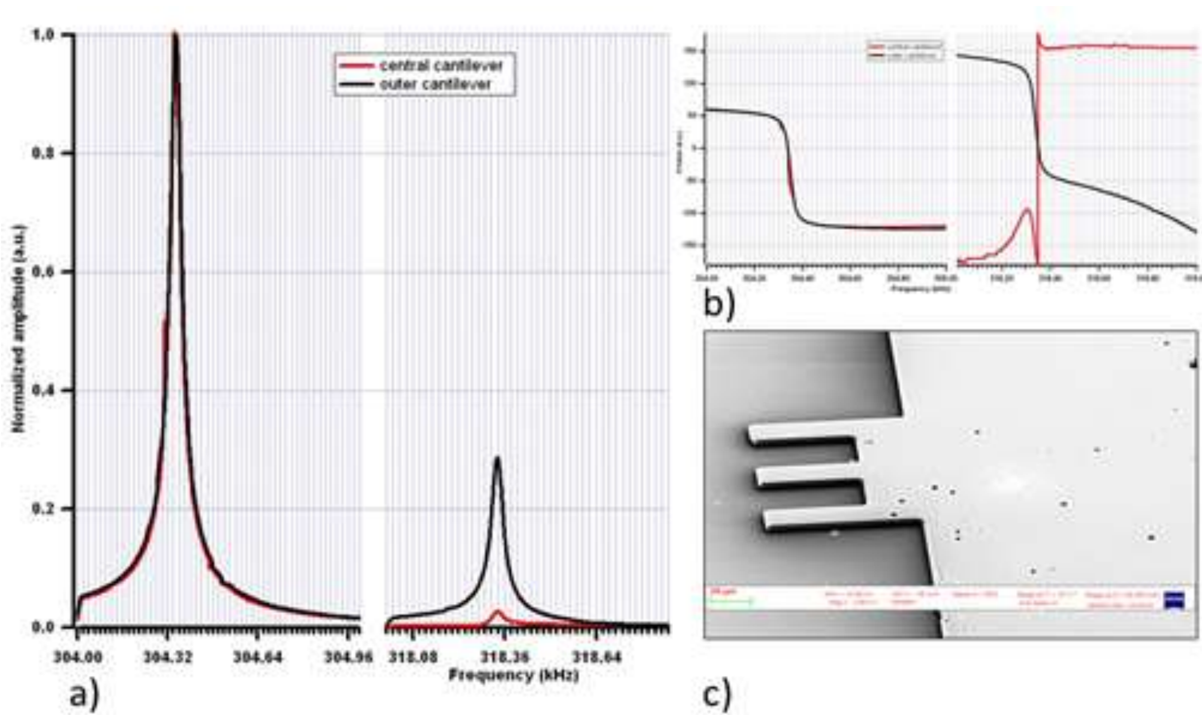

Figure 5.5: The oscillation amplitude versus frequency. a) The measurements are done with the SOI-substrate. Frequency response vs. normalized amplitude of TCC. The red and black colors are indicating the vibration modes of the central and lateral (outer or external) cantilevers, respectively. The central and lateral cantilever is symmetric in the first mode. b) Frequency response vs. phase of first and second modes. c) SEM image of *SOI TCC*.

We measured the resonance frequencies of *SOI TCC*. The measurements are performed on the central and one of outer cantilevers, as illustrated in figure 5.5a. The first and second eigenmodes are 304 kHz and 318 kHz, respectively. The first mode shows that the central and outer cantilevers are symmetric, as there is no frequency shift is observed. The central and outer cantilevers are in same phase as plotted in figure 5.5b. The second mode in figure 5.5a, illustrate the vibration amplitudes of the central and outer cantilevers. The red and black lines are indicating the vibration amplitudes of the central and outer cantilevers, respectively. The vibration amplitudes of the central cantilevers is only a factor 10 less compared to the vibration amplitude of lateral cantilever, and show a finite oscillation amplitude which was not expected from simulations. We attributed this effect to the defects generated in the fabrication process such as improper wet etching as shown in figure 5.5c. It has shown in chapter of *Design and Fabrication Process* that the etching of HF may create asymmetry in the structure in a way that the dimensions of the outer cantilevers are different with the central cantilever. The phase of the central cantilever in the second mode behave as expected, with the two cantilevers which oscillate in phase (neglecting a factor 2π) below the resonance frequency, and oscillate in antiphase above the resonance frequency, which indicated that the

central cantilever oscillate in phase with the non- measured lateral one, which in turn means that the measured one is the heavier of the two is also different as illustrated in figure 5.5b.

5.6 SiN TCC as Mass Sensor

In the previous *SOI TCC* design the vibration amplitudes of the lateral cantilevers have factor 10 higher than the central cantilever. But, there is a necessity to improve this factor to have a better sensitive device. Hence, we proposed and developed another with SiN material *(SiN TCC).* In this *SiN TCC* design, a better fabrication process than *SOI TCC* has been carried out and is presented in the *Design and Fabrication Process Chapter 4.* We observed from the simulation results, addition of more masses to the *SiN TCC* results increase in the vibration amplitude of central cantilever.

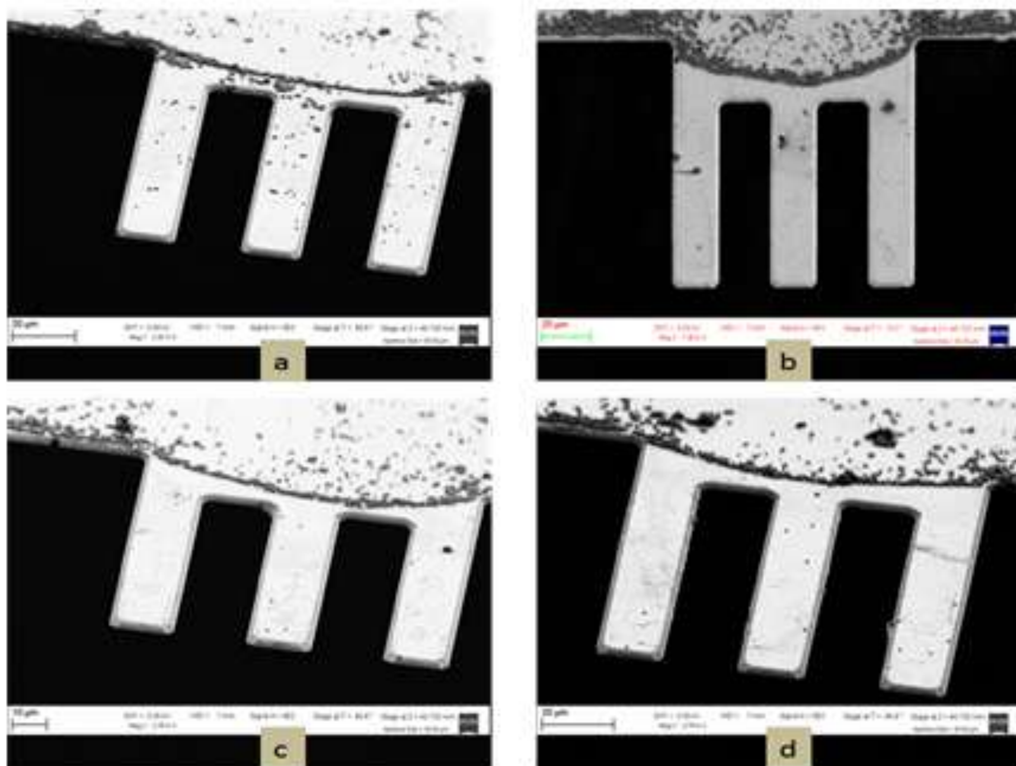

Figure 5.6: Beads on other device with 100 mircons. All the beads are deposited around the overhang, and few beds are on the cantilevers.

In addition, a linear relationship is observed between non-mass lateral cantilever and the central cantilever in the pg range. Investigations have been done to measure the mass of silica beads of sizes 1 micron and 4 microns using the device. Experimental studies are performed to observe the relation between added masses and the vibrational mode localization of *SiN*

TCC with other and better *SiN TCC* devices, as shown in figure 5.8d.

We have measured *SiN TCC* with three beads as shown in figure 5.7a and more beads shown in figure 5.7c.

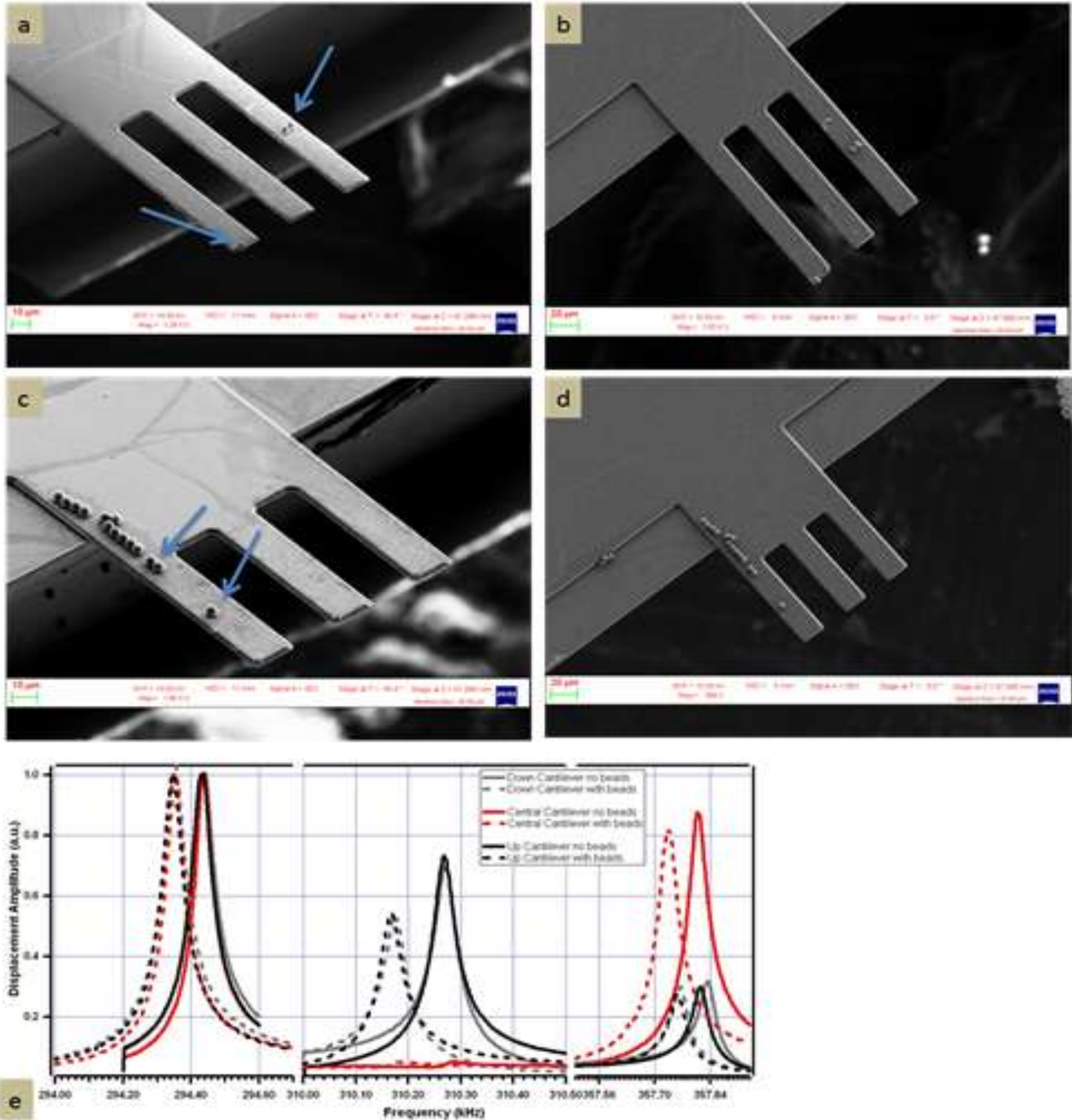

Figure 5.7: a) and b) are the same devices with different view . There are two beads on the right lateral cantilever and one on the left lateral cantilever. Similarly, c) and d) are the same device with different view. e) frequency response of the three modes before and after beads addition for the structure shown in panel a) and b)

The mass response measurement of device figure 5.7a is shown in panel e: Here it is qualitatively clear that the system is still rather symmetric, since the single bead at the edge of the left cantilever is compensated by the two beads in the middle of the right cantilever. The

measurements confirm our assumptions: indeed all the resonance frequencies are lower shifted upon mass addition, as expected, but the amplitude of the second mode for the central cantilever does not change significantly, since the symmetry is quite preserved.

Figure 5.8d. shows clearly the mode localization of *SiN TCC* device.

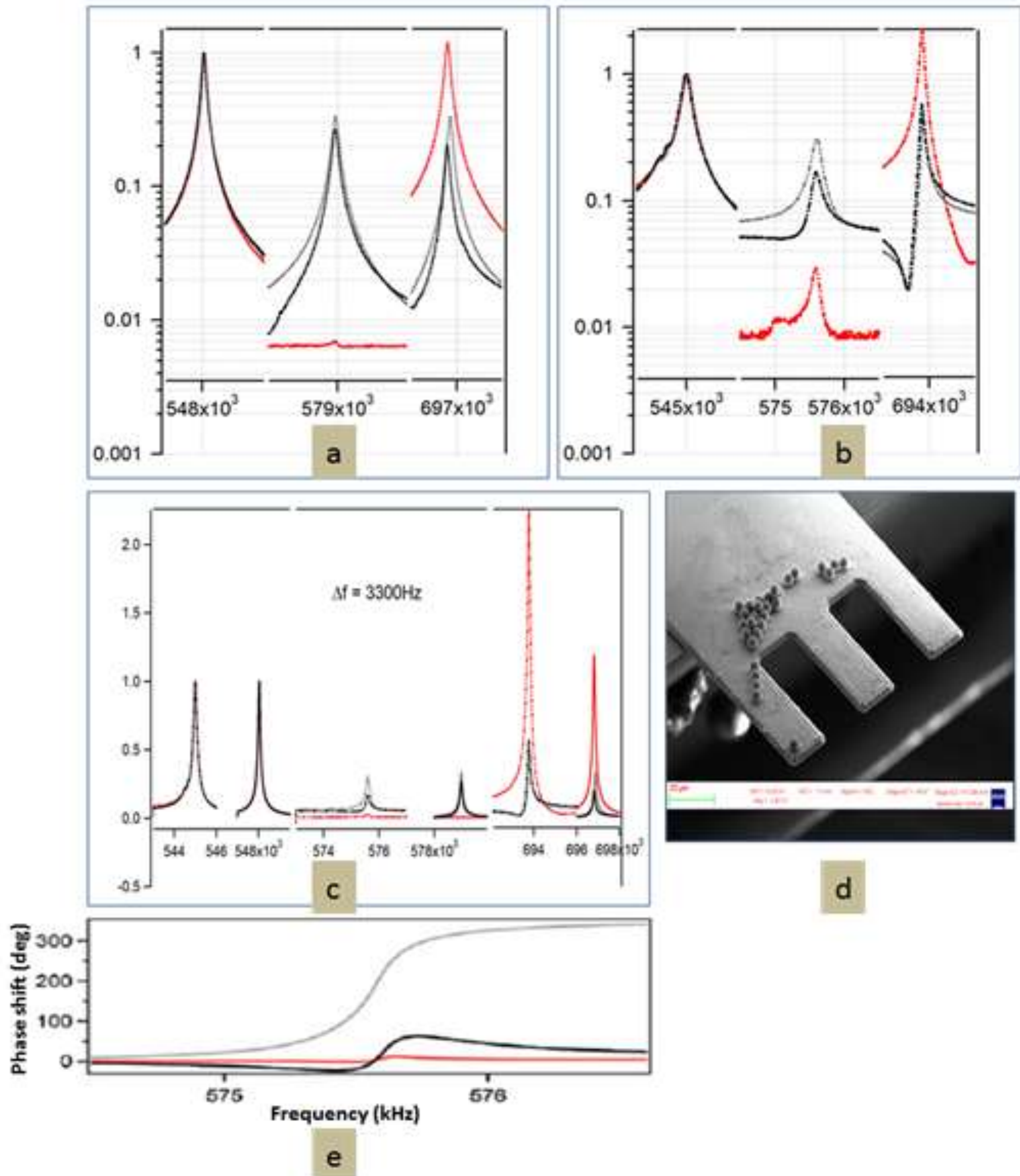

Figure 5.8: Frequency response vs. vibration amplitude. a) This plot is performed before beads are added to the TCC. The black stands for up cantilever, the red stands for the central cantilever and the grey is for down cantilever. The three modes are measured for all the cantilevers. b) This plot is after beads are added. c) In this plot before and after beads are added are plotted together. From the resonance frequency shift the added mass can be calculated. d) A SEM image of TCC with the beads. e) Phase spectrum of the second mode after bead adsorption. The gray curves refer to the lateral cantilever with beads, the black curves refer to the lateral cantilever without beads, the red curves refer to the central cantilever.

In order to test the devices performances, silica microbeads with diameter of 4μm and 0.95 μm and weight of 73 pg and 0.98 pg respectively are used. Silica microbeads were dispersed on the sample starting from a high dilute water-based suspension. Unfortunately this method does not allow a precise location of the beads and only few devices resulted with a suitable bead localization, as shown figure 5.6 for smaller beads and 5.8d. In figure 5.8d we display a scanning electron microscopy (SEM) image showing one microbead at the extreme end of a lateral cantilever, and several beads on the base of the cantilever and on the overhang. Figure 5.8c shows the frequency response of the first mode for the central and lateral cantilever before (right) and after (left) mass addition. The recorded frequency shift corresponds to a mass increase of about 16 pg; considering the 5 beads located along the cantilever, each contributing a fraction (x/L), where x is the distance from the cantilever base and L the cantilever length [110], this gives a bead mass of 9 pg, strongly underestimated. A FEM analysis was performed to test and verify the x/L dependence of the frequency shift also for TCC systems. Figure 5.8a and b shows the oscillation amplitudes relative to the second mode recorded on the unloaded, loaded, and central cantilever (black, gray and red curve, respectively) before and after the deposition of the silica bead. The amplitude ratio ρ_A increases from about 10^{-3} to 0.08 thus providing a mass ratio of 1×10^{-2} that corresponds to an added effective mass of 62 pg. We performed FEM analysis to investigate the dependence of ρ_A on particle location along the lateral cantilever in a TCC system. The simulation showed that ρ_A is proportional to $(x/L)^2$. By weighing accordingly the contribution of each particle we obtained 61 pg per bead, closer to the real value. The frequency shift based mass determination error can be explained considering the stiffening of the cantilever elastic constant induced by the bead interaction at the cantilever bases which shifts the resonance frequency to higher values [111]. From this experiment we conclude that the mass measurement using TCC systems is less affected by surface stress induced by mass location. We also notice, that, in agreement to what should be expected from the general behavior of mode localization [73], the loaded cantilever amplitude is reduced with respect to that of the unloaded one. In figure 5.8e we report the phase behavior for the three cantilevers at the second mode. Before crossing the second resonance the three cantilevers follow the excitation with the same phase delay (180^0). At resonance, the two external cantilevers vibrate in antiphase, and the central one, follows the motion of the unloaded one. Far above the resonance the three cantilevers are again all 180^0 out-of-phases relative to the excitation, but the loaded one has performed one extra cycle. The phase matching between mode resonances for each cantilever is responsible for the asymmetric shape of the resonances [112]. By

monitoring the phase response of the TCC system, the location of the adsorbed mass can be therefore identified, regardless of the value of the added mass.

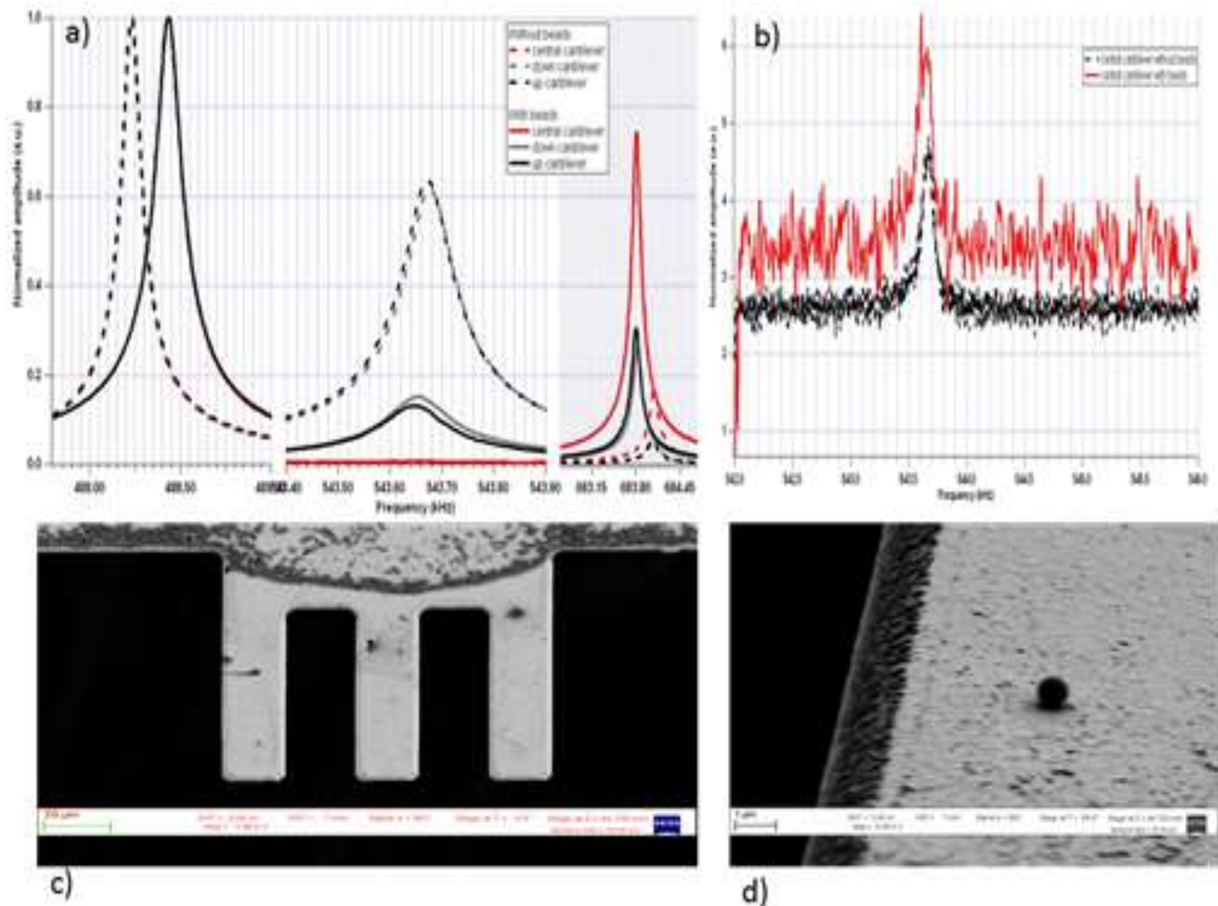

Figure 5.9: Frequency response measurement of another design of *SIN TCC*. This design has twice longer cantilevers than the previous. a) All the three eigenmodes are shown in the same plot. The resonance frequency measurements are performed before and after adding beads. The dotted lines are indicating no beads are added and the continuous lines after beads are added. The black and grey colors are for outer cantilevers and the red color is for central cantilever. b) The mode localization of the vibration of the central cantilever before and after beads is added to the TCC. The black line is indicating the vibration without beads and the red line is showing that the eigenmode is increased (more localized) due to deposition of beads. From the shift in the vibration amplitude modes as illustrated the added mass can be found. c) A SEM image of SIN TCC with deposition of beads on the overhang as well as on the outer-left-cantilever. d) A close SEM image of one bead on one of the outer-left-cantilever.

To further investigate the experimental sensitivity limits of the TCC system and to explore the possibility of minimizing the adsorption induced stiffening effect, in figure 5.9c,d SEM picture shows TCC device in which two small silica bead have been located on one lateral cantilever (the inset shows a detail of the two beads). The frequency response before and after the bead addition is displayed in figure 5.9a,b where first and second mode response are displayed. figure 5.9a shows the 200Hz frequency shift following the mass increase, measured on the first vibration mode of the system. Considering that the particles are located 10

microns away from the cantilever extremity, the measured mass is 1.5 pg. On the other hand, the relative amplitude increase in the second mode measured on the central cantilever and shown in figure 5.9b is 0.0013 thus providing a mass ratio of 1.6×10^{-4} that, considering the quadratic dependence on position along the cantilever, corresponds to an added mass of 1.6 pg. Here, because of the negligible size of the beads, the stress induced upon absorption is negligible and the two methods are consistent with each other.

In conclusion, we demonstrated the application of the measurement of amplitude variation for the determination of the absorbed mass in a TCC system. This approach exhibits sensitivity comparable with the well established frequency shift method, when used in high vacuum and with high quality factor cantilevers, and offers several additional advantages. Our technique is less affected by the surface stress induced by mass adsorption along the cantilever; the quadratic dependence on the adsorbing site position allows a more precise determination of the mass location; using the oscillator phase response it is possible to identify the cantilever onto which adsorption takes place. Further potential advantages are the insensitivity to the adsorption of a nonspecific, uniformly distributed, mass (resulting, for instance, from environmental contamination) that does not alter the symmetry of the system and therefore only induces a frequency shift with no amplitude redistribution, and the weak dependence on the quality factor of the oscillator, therefore on the operation environment of the device.

5.7 Focused Ion Beam with SiN TCC

We used FIB to make some cubic structures on the free end of the cantilever of silicon nitride TCC, as SEM image is shown in figure 5.10. Each cubic structure has an area of $(3\mu m)^2$ and the thickness of the cubic structure is the same of the silicon nitride cantilever (2µm). The dimension of the cubic structure is measured after FIB is performed. Each cubic structure has a weight of 54 pg.

The FIB process is an extremely versatile technique which is used in research environment to remove or deposit material on microstructures with nanometric spatial control. The continuous down scaling of material science demands a corresponding focus on methods for both investigation and manipulation of materials at that level. FIB is a very versatile technique that has found use in different areas within especially semiconductor and materials research. The principle of FIB is not very different from Scanning Electron Microscopy (SEM) and the typical setups look in many ways similar. Ions are extracted from a Liquid Metal Ion Source

(LMIS), which often is gallium that are kept liquid in the source and extracted from a tungsten tip by a large potential, that also ionizes and accelerates the ions to typical energies of 5-100 keV down through the column. Electrostatic lenses condenses and focuses the ions while an extraction voltage and plate apertures pick out a desired beam current by blanking the path of outer ions. Secondary lenses are used to scan the ion beam across the surface. The reason for using electrostatic lenses is because the normally used magnetic lenses in electron microscopes need to be very large to condense the much heavier ions. [113] When ions strike the surface of the sample different scattering processes can occur. Ions are much bigger and heavier than electrons and hence they deliver their much higher energy density at a much shorter distance than electrons. The ions impinge on the surface and interact with substrate atoms in scattering processes. The ion-matter scattering can either have an elastic character with nuclei or inelastic with electron. If the ions deliver enough energy to overcome the binding energy of the surface atoms, these are physically sputtered away and either ventilated out or redeposited in other areas. The sputtering of atom by the ion beam is referred to as FIB milling. If the ions do not transfer the required amount of energy to sputter away atoms, they instead enter the sample. Thus contaminating the original material [114,115].

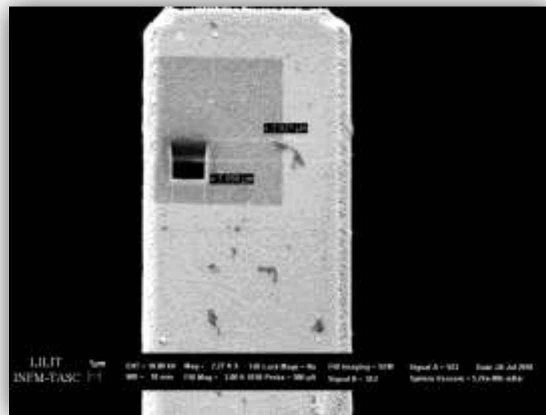

Figure 5.10: The first cubic structure is made with FIB on one of the lateral cantilever. The dimension of the cubic structure is measured after FIB is done. The volume of the cubic structure is 3x3x2µm. The TCC sample is titled forward in order to perform the measurement of the thickness of the cubic structure.

The *SiN TCC* sample is measured after each FIB steps. The results are shown in figure 5.11. We normalized all the plots with respect to the first modes as shown in figure 5.11. The lateral cantilevers have black (outer up which means right cantilever) and grey (outer down which means left cantilever) colors, respectively and the red color is for the central cantilever. The ratio amplitude is between the amplitudes of the lateral cantilevers and the amplitude of the central cantilever in the third mode, as illustrated in figure 5.11**.** The idea behind the FIB experiment was to remove 60pg each time to test the TCC as a mass detection sensor. In this

way, the amount and the position of the removed material can be controlled with a considerable advantage as compared to deposition of the silica beads in the previous section where it resulted impossible to avoid the deposition of beads are around the overhang. Moreover the aim of this experiment was to demonstrated that TTC system is sensitive to the differential mass i.e. to the mass selectively adsorbed (or desorbed as in our case) from one specific cantilever being on the contrary insensitive to unspecific adsorption.

The first cubic structure with FIB is performed as seen in figure 5.10, and the mass of the cubic structure can be calculated by calculating the volume of the cubic structure and the density, for Silicon nitride it is 3100 kg/m^3 according to the Comsol Multiphysics.
As seen in figure 5.11, numbers of cubic structures are increasing from 1 to 3 and resultant graphs are shown beside each design in figure 5.11b to d. We observed from the plots the vibration amplitude of the central cantilever in the third mode increases with increase in the number of cubic structures due to the imbalance in the structure. We also tried to bring back to the balancing condition (one cubic structure case) by adding two cubic structures each on two other cantilevers as shown in figure 5.11e. The steps and specifications are shown in table 1.

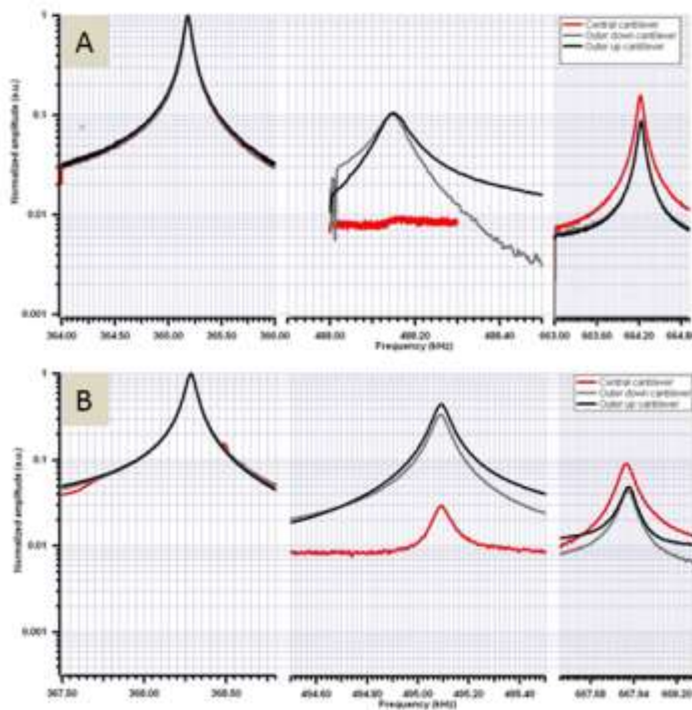

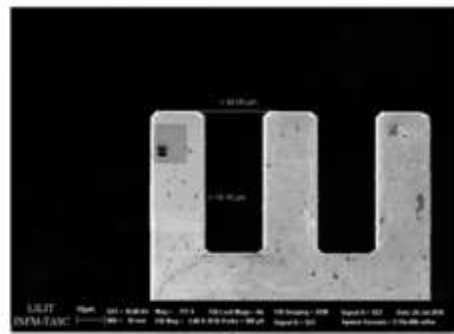

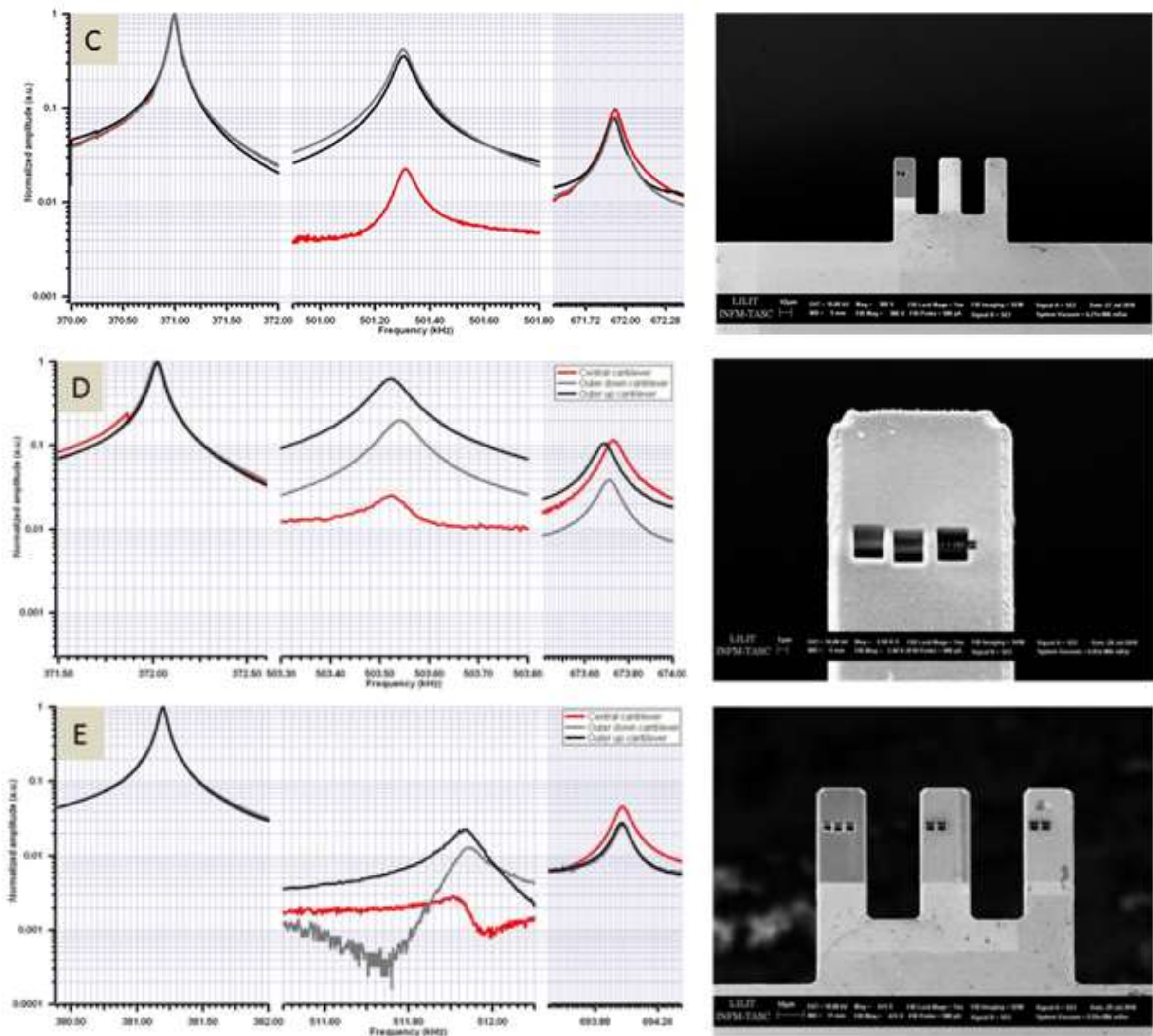

Figure 5.11: Normalized amplitude of vibration of the cantilevers with respect to the frequency. There are five plots of five different FIB steps. The red color is for the central cantilever, the black and grey colors are indicating outer up (left) and down (right), respectively. A) In this plot the cantilevers are not drilled for any cubic structures. The second mode for the amplitude of the central cantilever is around $1x10^{-2}$. B) The first cubic structure is made on one of the lateral cantilever and the amplitude of the central cantilever is increased to $8x10^{-1}$ as indication of symmetry break in the structure. C) The second cubic structure is close to the first one. D) The third cubic structure is made and the vibration amplitudes of outer cantilevers are not equally leveled in vibration amplitudes. E) The last FIB step fourth cubic structures are done and the second mode has an unstable behavior as compared to before.

All the cantilevers are measured for all the distinct modes (first, second and third), as seen in figure 5.11. The second and third modes are normalized with respect to the vibration amplitudes of first mode. The first plot in figure 5.11A, is measured before FIB process. The second and third modes are showing a general TCC behavior.

The readout and actuation is performed by using the frequency pulsed lasers. The detection laser is located close to the free end of the cantilever hence, the laser beam can be partially diffracted by the cubic structure so that the overall intensity in one mode could result

diminished. A second possible explanation come from the well known fact that FIB operation damage the substrate through the implantation of Ga^+ ions which create defects which in turn affect the resonance quality factor. Therefore the frequency measurement for the last step of the FIB process did not show proper results, especially in the second mode for all the cantilevers. Therefore, although the qualitative behavior is consistent with the initial assumption we were not able to produce a quantitative agreement with second mode simulation, as illustrated in figure 5.11D and E. In particular amplitude ratio did not follow a linear relationship with the remode mass and did not recover completely after removing mass from the other cantilevers. The third modes are having more reliable results and therefore we display a table with all the ratio amplitudes for both down (right) and up (left) cantilevers with respect to the central cantilever, see the table 1. The data do not show a linear trend though in general the ratio increases with the increase of the asymmetry of the structure. The more relevant result is that, when the structure recovers, at least partially, the symmetry the ratio decreases again, showing that it depends on the localization of the mass rather than on the overall added/removed mass.

FIB Steps	Cubic structures (60pg each)	Ratio (Up/Central)	Ratio (Down/Central)
No FIB processing	-	0.56	0.56
1	1 (same cantilever)	0.54	0.48
2	1 (same cantilever)	0.82	0.85
3	1 (same cantilever)	0.91	0.34
4	4 (central and the other outer cantilever)	0.60	0.60

Table 1: The zero step in FIB step means that the TCC device was measured before the FIB process. The other steps of FIB show that for each step one cubic structure was added to the one of the cantilever. 4 cubic structures were added at the last step of FIB process. Two cubic structures are added to the central and to the one of the outer cantilever. Calculation of the ratio amplitudes of the upper and down cantilevers are written with respect to the central cantilever.

5.8 A proposal for a Micromechanical Transistor (μMT)

One particular field in MEMS that has a growing interest in the electronic and communication markets [116] is RF-MEMS with various RF applications such as switches, resonators, and filters etc. Operation of MEMS analog devices are based on the mechanical motion of a resonator. The mechanical motion of the moving parts (cantilevers) is typically controlled by a radio frequency signal force. Different attempts of MEMS switches and circuits can be found in the literature [117,118,119].

The use of coupled cantilevers [120,70,105] for mechanical based logic elements have been

already proposed in the past times. The MEMS devices are good candidates as alternative to the traditional electronic components on the design of multiple RF devices [105,120] i.e. mixers, on/off-switches, oscillators etc. These devices will improve the performance of an electronic system, such as reducing costs, power consumption etc. [121,122] The conventional electronic components of silicon such as FETs and PIN diodes have the disadvantages [123] of high power consumption, low reliability, and high manufacturing cost. The RF MEMS devices are offering miniaturization, integrating and better performance. However, these semiconductor switches have poor isolation at high frequency operation.

The aim of this section is to mimic the Field Effect Transistors (*FET*) device in totally based on mechanical coupled cantilevers transistor.
In traditional *FET* device, an electrical field gates the flow of electrical current through a semiconductor. Instead of using an electrical signal, the new logic devices create the switching field by mechanically deforming a cantilever. The coupled cantilevers are deformed due to the electrostatic voltage (V_{DC}), which lower the oscillation amplitudes of another lateral cantilever. When we apply a RF-signal to across two Au-metal electrodes as shown in figure 5.12, we create a field, which is sufficient to excite the *SiN TCC Electrodes* device into a vibration. By applying a static voltage (V_{DC}) on another cantilever, the cantilever motion will be damped due to the cantilever attraction to the maximum point of the electric field. This can work as damping factor for the whole system, in other words, the DC bias will serve as a gating voltage. This type of device would allow mechanical action to be interfaced with electronics, and could be the basis for a new form of logic device that uses the mechanical resonator instead of field effect transistor. The mechanical alternative to the electronic FET could be extremely advantageous in all those particular conditions where electronics fails, such as at extremely low temperatures, where electrons are frozen inside the semiconductor, or in harsh environment, where surface chemistry determine the response of superficial electron channels, or in presence of damaging radiation that can affect the conductive properties in semiconductor-based transistors.
The *SiN TCC Electrodes* are actuated by the dielectric gradient force. In the following section the actuation will be implemented and applied on the *SiN TCC Electrodes*.

5.8.1 Dielectric gradient force actuation

The new drive scheme is integrated with the cantilevers. It is a local actuation for arbitrary

resonators that is based on electrical signals. The results of optical and dielectric gradient force actuations are shown in figure 5.13.

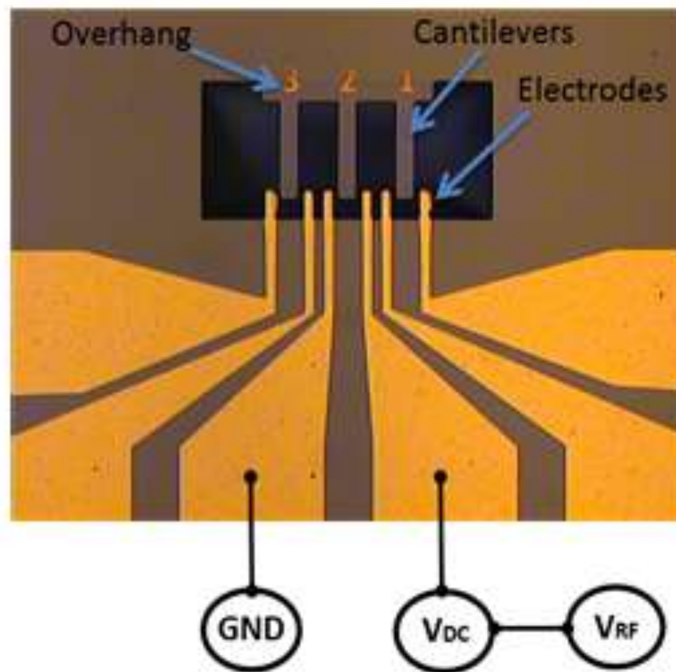

Figure 5.12: It is an optical image of TCC with the dielectric gradient force actuation method. The cantilevers are labeled with numbers in order to better recognize the displacements of each of cantilevers. The yellow electrodes are aligned with the cantilevers. The dielectric gradient force actuation is configured by an electrostatic voltage (V_{DC}) and RF signal (V_{RF}) on cantilever 2.

We have applied two different actuation methods on the same *SiN TCC Electrodes* device. From the previous design *SiN TCC* has shown that the optical actuation could excite all the fundamental modes. Therefore, we used optical actuation also on the new design *SiN TCC Electrodes*. The results are shown in figure 5.13. The dielectric gradient force actuation works by applying electrostatic voltage V_{DC} and radio frequency signal V_{RF} on the central cantilever as shown in figure 5.13a. The optical actuation works by using a frequency-pulsed laser on the overhang of the *SiN TCC Electrodes*, as shown in figure 5.13b. All the modes are plotted for all the cantilevers as shown in figure 5.13b. Few difference can be observed in the two actuation method. First, dielectric actuation imposes equal amplitude on all the cantilevers in all the modes, while optical actuation produces differences in amplitude as predicted by FEM, although in this particular device it wasn't possible to obtain a perfect symmetry. Second resonance width is much larger in electrostatic actuation, inditaing that the induced cantilever polarization is actually dissipating energy and is the dominant effect in this actuation mode.

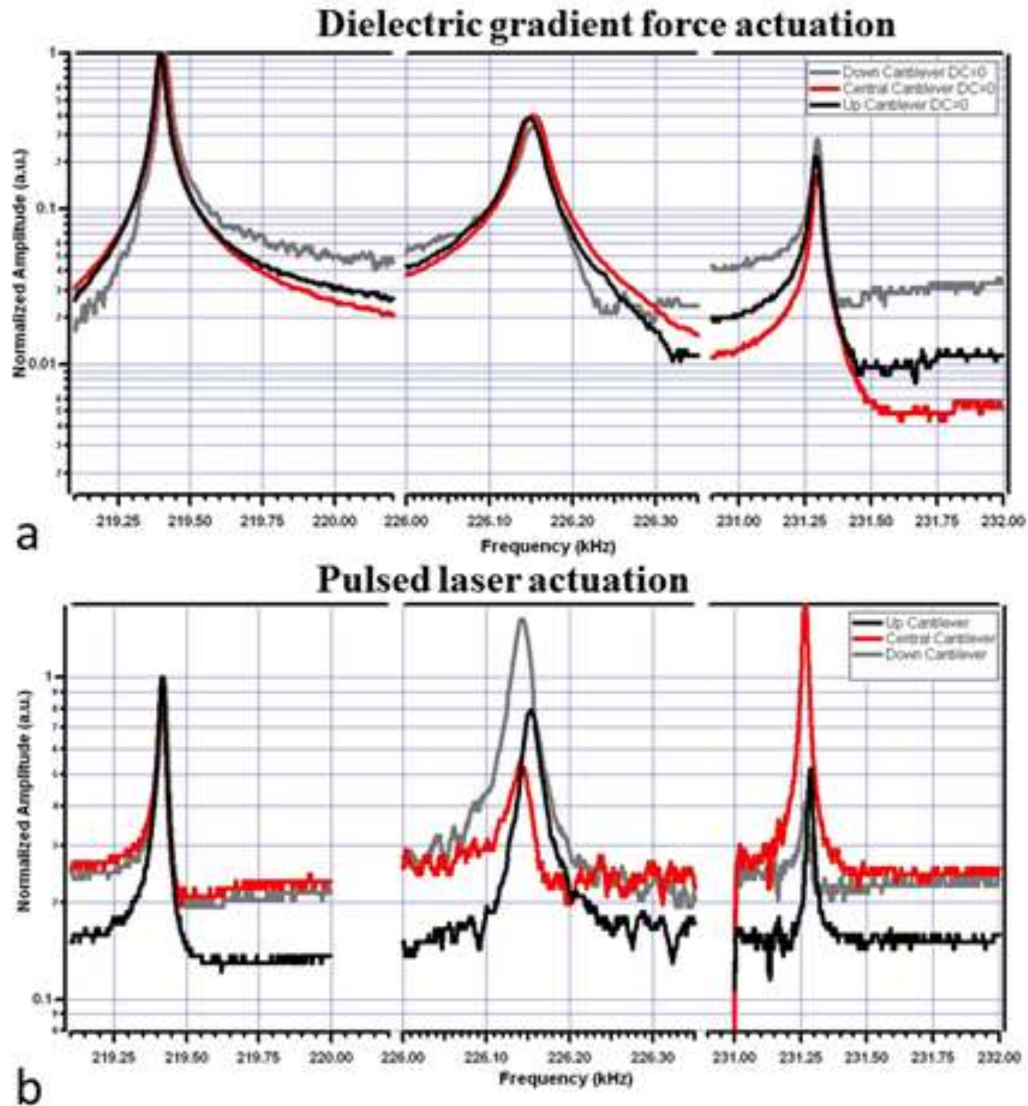

Figure 5.13: Plot of frequency response vs. displacement amplitude. The black and grey is representing the lateral cantilevers, respectively. The red stands for central cantilever. Two different actuation techniques are used. a) the dielectric gradient force actuation method is used and all the modes are shown as it is the case of the optical actuation. b) the frequency-pulsed laser is used on the new design *SiN TCC Electrodes*. The modes are comparable with the dielectric gradient force technique.

We have shown that a dielectric cantilever can oscillate when a static voltage applies with a modulation signal, then the cantilever attracts towards the maximum field strength because of the inhomogeneous electric field, as shown in figure 5.13a. The inhomogeneous field in the cantilever is created by two Au-electrodes, as shown in figure 5.12 for the central cantilever. A static voltage V_{DC} applied to the electrodes induces a strong dipolar moment in the cantilever that in turn experiences an attractive force directed towards the electrodes. Modulating V_{DC} with an RF-signal V_{RF} gives rise to an oscillating force component that drives the cantilever perpendicularly to the sample plane.

We apply a static voltage on one of the oscillating lateral cantilevers. The static voltage is also

a spatially non-uniform field; thereby the cantilever will try to remain in the maximum field region and a restoring force against the motion will be developed, decreasing the oscillation amplitude. The field force works like a damping force for the applied lateral cantilevers, because of the polarization dissipation mentioned before. Thanks to the fact that the TCC system is made of three strongly entangled cantilevers which are, on the other hand, spatially separated, it is possible to create on the same oscillator a damping field separated from the oscillating field. In spite of the fact that the two are applied to two distinct cantilevers, they affect the same oscillating system exactly in the same way two distinct voltages, V_{SD} and V_G, affect the current in the channel of a FET. It is worth to stress here that, if a DC voltage is applied on the same cantilever on which the RF voltage is applied, the oscillation amplitude is ***increased*** by a factor $1 + V_{DC}/V_{RF}$.

With these two properties:

- Applying V_{DC} and V_{RF} on central cantilever
- Applying $V_{damping}$ on one of the lateral cantilevers

These two properties together to conceive a sort of micromechanical transistor

Before the micromechanical transistor introduces, the FET device is explained, because the micromechanical transistor has many similarities with FET device.

5.9 Field Effect Transistor (FET)

In this section the concept of FET device will be presented. We can make an analogy between the FET device and the micromechanical transistor. In the figure 5.14, the FET device will be introduced in a simple schematic diagram.

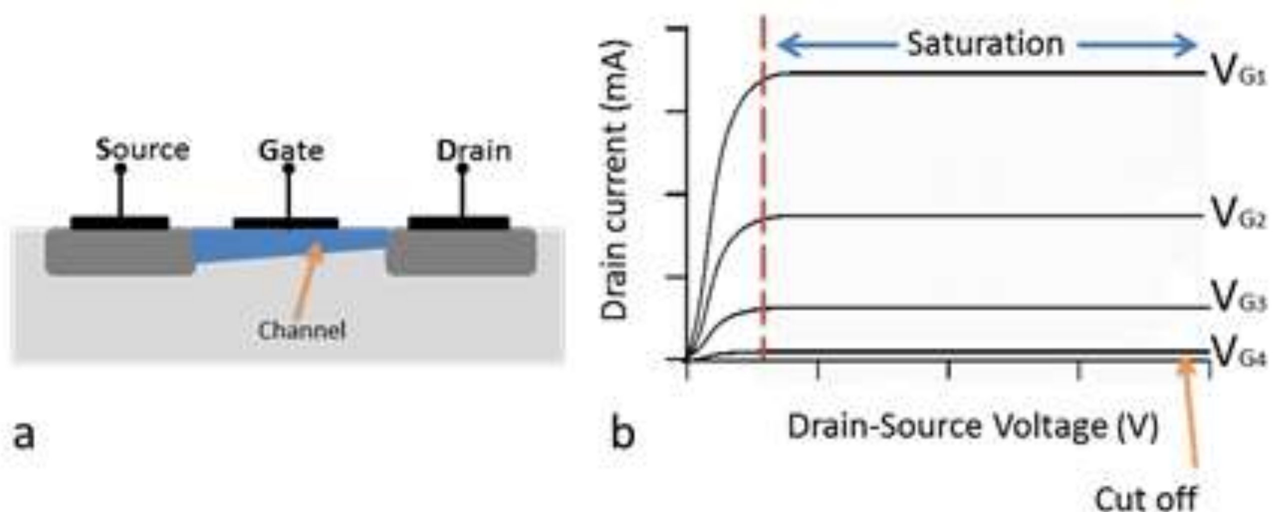

Figure 5.14: A schematic of diagram of Field Effect Transistor (FET) in cross section. a) The S stands for source, D is drain current and the G is representing gate voltage. The current is flowing from the source to the

drain, I_{DS}. The gate voltage, V_G, is controlling the current between the source and drain channel as shown with the blue color. b) The I-V characteristic of FET is shown. In the initial stage of the V_{DS} and I_D is linear. When the V_{DS}, is reaching the threshold value starts the I_D to saturate. The level of the ID is decided by the gate voltage. [124]

The I-V characteristic behavior of FET device can be divided in three regions. The first region or called cut off, the current is zero (I_D=0) and the FET device is acting as an insulator, when the V_{DS} is smaller than the pinched off voltage (V_t). In the second region, the FET device is acting like a linear resistor because the value of the drain-source voltage (V_{DS}) is > pinched voltage (V_t) as shown in figure 5.14b. The third region, or called the saturation region, where the FET device is controlled by the gate voltage (V_G), means that the current is not increasing further as the drain-source voltage is increasing. We can see that for a given value of gate voltage (V_G), the current is constant. If the voltage gate, V_{G1} negatively increases, the conduction channel will narrow and the current flow between the source and the drain will be reduced, as it is shown in figure 5.14b. The first gate voltage V_{G1} is usually zero; therefore the I_D has the highest current flow. When the gate voltage V_{G4} is reached a sufficient enough negative value the channel will stop flow of the current between the source and drain channel, also called cut off [124], as is shown in figure 5.14b.

The main three operations of FET are:

1) Cut-off regime where no channel exists (V_t>V_G) and I_D = 0 for any V_{DS}

2) Linear resistor regime (V_G > V_t).

3) Saturation regime in which the channel is pinched means (V_G>V_t) and I_D is not increased as V_{DS} increases.

The final goal of the project is the development of a full micromechanical transistor using *SiN Electrodes TCC*. In a transistor a high power signal is controlled by a low power signal, thus obtaining amplification. In a FET device, at V_{DS} (the input voltage) constant, the output current I_{DS} is controlled by the Gate Voltage, V_G. Since I_G is negligible, the FET acts as an amplifier. In our device an oscillating bias V_{RF} applied to one cantilever 2 is used to put the three cantilevers in oscillation, as seen in figure 5.12. A second cantilever is exposed to a DC bias that damps the cantilever motion, which is detected on the third cantilever. So, the oscillation amplitude of the *SiN Electrodes TCC* is controlled by the DC signal, which, having no RF components is a low power signal, while both excitation and oscillation are RF signal and thus high power signal. Therefore we obtain an amplification effect. Proof of principle investigations were performed and suggest that the device proposed is working as expected.

In the following the analogy of FET and μmechanical transistor are listed.

FET	μMT
V_{DS} →	Actuation amplitude V_{RF}
V_G →	Damping voltage V_{DC}
I_{DS} →	Oscillation amplitude

The saturation region in a FET device is related to the no current increases further as drain-source voltage increases. The saturation region for micromechanical transistor is illustrated by figure 5.15.

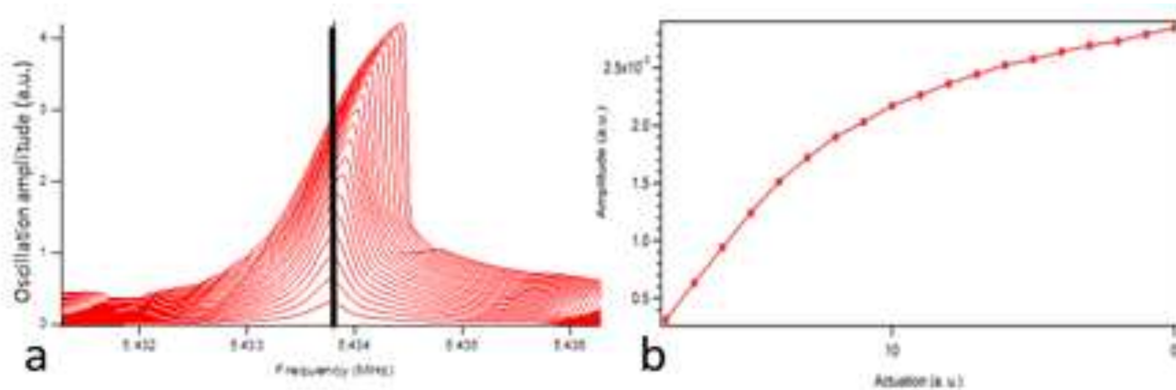

Figure 5.15: Oscillation amplitude vs. frequency for a given resonator. a) The black line is taken at the peak-value of the lowest oscillation amplitude. The points are plotted in the right side. b) Oscillation amplitude vs. actuation voltage (V_{RF}). It is clear that the actuation voltage is linear to certain value, and then the oscillation amplitude starts to reach a plateau [125].

The magnitude response curves at various driving amplitudes are shown in figure 5.15a. At large amplitudes, the frequency response becomes nonlinear due to second order mechanical properties such as stretching of the resonator. The deflection of the resonator shows that with modest excitation voltages, motion beyond the onset of nonlinearity [126] is obtained. At larger excitations the oscillation amplitude is increased and the resonator is stretched, and, as in guitar strings under tension, the resonance frequency is shifted to higher values. As the frequency is swept from low to high, it reaches a point that is no longer stable and so it rapidly switches to the next stable state at lower amplitude.

The overall effect is that exciting the mechanical resonator at fixed frequency above a certain amplitude the oscillation amplitude is not going to increase as actuation voltage (V_{RF}) increases, as shown in figure 5.15b.

The experimental results of the *SiN Electrodes TCC* are measured by applying V_{RF} and V_{DC} on the lateral cantilever as shown in figure 5.16, and the measured the I_{DS}, oscillation of the lateral cantilever as shown in figure 5.16 by using a CW green laser and photodiode, as shown in figure 5.2c.

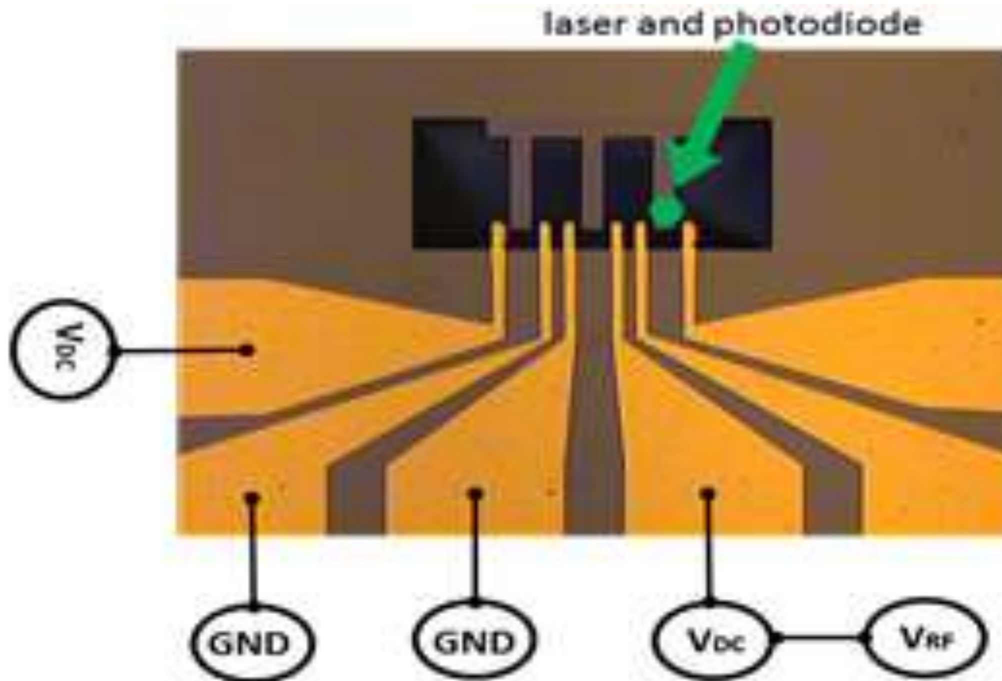

Figure 5.16: The configuration of micromechanical transistor is shown by applying a static voltage (V_{DC}) on the left cantilever, V_{RF} signal on the central cantilever and the output signal, which is the oscillation amplitudes are measured by the right cantilever, where the green arrow is pointing on the green laser spot. The value of the damping voltage V_{DC} and actuation voltage V_{RF} are varying from 0V to 4V in all the three modes.

The results of measurement of the right cantilever in first, second and third modes with varying the actuation and damping voltage from 0V to 4V are plotted in figure 5.17.

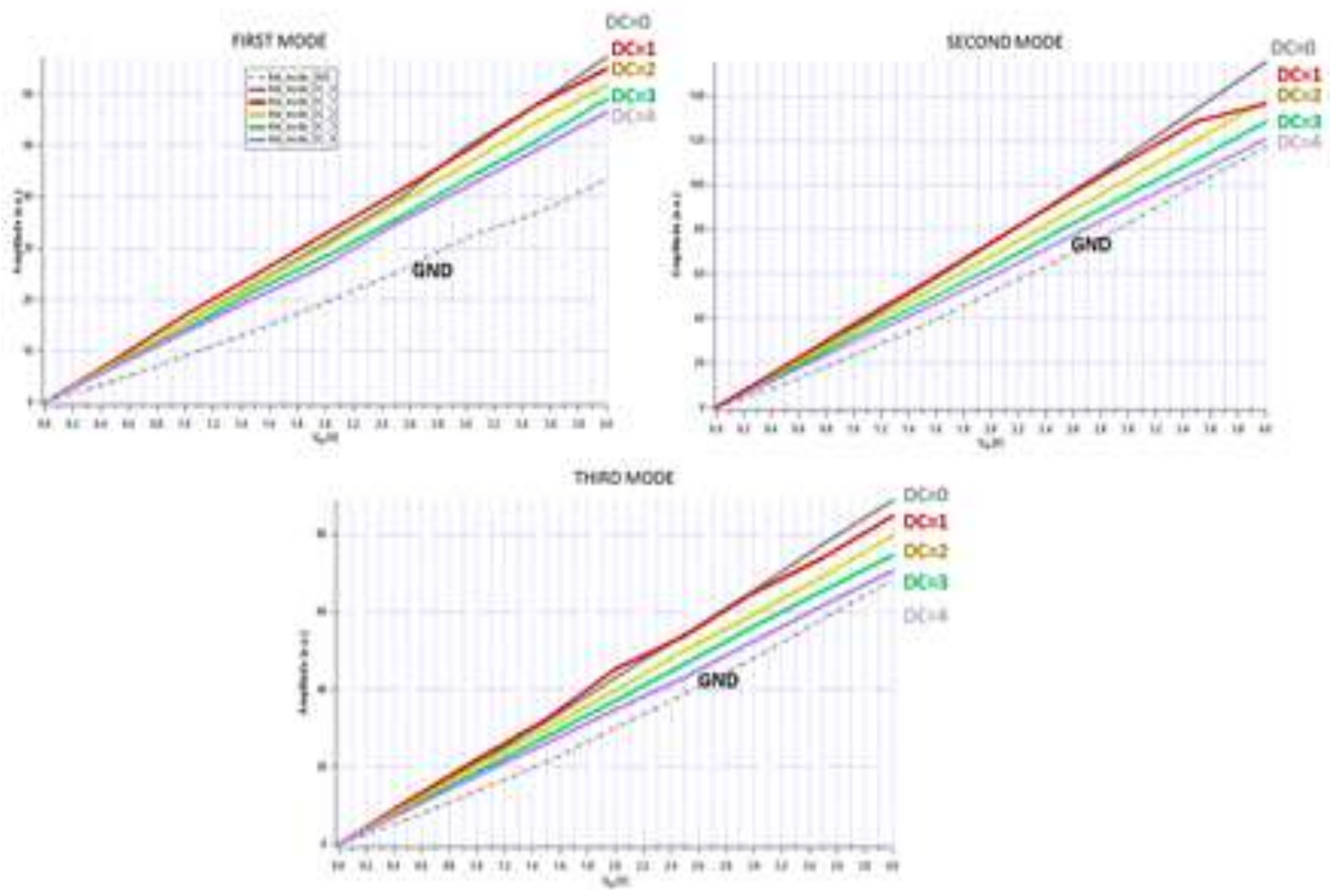

Figure 5.17: Oscillation amplitude vs. actuation voltage. The actuation and damping voltage is from 0V to 4V, respectively. The oscillation amplitude of the right cantilever is decreasing in the five damping voltage values.

The results of micromechanical transistor has shown that it has the tendency of the FET device in the linear resistor regime. The results do not show the saturation regime; which is more easily obtained in microbridges, which are clamped at the two ends and therefore experience larger non linear effect. On the other hand the TCC approach can be applied also to suspended microbridges, therefore more investigation in the direction are envisaged.

However, our work with coupled cantilever transistor device provides a first implementation of a new approach to analog operations that performs mechanical-electrical actions in one structural unit using a single material. This new family of transistors-like micromechanical devices could provide new processing and memory capabilities in very small and portable devices.

5.10 Cell Growth on Cantilever

We performed an preliminary experiment on GT1 cells which are used as a neuronal cell hypothalamic cell line. The GT1 cells are grown on the cantilevers according to the protocol explained by Didonna A. et al [127]. Those cells are grown on the cantilever, as shown in figure 5.18a, 5.19a. The cells grow well on the cantilevers and the images in figure 5.18b, 5.19b show that the cells were grown on the cantilever and close to the edge of the paddle. Using the standard protocol for fluorescence to recognize the nuclei to define number of cells are shown in figure 5.18b and 5.19b.

With the technique of resonance frequency shift method the weight of the cells can be defined. The cells are dried and fixed so it is possible to perform the measurement in low vacuum. The cantilevers were measured before the treatment with the cells. Afterwards the cantilevers were prepared to be measured with the dried cells. In this way the weight of the cells can be found and compared with the nuclei on the images performed.

The image in figure 5.18b, shows that there three cells on the base of the cantilever. This can change the mechanical property of the cantilever's resonance frequency

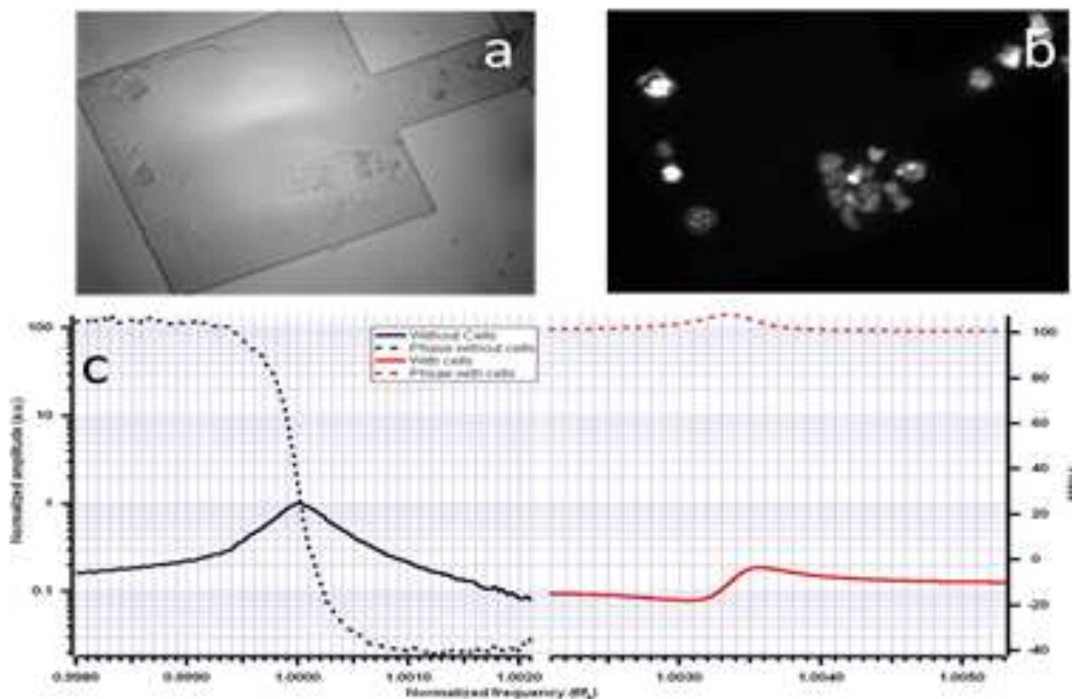

Figure 5.18: The frequency is normalized with the without cell resonance frequency. The y-axis is the normalized vibration amplitude of the cantilever. The opposite y-axis is the phase profile. a) The cantilever after the fabrication process. The dimensions of the cantilever are 200x200x2μm^3. b) The fluorescence image of the cells on the cantilever to count the number of the cells that are grown after the treatment of the cell growth. c) The frequency response is performed before and after. The black color is before cells on top of the cantilever. The red color is after the cell treatment. The dotted lines are the phase of the cantilever.

In principle the resonance frequency of a mechanical resonator should decrease as the mass of the cantilever increases. In this case the resonance frequency is increasing due to cells grown on the base results the stiffening of the cantilever elastic constant, as shown in figure 5.19b. The next example is shown that the cells are not grown on the base.

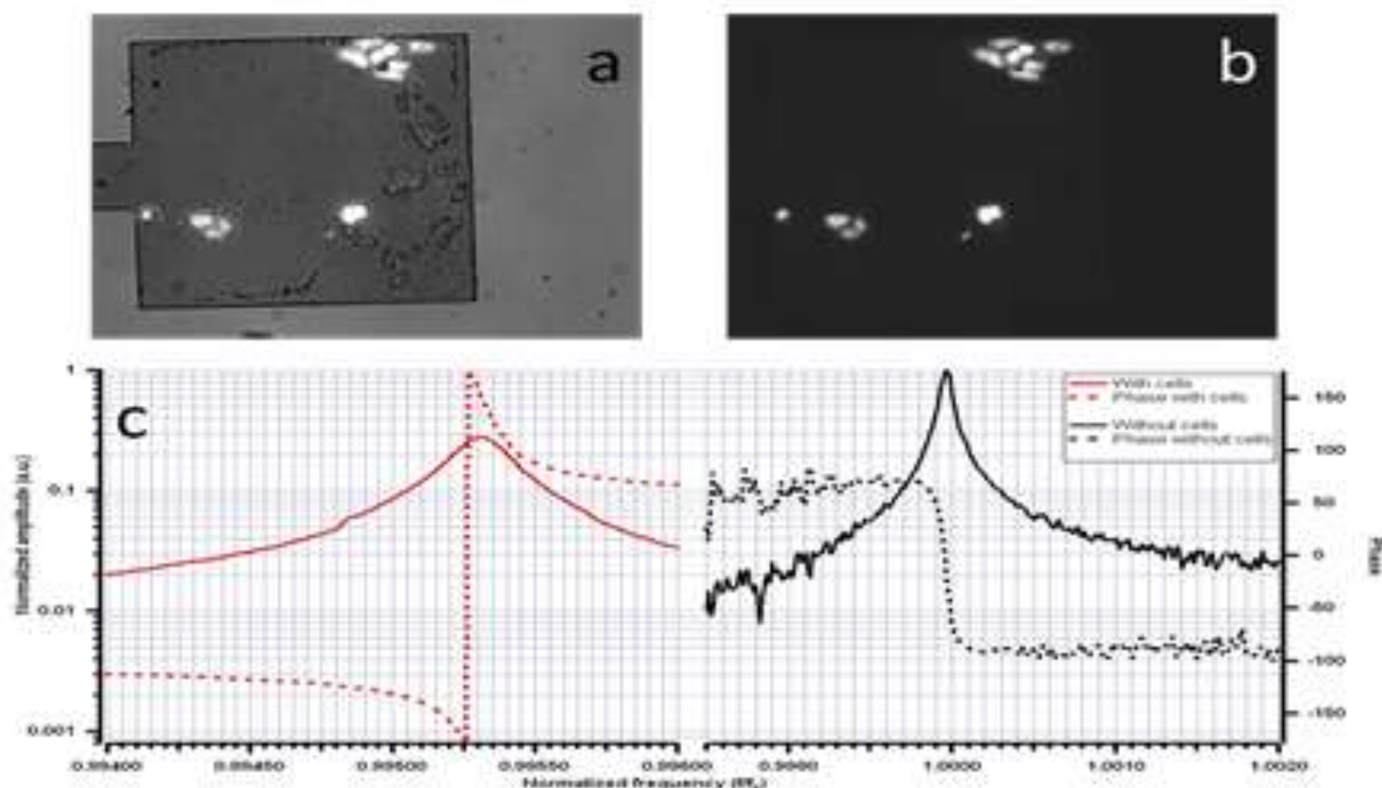

Figure 5.19: The frequency is normalized. The y-axis is the normalized vibration amplitude of the cantilever. The opposite y-axis is the phase profile. a) The cantilever after the fabrication process. The dimensions of the cantilever are 200x200x2μm^3. b) The fluorescence image of the cells on the cantilever to count the number of the cells that are grown after the treatment of the cell growth. c) The frequency response is performed before and after. The black color is before cells on top of the cantilever. The red color is after the cell treatment. The dotted lines are the phase of the cantilever.

In this experiment the cells are not grown on the base, figure 5.19b. We observed the resonance frequency is decreasing after the cells are added. This measurements allowed us to evaluate the cellular mass in 0.5pg on average per cell. A further AFM analysis – not performed – would allow the estimation of the cell density. Other cantilever measurements are reported in the appendix E. The main improvement is to cover the base for cells, which can affect the cell growth and the cantilever will not perform as normal mechanical resonator.

6 CONCLUSIONS

Three identical microcantilevers are coupled and the mechanical behavior is changed from a single cantilever. The coupling gave three unique modes with distinct symmetry and resonance frequency. The first mode is characterized by all the microcantilevers oscillating at the same amplitude and phase. The second mode shows that the central cantilever has no movement and the lateral cantilevers have a movement but in antiphase. In the third mode, the central one is moving more than the lateral cantilevers. The lateral cantilevers are in the same phase than the central one. The value of the length of overhang gives the necessary coupling effect to obtain the usual distinct modes with the highest vibration amplitudes.

A Finite Element analysis of the mechanical behavior have been performed and the results have been employed to design the best structure. Moreover, the sensitivity of the devices have been determined.

Triple coupled cantilever (TCC) systems were fabricated on Silicon on Insulator wafer and on Si_3N_4 suspended membrane using KOH-etch back-release technique.
We observe numerous defects and disadvantages with this SOI device. The etching profiles of silicon oxide shows that the overhang and the cantilevers are not properly etched and not following the symmetry. This may lead to vary the mechanical properties of the device means the central cantilever may not operate as desired. Therefore, we made the TCC device with SiN. Hence, we conclude that the performance of TCC device with SiN is a better device compared to device with SOI to use as mass sensor. The experimental results obtained are also supportive to the this argument and were presented .

Measurements show that the amplitude of oscillation of the central cantilever in the second mode is negligible and an amplitude ratio better that 100 is obtained. Using these devices,

preliminary results indicated that a mass down to 1pg can be detected.

Focused ion beam lithography is used to make cubic structures in order to remove materials in a controlled manner in order to demonstrate the intrinsic sensitivity of our device to mass localization and the relative insensitivity to a-specific adsorbed mass. .

An electrostatic actuation of the TCC devices has been implemented using a self-aligned configuration. This original configuration has been used to implement a micromechanical analogous of an electronic transistor. In this approach, which takes advantage of the mechanical entanglement of the three spatial separated cantilevers that form a TCC, one cantilever is excited with an RF bias while a second one is damped by a DC bias and the oscillation amplitude is monitored on the third one. The results of micromechanical transistor were limited to the linear regime, but a not negligible gating effect was demonstrated..

Our work with coupled cantilever transistor device provided a first implementation of a new approach to analog operations that performs mechanical-electrical actions in one structural unit using a single material. This new family of transistors-like micromechanical devices could provide new processing and memory capabilities in extreme environmental conditions, such as at very low temperature or in presence of high energy radiation.

Finally, the results of the grow of GT1 cells on the paddle has shown that the cells are grown on the cantilever and therefore gives a stiffer cantilever and thereby changing the resonance frequency to higher resonance frequency. We need to make the cells grow on the paddle and not on the cantilevers, so more investigations are needed. However we showed that it is possible to count and detect the mass of single cells.

Appendix A – Details of simulation of TCC

This appendix describes the details of simulations of TCC by Comsol

COMSOL Model Report

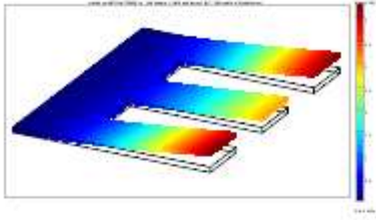

1. Table of Contents

- Title - COMSOL Model Report
- Table of Contents
- Model Properties
- Geometry
- Geom1
- Geom2
- Materials/Coefficients Library
- Solver Settings
- Postprocessing
- Variables

2. Model Properties

Property	**Value**
Model name	
Author	
Company	
Department	
Reference	
URL	
Saved date	Nov 15, 2011 7:12:37 PM
Creation date	Nov 12, 2011 12:03:16 PM
COMSOL version	COMSOL 3.5.0.603

File name: D:\Phd project\PhD Thesis\Simulation\frequency_vs_width_overhang\cantilever length 50\TCC_50_overhang_100.mph

Application modes and modules used in this model:

- Geom1 (3D)
    - Solid, Stress-Strain (MEMS Module)

- Geom2 (2D)

3. Geometry

Number of geometries: 2

3.1. Geom1

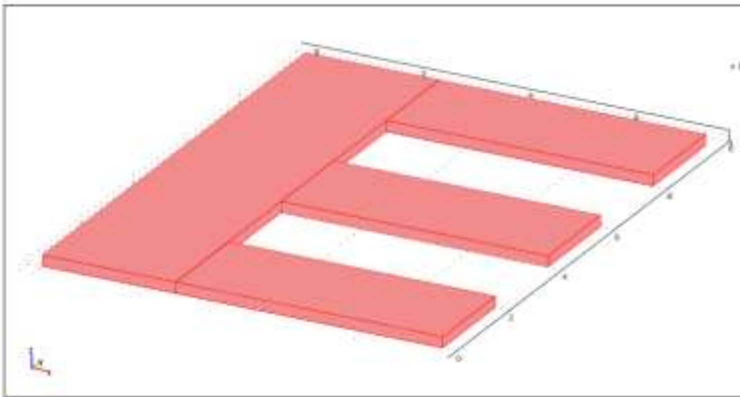

3.1.1. Point mode

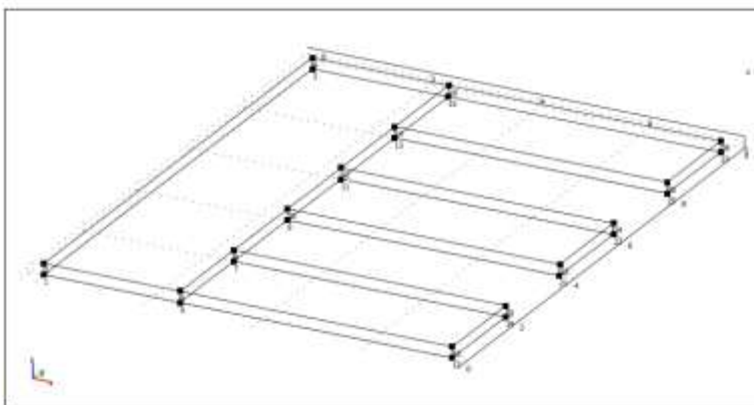

3.1.2. Edge mode

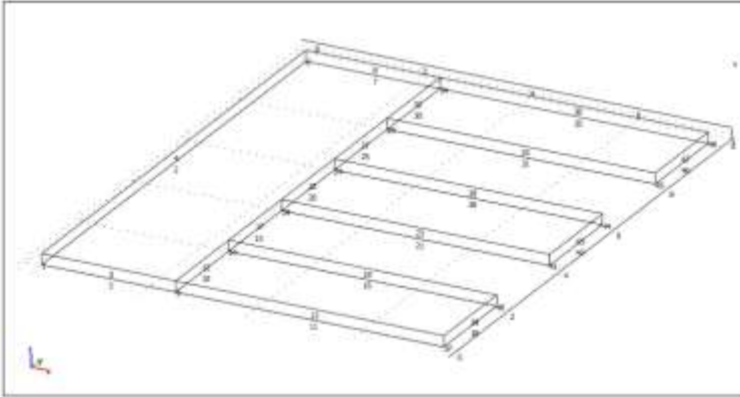

3.1.3. Boundary mode

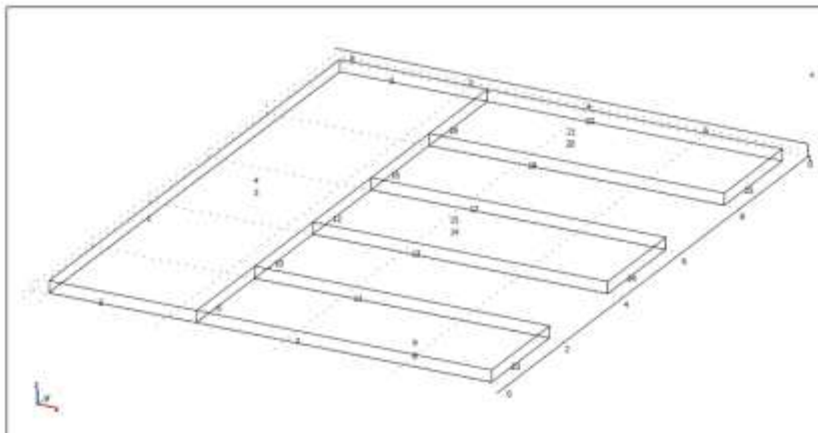

3.1.4. Subdomain mode

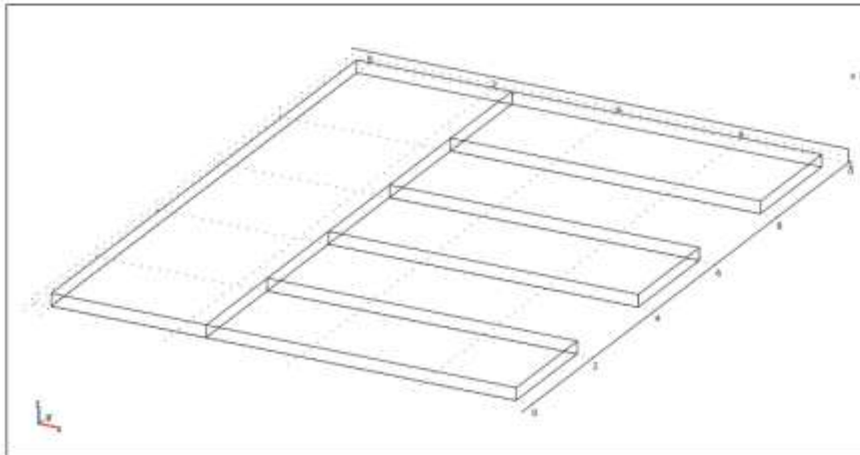

3.2. Geom2

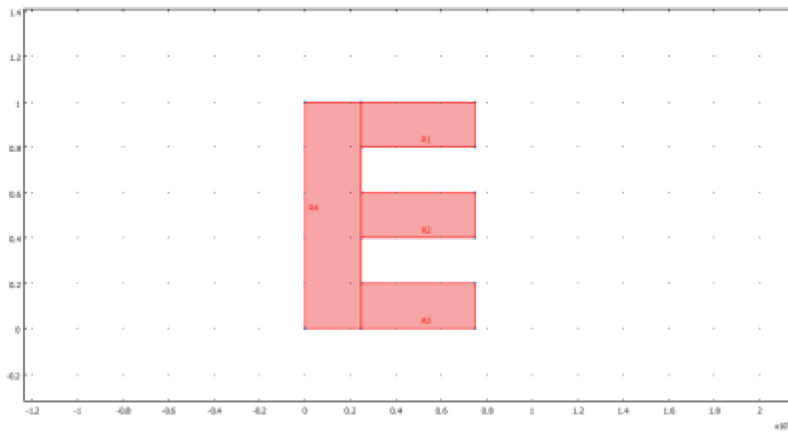

4. Geom1

Space dimensions: 3D

Independent variables: x, y, z

4.1. Mesh

4.1.1. Mesh Statistics

Number of degrees of freedom	131535
Number of mesh points	6916
Number of elements	24498
Tetrahedral	24498
Prism	0

Hexahedral	0
Number of boundary elements	11152
Triangular	11152
Quadrilateral	0
Number of edge elements	626
Number of vertex elements	28
Minimum element quality	0.278
Element volume ratio	0.074

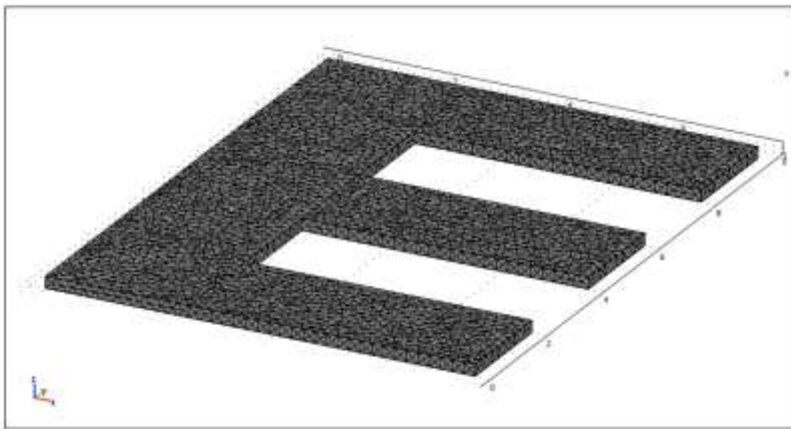

4.2. Application Mode: Solid, Stress-Strain (smsld)

Application mode type: Solid, Stress-Strain (MEMS Module)

Application mode name: smsld

4.2.1. Scalar Variables

Name	Variable	Value	Unit	Description
jomega	jomega_smsld	-lambda	rad/s	Complex angular frequency
t_old_ini	t_old_ini_smsld	-1	s	Initial condition previous time step (contact with dynamic friction)
refpntx	refpntx_smsld	0	m	Reference point moment computation x coord.
refpnty	refpnty_smsld	0	m	Reference point moment computation y coord.
refpntz	refpntz_smsld	0	m	Reference point moment computation z coord.

4.2.2. Application Mode Properties

Property	**Value**
Default element type	Lagrange - Quadratic

Analysis type	Eigenfrequency
Large deformation	Off
Specify eigenvalues using	Eigenfrequency
Create frame	Off
Deform frame	Frame (ref)
Frame	Frame (ref)
Weak constraints	Off
Constraint type	Ideal

4.2.3. Variables

Dependent variables: u, v, w, p

Shape functions: shlag(2,'u'), shlag(2,'v'), shlag(2,'w')

Interior boundaries not active

4.2.4. Boundary Settings

Boundary		2-5, 7-11, 13-17, 19-25	1
constrcond		Free	**Fixed**

4.2.5. Subdomain Settings

Subdomain		1-4
Young's modulus (E)	Pa	**250e9[Pa] (Si3N4)**
Density (rho)	kg/m^3	**3100[kg/m^3] (Si3N4)**
Thermal expansion coeff. (alpha)	1/K	**2.3e-6[1/K] (Si3N4)**
Poisson's ratio (nu)	1	**0.23 (Si3N4)**

5. Geom2

Space dimensions: 2D

Independent variables: x, y, z

6. Materials/Coefficients Library

6.1. Si_3N_4

Parameter	**Value**
Heat capacity at constant pressure (C)	700[J/(kg*K)]
Young's modulus (E)	250e9[Pa]
Thermal expansion coeff. (alpha)	2.3e-6[1/K]
Relative permittivity (epsilonr)	9.7
Thermal conductivity (k)	20[W/(m*K)]
Poisson's ratio (nu)	0.23
Density (rho)	3100[kg/m^3]
Electric conductivity (sigma)	0[S/m]

7. Solver Settings

Solve using a script: off

Analysis type	Eigenfrequency
Auto select solver	On
Solver	Eigenfrequency
Solution form	Automatic
Symmetric	auto
Adaptive mesh refinement	Off
Optimization/Sensitivity	Off
Plot while solving	Off

7.1. Direct (SPOOLES)

Solver type: Linear system solver

Parameter	**Value**
Pivot threshold	0.1
Preordering algorithm	Nested dissection

7.2. Eigenfrequency

Parameter	**Value**
Desired number of eigenvalues	3
Search for eigenvalues around	0
Eigenvalue tolerance	0.0
Maximum number of eigenvalue iterations	300
Dimension of Krylov space	0

7.3. Advanced

Parameter	**Value**
Constraint handling method	Elimination
Null-space function	Automatic
Automatic assembly block size	On
Assembly block size	1000
Use Hermitian transpose of constraint matrix and in symmetry detection	Off
Use complex functions with real input	Off
Stop if error due to undefined operation	On
Store solution on file	Off
Type of scaling	Automatic
Manual scaling	
Row equilibration	Off
Manual control of reassembly	Off

Load constant	On
Constraint constant	On
Mass constant	On
Damping (mass) constant	On
Jacobian constant	On
Constraint Jacobian constant	On

8. Postprocessing

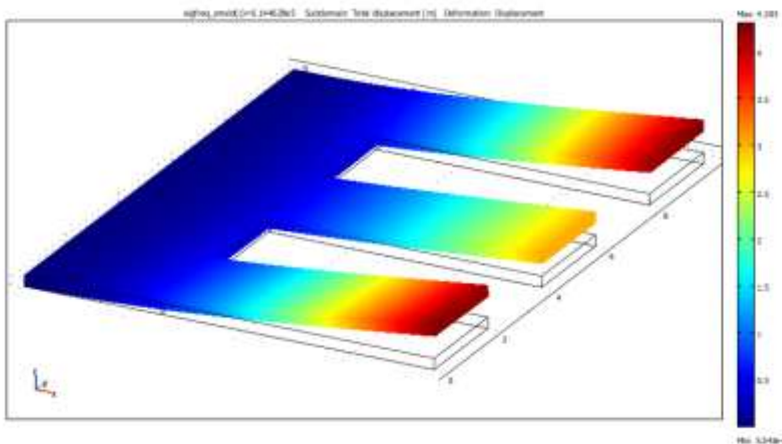

8.1. Eigenfrequency

614462.7741527525
648275.854840554
773177.0359670842

9. Variables

9.1. Point

Name	Description	Unit	Expression
Fxg_smsld	Point load in global x dir.	N	0
Fyg_smsld	Point load in global y dir.	N	0
Fzg_smsld	Point load in global z dir.	N	0
disp_smsld	Total displacement	m	sqrt(real(u)^2+real(v)^2+real(w)^2)

9.2. Edge

Name	Description	Unit	Expression
Fxg_smsld	Edge load in global x-dir.	N/m	0
Fyg_smsld	Edge load in global y-dir.	N/m	0
Fzg_smsld	Edge load in global z-dir.	N/m	0
disp_smsld	Total displacement	m	sqrt(real(u)^2+real(v)^2+real(w)^2)

9.3. Boundary

Name	Description	Unit	Expression
Fxg_smsld	Face load in global x-	N/m^2	0

	dir.		
Fyg_smsld	Face load in global y-dir.	N/m^2	0
Fzg_smsld	Face load in global z-dir.	N/m^2	0
disp_smsld	Total displacement	m	sqrt(real(u)^2+real(v)^2+real(w)^2)
Tax_smsld	Surface traction (force/area) in x dir.	Pa	sx_smsld * nx_smsld+sxy_smsld * ny_smsld+sxz_smsld * nz_smsld
Tay_smsld	Surface traction (force/area) in y dir.	Pa	sxy_smsld * nx_smsld+sy_smsld * ny_smsld+syz_smsld * nz_smsld
Taz_smsld	Surface traction (force/area) in z dir.	Pa	sxz_smsld * nx_smsld+syz_smsld * ny_smsld+sz_smsld * nz_smsld

9.4. Subdomain

Name	Description	Unit	Expression
Fxg_smsld	Body load in global x-dir.	N/m^3	0
Fyg_smsld	Body load in global y-dir.	N/m^3	0
Fzg_smsld	Body load in global z-dir.	N/m^3	0
disp_smsld	Total displacement	m	sqrt(real(u)^2+real(v)^2+real(w)^2)
sx_smsld	sx normal stress global sys.	Pa	4 * G_smsld * ex_smsld/3-2 * G_smsld * ey_smsld/3-2 * G_smsld * ez_smsld/3-p
sy_smsld	sy normal stress global sys.	Pa	4 * G_smsld * ey_smsld/3-2 * G_smsld * ex_smsld/3-2 * G_smsld * ez_smsld/3-p
sz_smsld	sz normal stress global sys.	Pa	4 * G_smsld * ez_smsld/3-2 * G_smsld * ex_smsld/3-2 * G_smsld * ey_smsld/3-p
sxy_smsld	sxy shear stress global sys.	Pa	2 * G_smsld * exy_smsld
syz_smsld	syz shear stress global sys.	Pa	2 * G_smsld * eyz_smsld
sxz_smsld	sxz shear stress global sys.	Pa	2 * G_smsld * exz_smsld
ex_smsld	ex normal strain global sys.	1	ux
ey_smsld	ey normal	1	vy

	strain global sys.		
ez_smsld	ez normal strain global sys.	1	wz
exy_smsld	exy shear strain global sys.	1	0.5 * (uy+vx)
eyz_smsld	eyz shear strain global sys.	1	0.5 * (vz+wy)
exz_smsld	exz shear strain global sys.	1	0.5 * (uz+wx)
sx_t_smsld	Time der. of normal stress global sys. (sx)	Pa/s	E_smsld * ((1-nu_smsld) * ex_t_smsld+nu_smsld * ey_t_smsld+nu_smsld * ez_t_smsld)/((1+nu_smsld) * (1-2 * nu_smsld))
sxy_t_smsld	Time der. of shear stress global sys. (sxy)	Pa/s	E_smsld * exy_t_smsld/(1+nu_smsld)
sy_t_smsld	Time der. of normal stress global sys. (sy)	Pa/s	E_smsld * (nu_smsld * ex_t_smsld+(1-nu_smsld) * ey_t_smsld+nu_smsld * ez_t_smsld)/((1+nu_smsld) * (1-2 * nu_smsld))
syz_t_smsld	Time der. of shear stress global sys. (syz)	Pa/s	E_smsld * eyz_t_smsld/(1+nu_smsld)
sz_t_smsld	Time der. of normal stress global sys. (sz)	Pa/s	E_smsld * (nu_smsld * ex_t_smsld+nu_smsld * ey_t_smsld+(1-nu_smsld) * ez_t_smsld)/((1+nu_smsld) * (1-2 * nu_smsld))
sxz_t_smsld	Time der. of shear stress global sys. (sxz)	Pa/s	E_smsld * exz_t_smsld/(1+nu_smsld)
ex_t_smsld	ex_t normal velocity strain global sys.	1/s	ux * jomega_smsld
exy_t_smsld	exy_t shear velocity strain global sys.	1/s	0.5 * jomega_smsld * (uy+vx)
ey_t_smsld	ey_t normal velocity strain global sys.	1/s	vy * jomega_smsld

eyz_t_smsld	eyz_t shear velocity strain global sys.	1/s	0.5 * jomega_smsld * (vz+wy)
ez_t_smsld	ez_t normal velocity strain global sys.	1/s	wz * jomega_smsld
exz_t_smsld	exz_t shear velocity strain global sys.	1/s	0.5 * jomega_smsld * (uz+wx)
p	Pressure	Pa	-K_smsld * evol_smsld
cp_smsld	Pressure wave velocity	m/s	sqrt((K_smsld+4 * G_smsld/3)/rho_smsld)
cs_smsld	Shear wave velocity	m/s	sqrt(G_smsld/rho_smsld)
mises_smsld	von Mises stress	Pa	sqrt(sx_smsld^2+sy_smsld^2+sz_smsld^2-sx_smsld * sy_smsld-sy_smsld * sz_smsld-sx_smsld * sz_smsld+3 * sxy_smsld^2+3 * syz_smsld^2+3 * sxz_smsld^2)
Ws_smsld	Strain energy density	J/m^3	0.5 * (sx_smsld * ex_smsld+sy_smsld * ey_smsld+sz_smsld * ez_smsld+2 * sxy_smsld * exy_smsld+2 * syz_smsld * eyz_smsld+2 * sxz_smsld * exz_smsld)
evol_smsld	Volumetric strain	1	ex_smsld+ey_smsld+ez_smsld
Ent_smsld	Entropy per unit volume	J/(m^3*K)	mat1_alpha * (sx_smsld-j * (imag(E_smsld * (1-nu_smsld)/((1+nu_smsld) * (1-2 * nu_smsld))) * ex_smsld+imag(E_smsld * nu_smsld/((1+nu_smsld) * (1-2 * nu_smsld))) * ey_smsld+imag(E_smsld * nu_smsld/((1+nu_smsld) * (1-2 * nu_smsld))) * ez_smsld+imag(0) * exy_smsld+imag(0) * eyz_smsld+imag(0) * exz_smsld)+sy_smsld-j * (imag(E_smsld * nu_smsld/((1+nu_smsld) * (1-2 * nu_smsld))) * ex_smsld+imag(E_smsld * (1-nu_smsld)/((1+nu_smsld) * (1-2 * nu_smsld))) * ey_smsld+imag(E_smsld * nu_smsld/((1+nu_smsld) * (1-2 * nu_smsld))) * ez_smsld+imag(0) * exy_smsld+imag(0) * eyz_smsld+imag(0) * exz_smsld)+sz_smsld-j * (imag(E_smsld * nu_smsld/((1+nu_smsld) * (1-2 * nu_smsld))) * ex_smsld+imag(E_smsld * nu_smsld/((1+nu_smsld) * (1-2 * nu_smsld))) * ey_smsld+imag(E_smsld * (1-nu_smsld)/((1+nu_smsld) * (1-2 * nu_smsld))) * ez_smsld+imag(0) * exy_smsld+imag(0) * eyz_smsld+imag(0) * exz_smsld))
tresca_smsld	Tresca stress	Pa	max(max(abs(s1_smsld-s2_smsld),abs(s2_smsld-s3_smsld)),abs(s1_smsld-s3_smsld))

Appendix B – Width of overhang vs. Resonance frequency

Cantilever length 50 microns

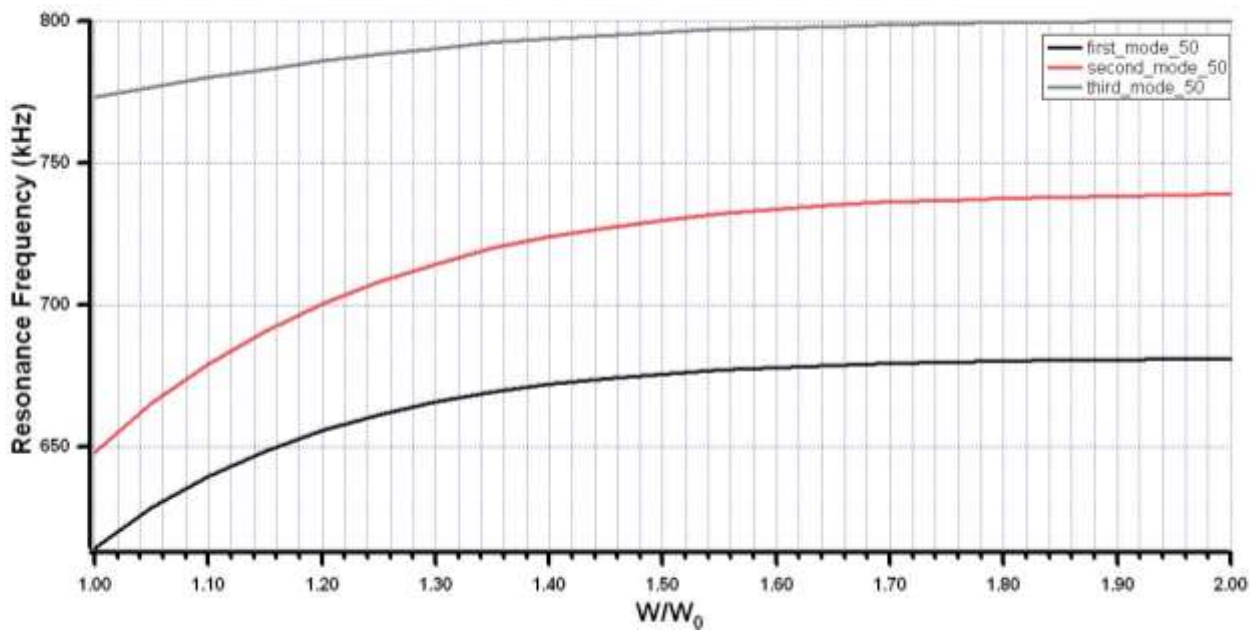

Cantilever length 75 microns

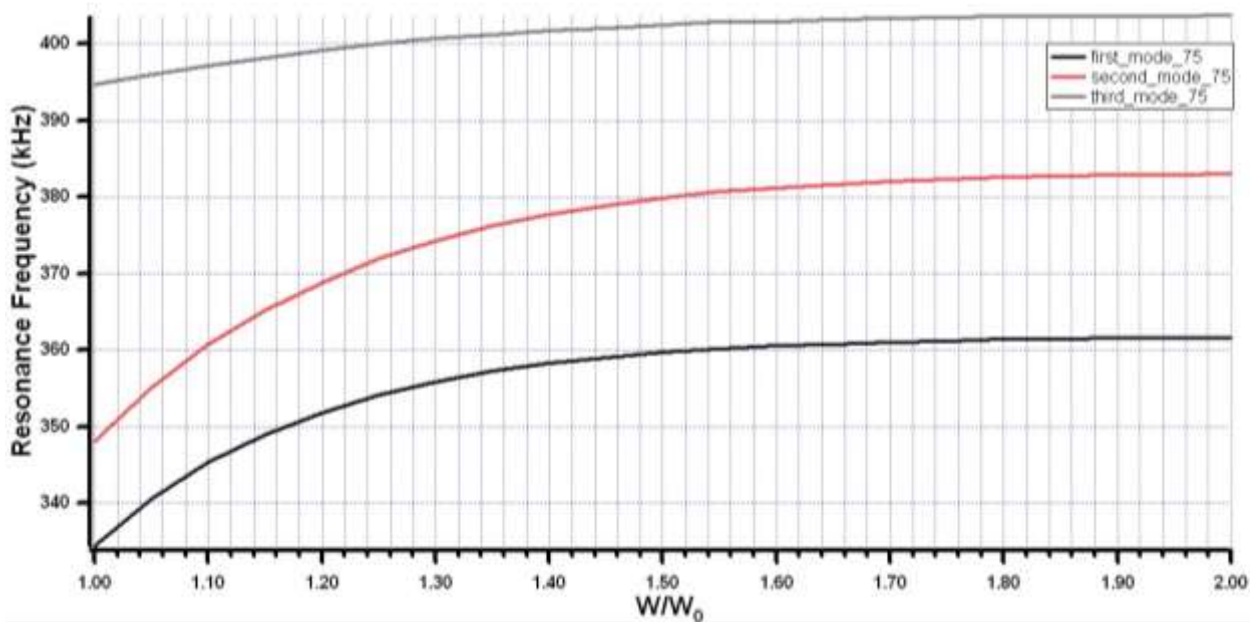

Process flow for TCC

Process flow of *SOI TCC*			
Process Step	**Process Name**	**Recipe / Parameters**	**Comments**
1	SOI Wafer	Cut in 1x1cm^2 squares Clean with ethanol	
2	Spin Coating	PR=S1828 time=50sec, 3000rpm and acc.=2sec thickness= 2µm	
3	Baking	Temperature=110^0 C and time= 2min.	To increase the adhesion
4	Photolithography	Exposure time=25 sec	The sample and the mask is in contact
5	Developer	MF319, 1 min.	Check under microscope
6	Silicon Etching, RIE	CF_4=28.5 sccm O_2 = 1.5 sccm V_{bias}=210 V Power = 100W Pressure inside the chamber = 2.6x10^{-1} Time=25 min.	Check the V_{bias} during the process and regulate it with the pressure knob attached to the chamber. Check the height of the etching height of Silicon with the profilometer.
7	Wet Etching of silicon oxide, BOE	time=1.5 hours	Avoid drying of the sample, otherwise the cantilevers will stick to the substrate.
8	Super Critical Point Drying		This method is used to remove liquid in a controlled manner.

Process flow of *SiN TCC*			
Process Step	**Process Name**	**Recipe / Parameters**	**Comments**
1	Silicon nitride on both sides wafer	Cut in 1x1cm^2 squares Clean with ethanol	
2	Spin Coating	PR=S1828 time=50sec, 3000rpm and acc.=10sec	Spin coating on both sides. thickness= 4µm
3	Baking	Temperature=100^0 C and time= 2min.	
4	Photolithography	Exposure time=30 sec	Bottom of the sample, making

			membrane
5	Developer	MF319, 1 min.	Check under microscope
6	RIE-etching - Silicon nitride	CF_4=28.5 sccm O_2 = 1.5 sccm V_{bias}=250 V Power = 100W Pressure inside the chamber = 2.3x10^{-1} Time=25 min.	.
7	Cleaning	Acetone to clean PR	Avoid drying of the sample, otherwise the cantilevers will stick to the substrate.
8	KOH wet-etching of silicon	temperature = 70°C, solid KOH = 42g, water=0.150L, concentration = 5M	The etching rate is around 50µm/hour. We wait for almost 10 hours.
9	Rinsing	1) Hot water 2) Cold water	
10	Spin Coating	PR=S1828	Same recipe as before
11	Photolithography	Exposure =30sec	This time cantilevers are made on top of the sample. Alignment with the membrane is required
12	Developer	MF319	
13	RIE-Etching of silicon nitride	Same as before	Making TCC out of silicon nitride
14	Cleaning oxygen plasma	O2=30 sccm, Power = 50W, V_{bias}=121V, Pressure inside the chamber=1.21x10^{-1}, time=10min.	If PR is still remained, we can use hot acetone.

Process flow of *SiN Electrodes TCC*			
Process Step	**Process Name**	**Recipe / Parameters**	**Comments**
1	Silicon nitride on both sides wafer	Cut in 1x1cm^2 squares Clean with ethanol	
2	Spin Coating	PR=S1828 time=50sec, 3000rpm and acc.=10sec	Spin coating on both sides. thickness= 4µm
3	Baking	Temperature=100^0 C and time= 2min.	
4	Photolithography	Exposure time=30 sec	The membrane is done on bottom of

			the sample.
5	Developer	MF319, 1 min.	Check under microscope
6	RIE-etching - Silicon nitride	CF_4=28.5 sccm O_2 = 1.5 sccm V_{bias}=250 V Power = 100W Pressure inside the chamber = $2x10^{-1}$ Time=25 min.	
7	Cleaning	Acetone to clean PR	Avoid drying of the sample, otherwise the cantilevers will stick to the substrate.
8	KOH wet-etching of silicon	temperature = 70°C, solid KOH = 42g, water=0.150L, concentration = 5M	The etching rate is around 50µm/hour. We wait for almost 10 hours.
9	Rinsing	1) Hot water 2) Cold water	
10	Spin Coating	First LOR =4000rpm, acc=50 sec. Second PR (S1828)=3000rpm, acc=50sec.	LOR is used for lift-off-resist. Wait 3 min. with spinning to cover the KOH-holes.
11	Baking	LOR heating 180°C for 1 min. PR 120°C for 1 min.	
11	Photolithography	Exposure =30sec	Using mask of the electrodes
12	Developer	MF319 for 50 sec.	
13	E-beam evaporator	Ti=10nm Au=40nm	Deposition of gold on the electrodes
14	Lift-Off process	MF319	By carefully shaking the glass within the sample, the resist and LOR will be dissolved.

Appendix D –Detailed drawings of the vacuum chamber

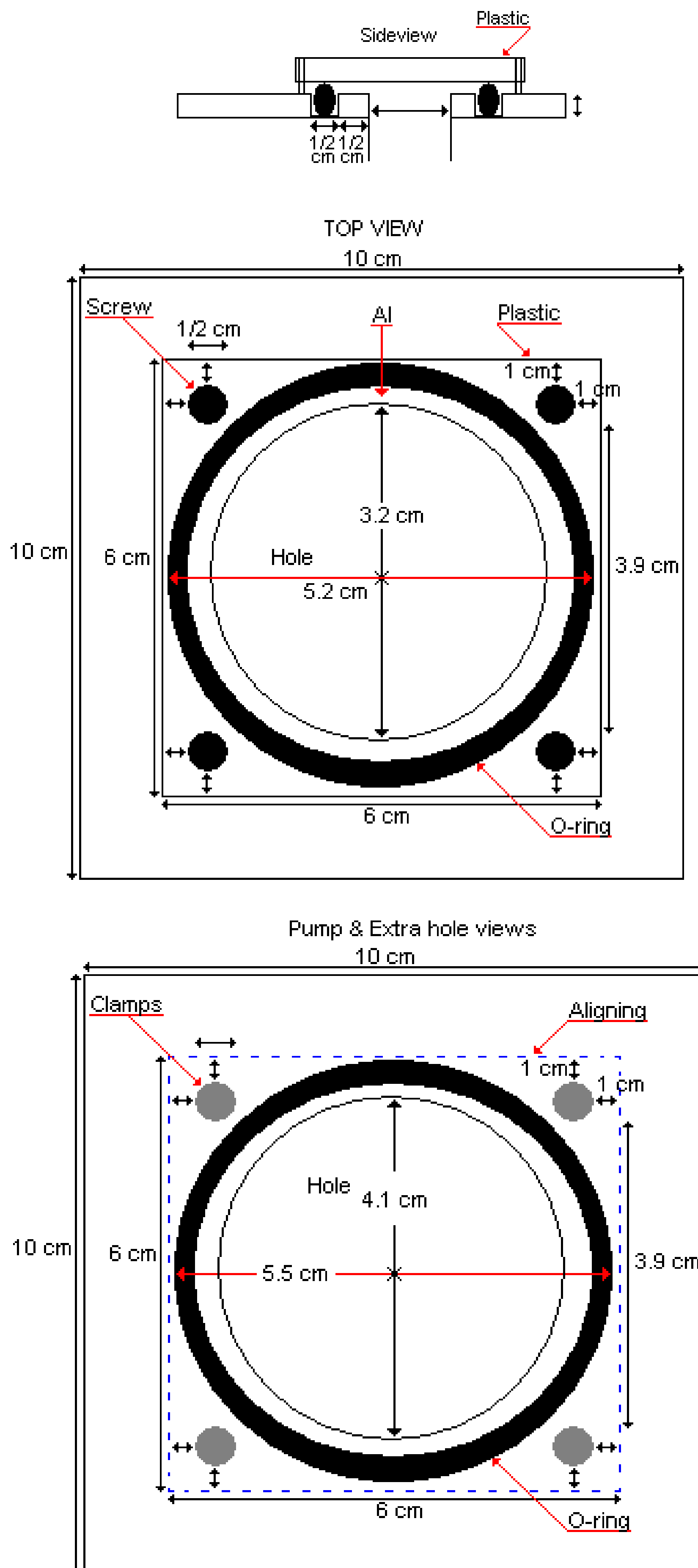

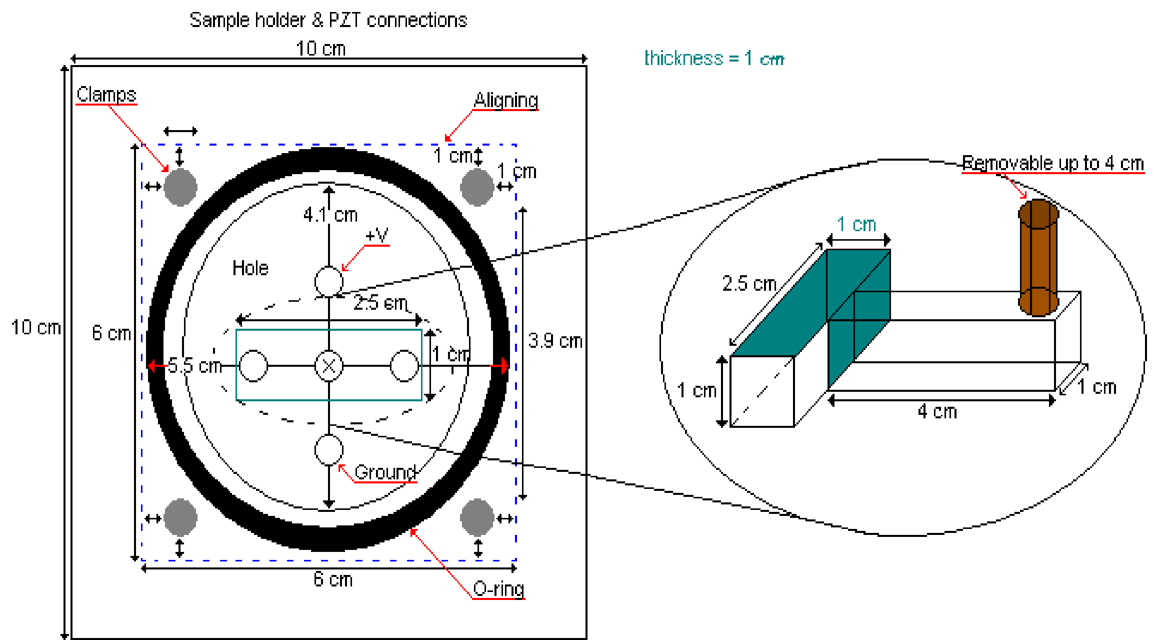
Sample holder & PZT connections
10 cm
thickness = 1 cm
Clamps
Aligning
1 cm
1 cm
4.1 cm
+V
Hole
2.5 cm
10 cm
6 cm
5.5 cm
1 cm
3.9 cm
Ground
6 cm
O-ring
Removable up to 4 cm
1 cm
2.5 cm
1 cm
4 cm
1 cm

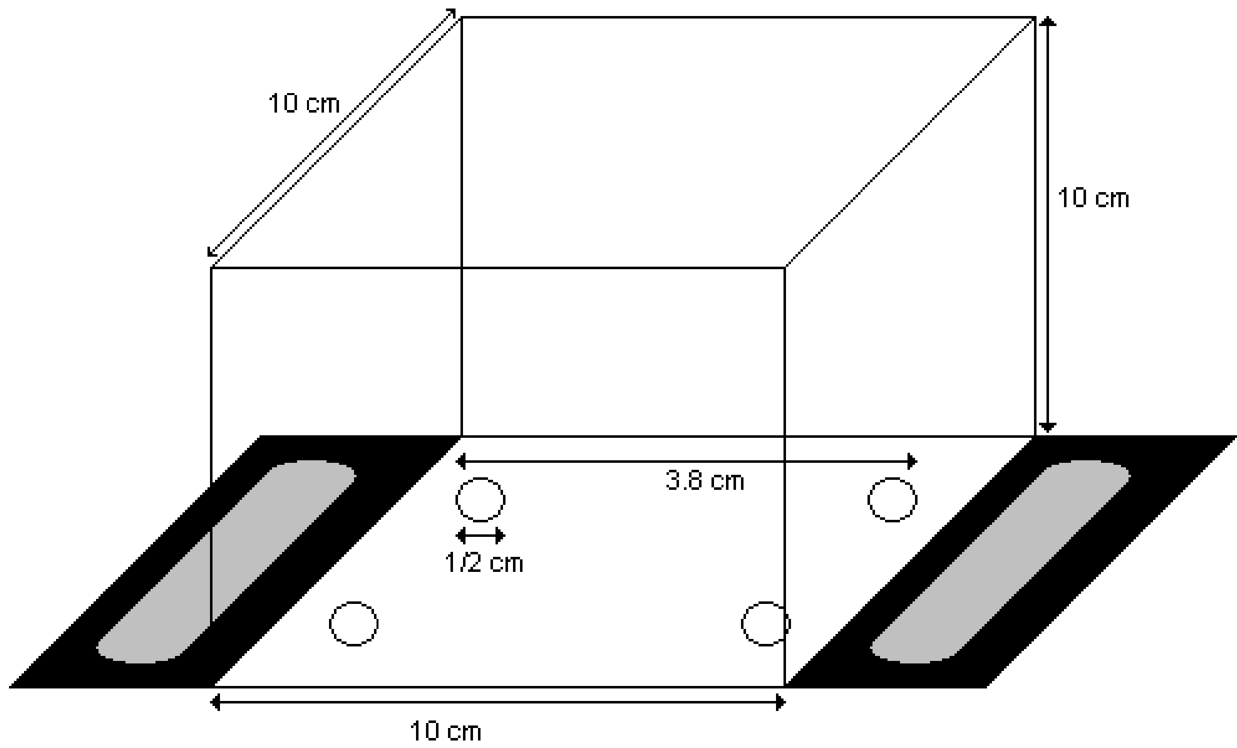
10 cm
10 cm
3.8 cm
1/2 cm
10 cm

Appendix E –Growth of Cells

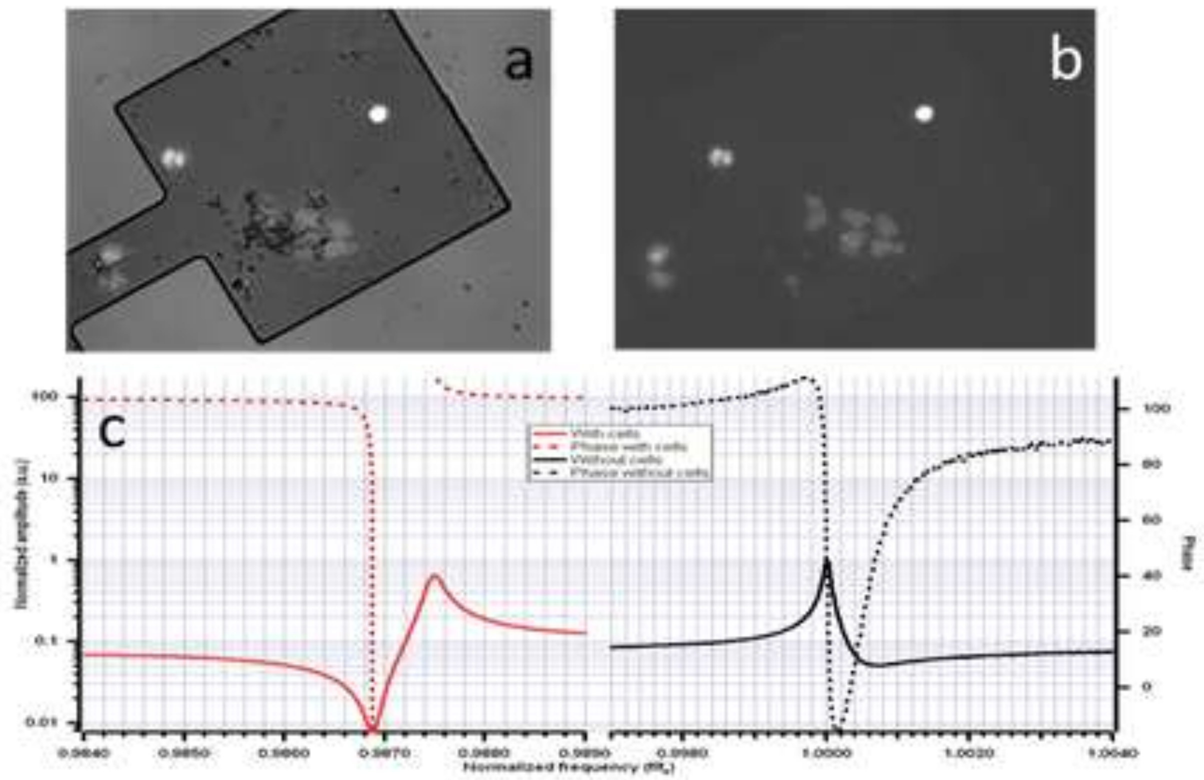

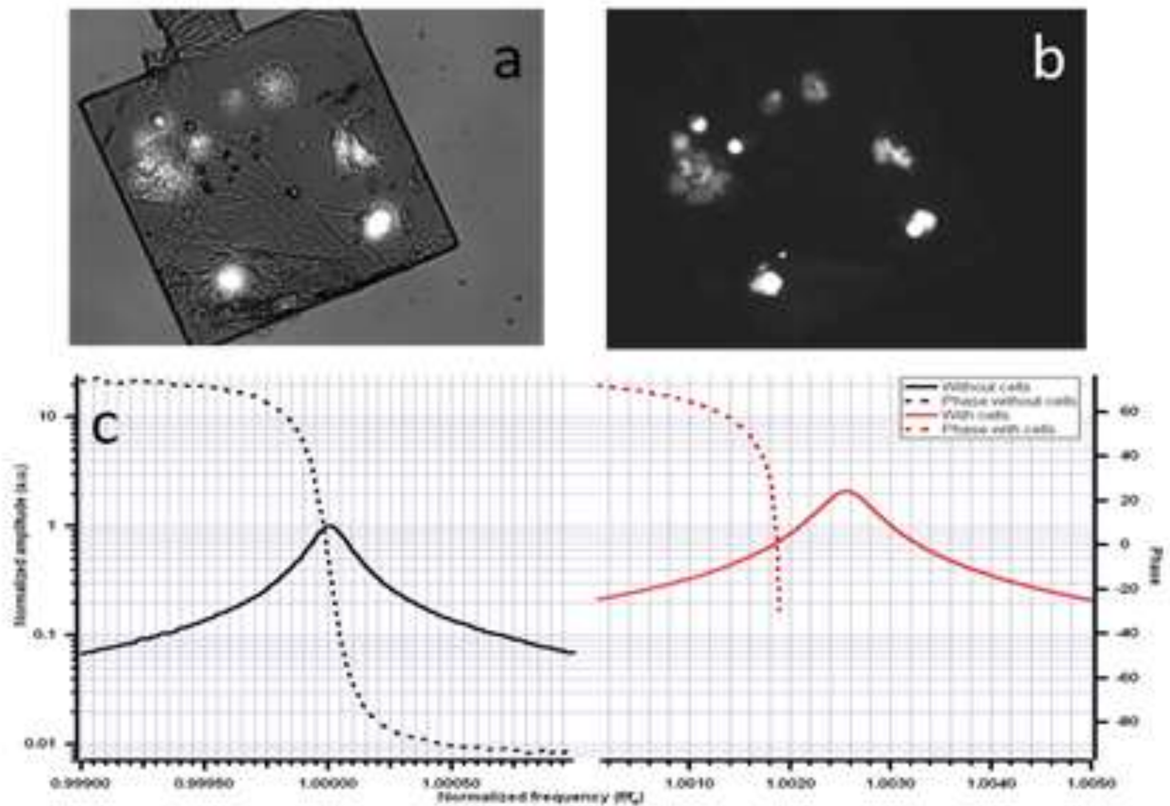

List of References

1. B. Lojek, *History of Semiconductor Engineering*, 1° ed. Springer, 2006.
2. www.itrs.net 03.02.2012
3. T. Mimura and S. Sakai. "Micro-Piezoelectric Head Technology of Color Inkjet Printer", DPP 2001: Eye on the Future, 230-234, 2001.
4. L. J. Hornbeck, "*Digital light processing for high-brightness, high-resolution applications*," Proceedings of the SPIE - The International Society for Optical Engineering , 3013: 27–40, 1997.
5. P.F. Van Kessel, L.J. Hornbeck, R.E. Meier, M.R. Douglass, "*A MEMS-based projection display*", Proceedings of the IEEE, 86(8): 1687-1704.
6. L. J. Hornbeck, "*Digital light processing update-status and future applications*", Proceedings of SPIE - The International Society for Optical Engineering, 3634: 158-170, 1999.
7. N. Barbour and G. Schmidt, "*Inertial sensor technology trends*" Proceedings of the IEEE ,1 (Sensors J.): 332–9, 2001.
8. C. Acar and A. M. Shkel, "*Experimental evaluation and comparative analysis of commercial variable-capacitance MEMS accelerometers*", J. Micromech. Microeng. (13): 634-645, 2003.
9. V. Kaajakari, Practical MEMS: *Design of microsystems, accelerometers, gyroscopes, RF MEMS, optical MEMS, and microfluidic systems*, Small Gear Publishing, 2009.
10. G. Binnig, C. F. Quate, C. Gerber, 'Atomic Force Microscope', Physical Review Letters, 56 (1986) 930.
11. P. Vettiger, M. Despont, U. Drechsler, U. Du¨ rig, W. Ha. berle, M. I. Lutwyche, H. E. Rothuizen, R. Stutz, R. Widmer, G. K. Binnig, "The "Millipede"— More than one thousand tips for future AFM data storage", IBM J. Res. Develop. 44(3): 323-340, 2000.
12. R. S. Decca, D. López, E. Fischbach, e D. E. Krause, "Measurement of the Casimir Force between Dissimilar Metals," Physical Review Letters, vol. 91, n°. 5, pag. 050402, Lug. 2003.
13. D. Rugar, R. Budakian, H. J. Mamin, e B. W. Chui, "Single spin detection by magnetic resonance force microscopy," Nature, vol. 430, n°. 6997, pagg. 329-332, Lug. 2004.
14. R. G. Knobel e A. N. Cleland, "Nanometre-scale displacement sensing using a single electron transistor," Nature, vol. 424, n°. 6946, pagg. 291-293, Lug. 2003.
15. K. Schwab, E. A. Henriksen, J. M. Worlock, e M. L. Roukes, "Measurement of the quantum of thermal conductance," Nature, vol. 404, n°. 6781, pagg. 974-977, Apr. 2000.
16. Y. T. Yang, C. Callegari, X. L. Feng, K. L. Ekinci, e M. L. Roukes, "Zeptogram-Scale Nanomechanical Mass Sensing," Nano Letters, vol. 6, n°. 4, pagg. 583-586, Apr. 2006.

17. M. D. LaHaye, J. Suh, P. M. Echternach, K. C. Schwab, e M. L. Roukes, “Nanomechanical measurements of a superconducting qubit,” Nature, vol. 459, n°. 7249, pagg. 960-964, Giu. 2009.
18. G. Binnig, H. Rohrer, Ch. Gerber, and E. Weibel. *Surface studies by scanning tunneling microscopy*. Physical Review Letters, 49:57,61, 1982.
19. http://sahussain.wordpress.com/2007/11/03/can-we-see-the-atomic-dimension, 03.02.2012.
20. Mo Li, H. X. Tang and M. L. Roukes, Ultra-sensitive NEMS-based cantilevers for sensing, scanned probe and very high-frequency applications, nature nanotechnology, Vol. 2, 2007
21. Philip S. Waggoner and Harold G. Craighead, Micro- and nanomechanical sensors for environmental, chemical, and biological detection, Lab Chip, 2007, 7, 1238–1255
22. Braun, T.; Ghatkesar, M. K.; Backmann, N.; Grange, W.; Boulanger, P.; Letellier, L.; Lang, H. P.; Bietsch, A.; Gerber, C.; Hegner, M. Nat. Nanotechnol. 2009, 4, 179–185.
23. Dorrestijn, M.; Bietsch, A.; Ac¸ikalin, T.; Raman, A.; Hegner, M.; Meyer, E.; Gerber, Ch. Phys. ReV. Lett. 2007, 98, 026102.
24. Varshney, M.; Waggoner, P. S.; Tan, C. P.; Aubin, K.; Montagna, R. A.; Craighead, H. G. Anal. Chem. 2008, 80 (6), 2141–2148.
25. G. Wu, H. Ji, K. Hansen, T. Thundat, R. Datar, R. Cote, M.F. Hagan, A.K. Chakraborty, A. Majumdar, *Origin of nanomechanical cantilever motion generated from biomolecular interactions*, Proc. Natl. Acad. Sci. U.S.A. 980 (2001) 1560–1564.
26. M. Alvarez, L.G. Carrascosa, M. Moreno, A. Calle, A. Zaballos, L.M. Lechuga, C. Martinez-A, J. Tamayo, *Nanomechanics of the formation of DNA self-assembled monolayers and hybridization on microcantilevers*, Langmuir, (2000).
27. D.J. Lockhart, E.A. Winzeler, *Genomics, gene expression and DNA arrays*, Nature 405 (2000) 827.
28. Ilic, B.; Czaplewski, D.; Neuzil, P.; Campagnolo, C.; Batt, C. Appl. Phys. Lett. 2000, 77, 450.
29. Ono, T.; Li, X.; Miyashita, H.; Esashi, M. ReV. Sci. Instrum. 2003,74, 1240.
30. Thundat, T.; Wachter, E. A.; Sharp, S. L.; Warmack, R. J. Appl. Phys. Lett. 1995, 66, 1695.
31. N. V. Lavrik, M. J. Stepaniak, and P. G. Datskos, Rev. Sci. Instrum. 75, 2229,(2004).
32. B. Ilic, Y. Yang, K. Aubin, R. Reichenbach, S. Krylov, and H. G. Craighead, Nano Lett. 5, 925 (2005).
33. K. L. Ekinci and M. L. Roukes, Rev. Sci. Instrum. 76, 061101 (2005).
34. T. Thundat, R. J. Warmack, G. Y. Chen, D. P. Allison, 'Thermal and ambient-induced deflections of scanning force microscope cantilevers', Applied Physics Letters, 64 (1994) 2894.
35. T. Thundat, G. Y. Chen, R. J. Warmack, D. P. Allison, E. A. Wachter, '*Vapor Detection Using Resonating Microcantilevers*', Analytical Chemistry, 67 (1995) 519.
36. Gupta A, Akin D and Bashir R 2003 Single virus particle mass detection using microresonators with nanoscale thickness Appl. Phys. Lett. 84 1976.
37. Gupta A and Akin D 2004 Detection of bacterial cells and antibodies using surface micromachined thin silicon cantilever resonators J. Vac. Sci. Technol. B 22 2785–91.

38. Vidic A, Then D and Ziegler C H 2003 A new cantilever system for gas and liquid sensing Ultramicroscopy 97 407–16.
39. Hagleitner C, Hierlemann A, Lange D, Kummer A, Kerness N, Brand O and Baltes H 2001 Smart single-chip gas sensor microsystem Nature 414 293–6.
40. G. Y. Chen, T. Thundat, E. A. Wachter, R. J. Warmack, "*Adsorption-induced surface stress and its effects on resonance frequency of microcantilevers*", Journal of Applied Physics, 77 (1995) 3618.
41. H. J. Butt, "*A sensitive method to measure changes in the surface stress of solids*", Journal of Colloid and Interface Science, 180 (1996) 251.
42. S. J. O'Shea, M. E. Welland, T. A. Brunt, A. R. Ramadan, T. Rayment, "*Atomic force microscopy stress sensors for studies in liquids"*, Journal of Vacuum Science & Technology B: Microelectronics and Nanometer Structures, 14 (1996) 1383.
43. J. K. Gimzewski, C. Gerber, E. Meyer, R. R. Schlittler, "*Observation of a chemical reaction using a micromechanical sensor*", Chemical Physics Letters, 217 (1994) 589.
44. J. R. Barnes, R. J. Stephenson, M. E. Welland, C. Gerber, J. K. Gimzewski, "*Photothermal Spectroscopy with Femtojoule Sensitivity Using a Micromechanical Device*", Nature, 372 (1994) 79.
45. H. P. Lang, R. Berger, F. Battiston, J. P. Ramseyer, E. Meyer, C. Andreoli, J. Brugger, P. Vettiger, M. Despont, T. Mezzacasa, L. Scandella, H. J. Güntherodt, C. Gerber, J. K. Gimzewski, " *chemical sensor based on a micromechanical cantilever array for the identification of gases and vapors*", Applied Physics A: Materials Science & Processing, 66 (1998) S61.
46. M. Tortonese, R. C. Barrett, C. F. Quate, "*Atomic resolution with an atomic force microscope using piezoresistive detection*", Applied Physics Letters, 62 (1993) 834.
47. J. Thaysen, A. Boisen, O. Hansen, S. Bouwstra, 'Atomic force microscopy probe with piezoresistive read-out and a highly symmetrical Wheatstone bridge arrangement', Sensors and Actuators A: Physical, 83 (2000) 47.
48. T. Itoh, T. Suga, 'Piezoelectric force sensor for scanning force microscopy', Sensors and Actuators A: Physical, 43 (1994) 305.
49. P. F. Indermuhle, G. Schurmann, G. A. Racine, N. F. de Rooij, 'Fabrication and characterization of cantilevers with integrated sharp tips and piezoelectric elements for actuation and detection for parallel AFM applications', Sensors and Actuators A: Physical, 60 (1997) 186.
50. C. L. Britton, R. L. Jones, P. I. Oden, Z. Hu, R. J. Warmack, S. F. Smith, W. L. Bryan, J. M. Rochelle, 'Multiple-input microcantilever sensors', Ultramicroscopy, 82 (2000) 17.
51. D. R. Baselt, B. Fruhberger, E. Klaassen, S. Cemalovic, C. L. Britton, S. V. Patel, T. E. Mlsna, D. McCorkle, B. Warmack, 'Design and performance of a microcantilever-based hydrogen sensor', Sensors and Actuators B: Chemical, 88 (2003) 120.
52. N. Blanc, J. Brugger, N. F. de Rooij, U. Durig, 'Scanning force microscopy in the dynamic mode using microfabricated capacitive sensors', journal of Vacuum Science & Technology B: Microelectronics and Nanometer Structures, 14 (1996) 901.
53. G. Shekhawat, S.-H. Tark, V. P. Dravid, 'MOSFET-Embedded Microcantilevers for Measuring Deflection in Biomolecular Sensors', Science, 311 (2006) 1592.

54. J. Fritz, M.K. Baller, H.P. Lang, H. Rothuizen, P. Vettiger, E. Meyer, H.-J. Guntherodt, Ch. Gerber, and J.K. Gimzewski. Science, 288(5464):316, 2000.
55. G.-H. Wu, R.H. Data, K.M. Hansen, T. Thundat, R.J. Cote, and A. Ma-jumdar. Bioassay of prostate-speci¯c antigen (psa) using microcantilevers. Nature Biotechnolgy, 19:856860, 2001.
56. J. H. Lee, T. S. Kimb, and Ki. H. Yoon. E®ect of mass and stress on resonant frequency shift of functionalized pb(zr0:52ti0:48)o3 thin ¯lm microcantilever for the detection of c-reactive protein. Applied Physics Letters, 48(16):3187{3189, 2004.
57. A. Hierlemann, D. Lange, C. Hagleitner, N. Kerness, A. Koll, O. Brand, and H. Baltes. Application-speci¯c sensor systems based on cmos chemical microsensors. Sensors and Actuators B, 70(1-3):2{11, 2000.
58. E. Forsen, G. Abadal, S. Ghatnekar-Nilsson, J. Teva, J. Verd, R. Sandberg, W. Svendsen, F. Perez-Murano, J. Esteve, E. Figueras, F. Campabadal, L. Montelius, N. Barniol, and A. Boisen. Ultrasensitive mass sensor fully integrated with complementary metal-oxide-semiconductor circuitry. Applied Physics Letters, 87(4):043507, 2005.
59. E. Fors´en. Nano-cantilevers fully integrated with cmos for ultrasensitive mass detection. PhD thesis, DTU Nanotech, Technical University of Denmark (DTU), 2005.
60. M. U. Demirci, M. A. Abdelmoneum, and C. T.-C. Nguyen, Digest of Technical Papers, The 12th International Conference on Solid-State Sensors and Actuators (Transducers'03), Boston, MA, 8–12 June 2003 (un- published), pp. 955–958.
61. Ilic, B. et al. Attogram detection using nanoelectromechanical oscillators. J. Appl. Phys. 95, 3694–3703 (2004)
62. K. L. Ekcini, X. M. H. Huang, and M. L. Roukes, Appl. Phys. Lett. 84, 4469 (2004).
63. D. K.Wickenden, J. L. Champion, R. Osiander, R. B. Givens, J. L. Lamb, J. A. Miragliotta, D. A. Oursler, and T. J. Kistenmacher, Acta Astronaut. 52, 421 (2003).
64. Q. Chen, L. Huang, and Y.-C. Lai, "Chaos-induced intrinsic localized modes in coupled microcantilever arrays," Applied Physics Letters, vol. 92, no. 24, p. 241914, 2008.
65. M. Sato, B. E. Hubbard, L. Q. English, A. J. Sievers, B. Ilic, D. A. Czaplewski, and H. G. Craighead, Chaos 13, 702, 2003.
66. B. Ilic and H. G. Craighead, Enumeration of DNA Molecules Bound a Nanomechanical Oscillator, Nano Letters, Vol. 5 No. 5 (2005) 925-929
67. A. Qazi et al., Asymmetrical twin cantilevers for single molecule detection, Appl. Phys. Lett., 90 173118 (2007).
68. M. Spletzer et al., Ultrasensitive mass sensing using mode localization in coupled Microcantilevers, Appl. Phys. Lett., 88, 254102 (2006).
69. Eduardo Gil-Santos, Daniel Ramos, Anirban Jana, Montserrat Calleja, Arvind Raman, and Javier Tamayo, Mass Sensing Based on Deterministic and Stochastic Responses of Elastically Coupled Nanocantilevers,NANO LETTERS 2009 Vol. 9, No. 12 4122-4127.
70. Hajime Okamoto,Takehito Kamada,Koji Onomitsu,Imran Mahboob and Hiroshi Yamaguchi,Optical Tuning of Coupled Micromechanical Resonators, Applied Physics Express 2 (2009) 062202.

71. S. Ghatnekar-Nilsson, J. Graham, R. Hull, and L. Montelius, “Multi-frequency response from a designed array of micromechanical cantilevers fabricated using a focused ion beam,” Nanotechnology, vol. 17, no. 20, pp. 5233-5237, Oct. 2006.
72. Mariateresa Napoli, Wenhua Zhang, Student Member, IEEE, Student Member, ASME, Kimberly Turner, Member, IEEE, Member, ASME, and Bassam Bamieh, Senior Member, IEEE, Characterization of Electrostatically Coupled Microcantilevers, JOURNAL OF MICROELECTROMECHANICAL SYSTEMS, VOL. 14, NO. 2, APRIL 2005.
73. M. Spletzer, A. Raman, H. Sumali, and J. P. Sullivan, “Highly sensitive mass detection and identification using vibration localization in coupled microcantilever arrays,” Applied Physics Letters, vol. 92, no. 11, p. 114102, 2008.
74. P. Rai-Choudhury (Ed.), Handbook of Microlithography, Micromachining and Microfabrication, Vol. 2, Micromachining and Microfabrication, SPIE Optical Engineering Press, Bellingham, WA, USA (1997).
75. Goeran Stemme. Resonant silicon sensors. Journal of Micromechanics and Microengineering, 1(2):113{125, 1991.
76. Scott A. Miller, Kimberly L. Turner ,Noel C. MacDonald, Microelectromechanical scanning probe instruments for array architectures, American Institute of Physics, 1997, 4155-4162.
77. http://www.gitam.edu/eresource/Engg_Phys/semester_2/dielec/BaTiO3.htm, 25.02.2012.
78. P.A. Rasmussen, J. Thaysen, S. Bouwstra and A.Boisen, Modular design of AFM probe with sputtered silicon tip, Sensors and Actuators A 92 (2001) 96-101.
79. R. Mukhopadhyay, V. V. Sumbayev, M. Lorentzen, J. Kjems, P. a Andreasen, and F. Besenbacher, “Cantilever sensor for nanomechanical detection of specific protein conformations.,” Nano letters, vol. 5, no. 12, pp. 2385-8, Dec. 2005.
80. D. Ramos, J. Mertens, M. Calleja, and J. Tamayo, Phototermal self-excitation of nanomechanical resonators in liquids APPLIED PHYSICS LETTERS 92, 173108,2008.
81. Nickolay V. Lavrik and Panos G. Datskos, Femtogram mass detection using photothermally actuated nanomechanical resonators APL. Vol. 82, No. 16, 2003.
82. Quirin P. Unterreithmeier, Eva M. Weig and Jo¨rg P. Kotthaus, Universal transduction scheme for nanomechanical systems based on dielectric forces Nature, Vol. 458, 2009.
83. Teva J, Abadal G, Torres F, Verd J, Pérez-Murano F, Barniol N (2005) A femtogram resolution mass sensor platform, based on SOI electrostatically driven resonant cantilever. Part I: electromechanical model and parameter extraction. Ultramicroscopy 106:800–807.
84. J. L. Ekinci, X.M.H. Huang, M.L. Roukes, Appl. Phys. Lett. 84 (2004) 4469-4471
85. Waggoner, P. S., Varshney, M. & Craighead, H. G. Detection of prostate specific antigen with nanomechanical resonators. Lab on a Chip 9, 3095–3099 (2009).
86. Burg, T. P. et al. Weighing of biomolecules, single cells and single nanoparticles in fluid. Nature 446, 1066–1069 (2007).
87. Jensen, K., Kim, K. & Zettl, A. An atomic-resolution nanomechanical mass sensor. Nature Nanotech. 3, 533–537 (2008).

88. Belov, M. et al. Mechanical resonance of clamped silicon nanowires measured by optical interferometry. J. Appl. Phys. 103, 074304 (2008).
89. Fadel L, Lochon F, Dufour I and Francais O, Chemical sensing: millimeter size resonant microcantilever performance , J. Micromech. Microeng. 14, S23–S30, 2004.
90. Simon Dandavino, Development of Resonator Based Atomic Oxygen Sensor System for Spacecraft Applications, M.Sc. Thesis, Department of Micro and Nanotechnology Techenical University of Denmark, 2007, chapter 4.
91. Karen M. Goeders, Jonathan S. Colton, and Lawrence A. Bottomley, Microcantilevers: Sensing Chemical Interactions via Mechanical Motion, Chem. Rev. 2008, 108, 522-542.
92. W.T. Thomson, Theory of Vibration with Applications, Prentice Hall, Inc., Englewood, Cliffs, NJ, 1981.
93. F.S. Tse, I.E. Morse, R.T. Hinkle, Mechanical Vibrations, Theory and Applications, Allyn and Bacon, Inc., Boston, 1978.
94. R.A. Buser and N.F. De Rooij, Resonant silicon structures, Sensors and Actuators, 17 145-154 (1989).
95. Evgeni Gusev, Eric Garfunkel and Arthur Dideikin, Advanced Materials and Technologies for Micro/Nano-Devices, Sensors and Actuators, Springer, 2009.
96. Michael J. Heller and Anderas Guttman, Integrated Microfabricated Biodevices, 2002.
97. Guckel, H.,High aspect ratio micromachining via deep X-ray lithography, Proc. IEEE, 86 (1998), 1586
98. Gary Wiederrecht, Handbook of Nanofabrication, Elsevier, 2010.
99. Kovacs, G.T.A., Micromachined Transducers Sourcebook, McGraw-Hill, New York, NY, 1998.
100. Sami Franssila, Introduction to Microfabrication, Wiley, 2004.
101. Madou, M., Fundamentals of Microfabrication, CRC Press, Inc., Boca Raton, FL, 1997
102. Petersen, K.E., Silicon as a Mechanical Material, Proceedings of the IEEE, May 1982, Vol. 70, No. 5, pp.420-457
103. F. Filhol, E. Defa, C. Divoux, C. Zinck, and M. Delaye, “Resonant micro-mirror excited by a thin-film piezoelectric actuator for fast optical beam scanning,” Sensors and Actuators A: Physical, vol. 123-124, pp. 483-489, Sep. 2005.
104. P. Castellini, “Measurement of vibrational modal parameters using laser pulse excitation techniques,” Measurement, vol. 35, no. 2, pp. 163-179, Mar. 2004.
105. S. C. Masmanidis, R. B. Karabalin, I. De Vlaminck, G. Borghs, M. R. Freeman, and M. L. Roukes, “Multifunctional nanomechanical systems via tunably coupled piezoelectric actuation.,” Science (New York, N.Y.), vol. 317, no. 5839, pp. 780-3, Aug. 2007.
106. B. Ilic, S. Krylov, K. Aubin, R. Reichenbach, H.G. Craighead, Optical excitation of nanoelectromechanical oscillators, Appl. Phys. Lett. 86 (2005) 193114
107. S. Alexander, et al., An atomic-resolution atomic-force microscope implemented using an optical lever, J. Appl. Phys. 65 (1989) 164
108. D. Ramos et al., “Arrays of dual nanomechanical resonators for selective biological detection,” Analytical chemistry, vol. 81, no. 6, pp. 2274-9, Mar. 2009.

109. L. Sekaric, M. Zalalutdinov, S. W. Turner, A. T. Zehnder, J. M. Parpia, and H. G. Craighead, APPLIED PHYSICS LETTERS, VOLUME 80, NUMBER 19, 2002.
110. B. Ilic, D. Czaplewski, M. Zalalutdinov, H.G. Craighead, P. Neuzil, C. Campagnolo, C. Batt, J. Vac. Sci. Technol. B 19 (2001) 2825.
111. J. Tamayo, D. Ramos, J. Mertens, M. Calleja, Effect of the adsorbate stiffness on the resonance response of microcantilever sensors, Appl. Phys. Lett. 89 (2006) 224104.
112. Y.S. Joe, A.M. Satanin, C.S. Kim, Classical analogy of Fano resonances, Phys. Scr. 74 (2006) 259.
113. N. Yao, ed., Focused Ion Beam Systems - Basics and Applications. Cambridgeuniversity Press, 2007.
114. A. Tseng, Recent developments in micromilling using focused ion beam technology,JOURNAL OF MICROMECHANICS AND MICROENGINEERING, vol. 14, pp. R15_R34, Apr. 2004.
115. http://en.wikipedia.org/wiki/Focused_ion_beam, 28.02.2012
116. Héctor J. De Los Santos, RF MEMS Circuit Design for Wireless communications, Artech House, 2002.
117. G.M. Rebeiz and J.B. Muldavin, RF MEMS Switches and Switch Circuits, IEEE Microwave Magazin, 2001.
118. L.P.B. Katehi, J.F. Harvey, and E. Brown, MEMS and Si Micromachined Circuits for High-Frequency Applications, IEEE Transactions On Mircowave Theory and Techniques, Vol. 50, no. 3, 2002.
119. B. Schauwecker, K. M. Strohm, W. Simon, J. Mehner, and J.-F. Luy, Toggle Switch – A new type of high bandwidth RF MEMS Switch, IEEE MTT-S, 2002.
120. I. Mahboob, E. Flurin, K. Nishiguchi, A. Fujiwara & H. Yamaguchi, Interconnect-free parallel logic circuits in a single mechanical resonator, Nature communications, 2:198,2011.
121. C.T. Nguyen et al., Vibrating RF MEMS for low power wireless communications, Proc. Int. MEMS Workshop (MEMS'01), July 2001.
122. C.T. Nguyen, et al., Frequency-Selective MEMS for miniaturized low-power communication devices, IEEE Trans. Mircowave theory and techniques, Vol. 47, n. 8, 1999.
123. Jae Y. Park, Jong U. Bu, and Joong W. Lee, RF MEMS Devices for Wireless Applications, JOURNAL OF SEMICONDUCTOR TECHNOLOGY AND SCIENCE, VOL.1, NO. 1, 2001.
124. ECE60L Lecture Notes, Spring 2002.
125. Results made by Mauro Melli.
126. A. H. Nayfeh and D. T. Mook, Nonlinear Oscillations,Wiley, New York, 1979.
127. Alessandro Didonna, Giuseppe Legname, Aberrant ERK 1/2 complex activation and localization in scrapie-infected GT1-1 cells, Molecular Neurodegeneration, 2010, 5:29